NTNU

Norwegian University of
Science and Technology

Harmonic Resonance Mode Analysis and Application for Offshore Wind Power Plants

Henrik Andreas Brantsæter

Master of Energy and Environmental Engineering
Submission date: December 2015
Supervisor: Elisabetta Tedeschi, ELKRAFT

Norwegian University of Science and Technology
Department of Electric Power Engineering

Preface

This thesis is the result of my 11^{th} and final semester as a master student at the Department of Electric Power Engineering, NTNU.

Łukasz Kocewiak at DONG Energy Wind Power has co-supervised my work for this thesis. He initiated the cooperation which led to a specialisation project and master thesis related to harmonics in offshore wind power plants. I would like to thank him for sharing his exceptional knowledge and experience in conference calls, emails, and on the occasions we have met in Trondheim.

Secondly, I would like to thank Atle Rygg Årdal for guiding me in choosing a topic for my specialisation project, and for providing invaluable contributions and support to a paper which was submitted in relation to the specialisation project.

The main supervisor for this master thesis has been Prof. Elisabetta Tedeschi. I would like to express my sincere gratitude to her for taking an interest in my work, finding time to give valuable feedback, and for being enthusiastic and supportive.

Lastly, I would like to thank my family for inspiration, love and support.

NTNU Trondheim, December 2015
Henrik Andreas Broch Brantsæter

Abstract

This thesis is centred around a form of resonance analysis for power systems known as Harmonic Resonance Mode Analysis (HRMA). It is a form of eigenvalue analysis and has some parallels to the modal analysis commonly associated with small signal stability. Modes in small signal stability analysis characterise the transient response of the system to a small disturbance, and are identified from the state matrix of the linearised state space description. Modes in HRMA characterise the parallel resonances of a power system, and are identified from the admittance matrix. Participation factors, which are derived from eigenvectors of the admittance matrix at resonance frequencies, indicate the observability of modes in the impedance measured at individual buses. In addition, sensitivity indices quantify the change in amplitude and frequency of modes when parameters are adjusted in the admittance matrix.

A part of this thesis is dedicated to replicating HRMA results found in published papers. By validating published results for two different test cases, the computer implementation for carrying out the analysis is verified. Obtained results are generally consistent with those in published papers. Some critical considerations in implementation of HRMA are identified and discussed, perhaps the most important of which is the issue of modal switching.

HRMA is also used to investigate resonances in a system modelled on the real offshore wind power plant of Anholt in Denmark. HRMA is based on the nodal admittance matrix, and power system components are modelled as equivalent admittances. Non-linearities and frequency dependencies can be included more easily than in a state space representation. Examining the impact of non-linear components in the admittance matrix on HRMA results is a central contribution from this thesis. The sensitivity of results with respect to degree of aggregation of the wind power plant model is also investigated.

Modern wind turbines are connected to power systems via full-scale frequency converters. Such converters can be modelled for harmonic analyses as equivalent impedances which are determined primarily from the converter current control loops. An equivalent impedance representing the grid-side converter of a wind turbine generator as seen from the grid is derived, and later such impedances are incorporated in the HRMA.

The resonance modes in the investigated large offshore wind power plant are sensitive to modelling of wind turbine main circuit components such as shunt harmonic filters, step-up transformers and main reactors. Suitable modelling of these electrical components is therefore important for obtaining reliable result from HRMA. Moreover, the resonance modes are highly dependent on the number of turbines in operation.

Sammendrag

Denne oppgaven omhandler en metode for analyse av resonanser i kraftsystemer kjent som HRMA (eng. Harmonic Resonance Mode Analysis). Innen kraftsystemanalyse er det velkjent at egenverdiene til den lineariserte tilstandsrombeskrivelsen, også kjent som systemets modi, bestemmer systemets transiente respons til små forstyrrelser. HRMA har visse paralleller til denne formen for analyse. Det har vist seg at egenverdiene til admittansmatrisen blir svært små ved frekvenser som er knyttet til parallelle resonanser. Mininum i egenverdienes frekvensresponser kan derfor defineres som systemets resonans-modi (eng. resonance modes). Impedansen målt fra de ulike nodene i kretsen kan knyttes til de ulike resonans-modi gjennom admittansmatrisens egenvektorer. I tillegg er det definert indekser som indikerer hvordan frekvensen og amplituden til resonans-modiene endres ved ved å justere parametere i admittansmatrisen.

Ett kapittel i denne oppgaven er avsatt til å gjenskape HRMA-resultater for to ulike testsystemer som av andre har blitt presentert i publiserte artikler. På den måten verifiseres implementering av metoden i MATLAB. Resultater som presenteres fra de to testsystemene i denne oppgaven er i overensstemmelse med de resultatene som finnes i tidligere publiserte artikler. Noen viktige betraktninger rundt implementeringen av HRMA som ikke finnes i de nevnte artikler blir identifisert og diskutert.

HRMA benyttes videre til å analysere parallelle resonanser i ett system modellert etter den reelle hav-vindparken ved øyen Anholt i Danmark. HRMA baserer seg på admittans-matrisen til systemet som analyseres, og hver komponent modelleres som en ekvivalent admittans. Det er enklere å inkludere ulineære komponenter i en slik admittansmodell enn i en tilstandsrombeskrivelse. Undersøkelser av hvordan HRMA-resultatene påvirkes når ulineære komponenter inkluderes i admittansbeskrivelsen er ett sentralt bidrag fra denne oppgaven. Det undersøkes også hvordan resultatene påvirkes av ulike grader av aggregering av vindparkmodellen.

Moderne vindturbiner knyttes til nettet via fullskala frekvensomformere. For harmonisk analyse fremstår slike omformere som frekvensavhengige impedanser som særlig påvirkes av omformerens strømregulator. Fra ett teoretisk perspektiv vises det i denne oppgaven

hvordan en slik ekvivalent impedans kan utledes, og videre inkluderes disse impedansene i HRMA av vindparkmodellen.

Analyse av vindparken viser at resonans-modiene er sensitive med hensyn til modellering av komponentene som finnes i nær tilknytning til hver enkelt turbin, slik som harmoniske filtre og transformatorer. Det er derfor viktig å modellere slike komponenter med omhu for harmonisk analyse. Videre er vindparkens modi svært avhengig av antall turbiner som til en hver tid produserer.

Contents

List of Figures

List of Tables

Abbreviations

AC	**A**lternating **C**urrent
CIGRE	**C**onseil **I**nternational des **G**rands **R**éseaux **É**lectriques (The International Council on Large Electric Systems)
DC	**D**irect **C**urrent
DSO	**D**istribution **S**ystem **O**perator
IEEE	**I**nstitute of **E**lectrical and **E**lectronics **E**ngineers
HRMA	**H**armonic **R**esonance **M**ode **A**nalysis
HVAC	**H**igh **V**oltage **A**lternating **C**urrent
HVDC	**H**igh **V**oltage **D**irect **C**urrent
MATLAB	**M**atrix **L**aboratory (computing environment)
PCC	**P**oint of **C**ommon **C**oupling
PF	**P**articipation **F**actor
PWM	**P**ulse **W**idth **M**odulation
SVC	**S**tatic **V**AR (reactive power) **C**ompensator
TSO	**T**ransmission **S**ystem **O**perator
VSC	**V**oltage **S**ource **C**onverter
WPF	**W**eighted **P**articipation **F**actor
WPP	**W**ind **P**ower **P**lant
WTG	**W**ind **T**urbine **G**enerator

Symbols

f	frequency	pu or Hz
f_1	fundamental frequency	pu or Hz
h	harmonic number	pu
ω	angular frequency	$\mathrm{rad\,s^{-1}}$
R	Resistance	pu or Ω
L	Inductance	pu or H
C	Capacitance	pu or F
X	Reactance	pu or Ω
G	Conductance	pu or S
B	Susceptance	pu or S
$[Y], [Y_f]$	Nodal admittance matrix (at frequency f)	
$[Z], [Y]^{-1}$	Nodal impedance matrix	
$[V], [V_f]$	Nodal voltage vector (at frequency f)	
$[I], [I_f]$	Nodal current vector (at frequency f)	
$[U]$	Modal voltage vector	
$[J]$	Modal current vector	
V_i	Nodal voltage at bus i	pu or V
I_i	Nodal current at bus i	pu or A
Z_{ii}	Driving point impedance bus i	pu or Ω
Y_{ii}	Driving point admittance bus i	pu or S
$Z_{m,k}$	Modal impedance number k	pu or Ω
λ_k	Eigenvalue number k	
l_k	Left eigenvector of k-th eigenvalue	
t_k	Right eigenvector of k-th eigenvalue	
$[\Lambda]$	Diagonal eigenvalue matrix	

$[L]$	left eigenvector matrix
$[T]$	right eigenvector matrix
α	Parameter of some power system component
Al	Aluminium
Cu	Copper

1 Introduction

In the context of worldwide commitments on curbing greenhouse gas emissions and transitioning to low carbon economies, governing bodies such as the EU, and intergovernmental agencies such as IEA (International Energy Agency), envision electricity generation in future power systems will be predominantly from renewable sources [1]. Offshore wind represents one of the most stable sources of renewable energy in many parts of the world. In comparison to onshore wind, there are benefits like reduced "Not In My Back Yard"-opposition, stronger and more consistent winds, and fewer constraints with respect to structure size and noise. Though harnessing the offshore wind energy is technically challenging and more expensive compared to onshore wind in today's market, offshore wind technology is rapidly emerging and arguably has important long-term potential. Realising the full potential of offshore wind will require support from policy makers in facilitating continued cost reduction through research and development of turbine and transmission technology, supply chain optimisation, and operation & maintenance [2].

1.1 Problem Background and Motivation

Power system voltage and current waveforms are ideally sinusoidal, continuous and of constant frequency. Power quality can be defined as the combination of *voltage quality* and *current quality*, and is concerned with the deviation of voltage and current waveforms from the ideal. Harmonics are one of the major types of disturbances to the ideal waveforms covered by the broader term of *power quality disturbances* [3].

State of the art offshore Wind Power Plants (WPP) are large and complex structures including Wind Turbine Generators (WTG), array cable systems and HVAC or HVDC export systems. Such WPPs represent new challenges with respect to prediction and mitigation of harmonic emission and propagation [4]. Harmonic resonances in power systems have the potential to amplify harmonic distortion. In offshore WPPs this issue is exacerbated by the heavily armoured submarine cables required for collection

and transmission of power. The capacitance of such cables can introduce problematic resonances at relatively low frequencies.

Although the cause of harmonic resonance is well understood, the tools and techniques available for analysis of such phenomena are arguably quite limited. Harmonic Resonance Mode Analysis (HRMA) is a relatively new application of eigenvalue analysis, and is also known as Resonance Mode Analysis (RMA) or simply modal analysis. It has been suggested that this method can be used in conjunction with traditional harmonic analysis to gain better understanding of harmonic resonances and solve harmonic problems more effectively [5–8]. However, the benefits and limitations of this method are not entirely clear from the handful of published papers which are related to it.

1.2 Limitations of Scope

The objective of this thesis is to investigate the potential of HRMA as a tool for harmonic resonance analysis. It aims to provide a comprehensive review of the HRMA concept, including verification of previous works on the topic. Application of the HRMA method to a large offshore wind power plant facilitates independent contributions. Examination of the sensitivity of HRMA results with respect to non-linearities and degree of model simplification constitutes the main independent contribution of the thesis.

The HRMA method is usually associated to the nodal admittance matrix, also known as Y-bus matrix, of the system under study, and only this kind of system description is considered in the thesis. As a consequence, HRMA is limited to the study of parallel resonances. An alternative system description, known as the loop impedance matrix, in principle allows for equivalent investigation of series resonances. HRMA based on loop impedance description has however received little attention in published papers, and is considered outside the scope of this thesis.

Quantifying actual waveform distortion due to harmonic emission and propagation is considered outside the scope of the thesis.

1.3 Relation to Specialisation Project

The author wrote a specialisation project in the autumn of 2014, titled "Wind Turbine and Offshore Wind Power Plant Modelling for System Level Harmonic Studies" [9]. Some findings from the specialisation project were presented in a paper [10]. The project's objective was to create a foundation for system level time-domain harmonic studies of offshore WPPs. It consisted of the following main components:

- A literature study covering topics such as offshore WPP layout, power electronics for variable-speed wind turbines, harmonic waveforms, harmonic resonance, harmonic indices, passive filters, standards and grid codes related to harmonic distortion.
- Design of emission filter (LCL filter) for the grid connection of wind turbines with full-scale converters.
- Current control in a synchronously rotating *dq*-reference frame for representation of wind turbine grid-side converter harmonic interaction.

Simulation of harmonics in an offshore WPP and subsequent Fourier analysis of the time-dependent results turned out to be a challenging task. Certain studies suggest accurate results from time-domain simulation of harmonics requires massive parallel processing and efficient modelling of converters [11]. It was decided to work within the frequency domain for this thesis.

Some content from the project's literature study, although mostly rewritten and restructured, is included to ensure the thesis can be regarded a complete and independent work. As will be shown, the specialisation project's findings related to emission filter design and converter control also have relevance to the resonance analysis carried out in this thesis.

1.4 Structure

The thesis is organised as follows: Chapter 2 presents fundamental theory on harmonics, harmonic resonance and available techniques for harmonic resonance analysis, including HRMA. Chapter 3 covers the modelling of power system components for harmonic resonance analysis. Chapter 4 is dedicated to verifying HRMA results which can be found in published papers, hence also validating the implementation of HRMA which has been done from scratch in MATLAB. Important considerations and limitations identified in this process are discussed. In Chapter 5, HRMA is applied to a model of a large offshore WPP, based on the Anholt WPP in Denmark. Discussion and Conclusions follow in Chapter 6 and Chapter 7 respectively.

2 Harmonic Analysis Theory

This chapter presents fundamental concepts and definitions related to harmonics and harmonic analysis. Available methods for harmonic resonance analysis are presented and compared. Theory behind HRMA is presented in detail.

2.1 Harmonics

Any periodic waveform of period T can be expressed as a Fourier Series. This means a function $g(t) = g(t + T)$ with fundamental frequency f_1 can be expressed as

$$g(t) = C_0 + \sum_{h=1}^{\infty} C_h \cos(hf_1 + \phi_h) \tag{2.1}$$

where coefficient C_0 is the DC component, C_h is the magnitude and ϕ_h is the phase angle of the h-th order integer harmonic component [12].

Waveform distortion can in general be quantified by considering the waveform as a sum of frequency components which are superimposed on the ideal fundamental frequency waveform. In power systems, the dominant distortion components usually appear at frequencies which are integer multiples of the fundamental frequency. Hence, the term harmonic distortion is commonly used as a synonym for waveform distortion, even if the frequency of some components are not integer multiples of the fundamental. The non-integer multiple frequency components are often referred to as inter-harmonics, while non-integer harmonics below the fundamental frequency can be categorized as sub-harmonics [13].

Interest in power quality has surged in recent decades. Increased sensitivity of equipment to voltage quality, and proliferation of power electronic devices in generation, transmission and consumption, are often credited as the main drivers for this. In addition, companies have become less tolerant to equipment malfunction and production process stoppages. Restructuring and deregulation of power markets has also led to an increased need for power quality indicators [3].

Distorted voltage and current waveforms may result in reduced lifetime or failure of sensitive power system components. Voltage distortion affects primarily shunt connected components, ranging from capacitor banks and industrial drives to fluorescent lamps and computer equipment. Current distortion affect primarily the series connected elements, such as transformers [3]. Harmonics can also interfere with control, communication and protective equipment [14].

In relation to offshore WPPs, harmonic distortion is of concern both to the network system operators (i.e. TSO or DSO depending on voltage level at PCC) and to the WPP operators. A system operator is concerned with adhering to regulations on power quality, and therefore may specify connection requirements for WPPs in the form of grid codes. A WPP operator is concerned with grid code compliance, as well as potential damage to equipment and WPP malfunction due to harmonic distortion [9, 13].

There are two main categories of harmonic sources in power systems. The first type of devices are those with non-linear voltage-current relationships, such as iron core reactors and transformers. The second category consists of power electronic devices. In a balanced three-phase system, where voltages and current are of equal magnitude with 120 degrees phase shift between phases, only so-called characteristic harmonics are produced by power electronic converters. The characteristic harmonics are defined from converter topology. Because the switching of such devices in steady state is usually synchronised to the fundamental frequency, the characteristic harmonics are also integer harmonics. In reality there is always some degree of asymmetry between phases, causing non-characteristic harmonics to be present as well. These are not related to the converter topology, but are determined by the operating point and control scenario of power electronic converters [12, 14].

Under balanced operating conditions, integer harmonics can be associated to either positive, negative, or zero sequence. Assuming power is supplied in positive sequence, this relationship can be explained by considering the phase shift between phases of harmonics of order h:

$$\begin{aligned}
&\text{Phase a} : h \cdot 0^\circ \\
&\text{Phase b} : h \cdot -120^\circ \\
&\text{Phase c} : h \cdot +120^\circ \ (= h \cdot -240^\circ)
\end{aligned}$$

Taking the third harmonic as an example, there is no phase shift between phases, thus the third harmonics are ideally only in the zero sequence. The existence of third order harmonics in the line current is then governed by zero-sequence impedance, which implies the third harmonic current does not flow in the lines of delta or ungrounded systems.

Similarly, it can be verified that in a balanced power system the fifth harmonics are in the negative sequence, the seventh harmonics are in the positive sequence and so on [15].

2.2 Harmonic Resonance

Harmonic resonances influence on harmonic propagation and distortion levels in power systems. Resonances are characterised by energy exchange between capacitive and inductive elements in a circuit, hence at least one capacitive and one inductive element must be present in a circuit for resonance to occur. Reactances of capacitors and inductors can be expressed respectively as

$$X_C = \frac{-1}{\omega C}$$
$$X_L = \omega L$$

where ω has a unit of rad/s and is equal to $2\pi f$ where f is frequency in Hz. Hence it is immediately clear that reactances vary with frequency.

Two types of harmonic resonance can occur in electrical circuits: parallel resonance and series resonance. A parallel resonance is exemplified by the circuit in Figure 2.1. The equivalent reactance of the parallel connected capacitor and inductor is given by

$$X_{eq,parallel} = X_C || X_L = \frac{-\frac{1}{\omega C} \cdot \omega L}{-\frac{1}{\omega C} + \omega L} = \frac{\omega L}{1 - \omega^2 LC} \tag{2.2}$$

At the resonance frequency the denominator of (2.2) approaches zero. Hence the equivalent reactance becomes infinitely high, forcing any harmonic current to flow through the resistor. A parallel resonance thus presents a high impedance to harmonic current close to the resonance frequency. Presence of harmonic current close to the parallel resonance frequency can excite the resonance and cause substantial voltage distortion.

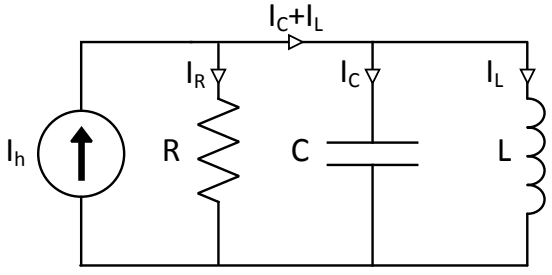

FIGURE 2.1: Parallel resonant circuit. The current $(I_C + I_L)$ is forced to zero near the resonance frequency, hence any harmonic current I_h must flow through resistor R, which causes voltage distortion.

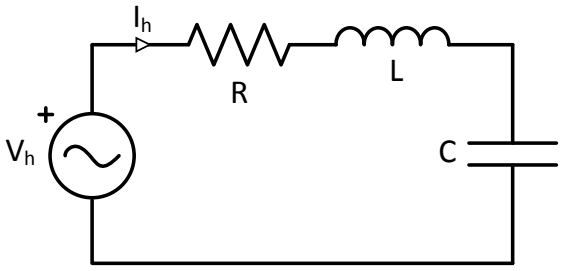

FIGURE 2.2: Series resonant circuit. At the resonance frequency the equivlaent reactance is zero and the flow of current is only a opposed by the resistor. Hence a small harmonic voltage can cause large current distortion.

A series resonance is illustrated by Figure 2.2. The equivalent reactance is given by

$$X_{eq,series} = X_L + X_C = \omega L - \frac{1}{\omega C} = \frac{\omega^2 LC - 1}{\omega C} \tag{2.3}$$

At the resonance frequency the nominator of (2.3) approaches zero. Hence the equivalent reactance goes to zero, and the flow of harmonic current is opposed only by the resistor. A series resonance thus presents a low impedance path for harmonic currents, and can be excited by a small harmonic voltage of frequency close to the resonance.

Comparing (2.2) and (2.3), it is clear that the resonance frequency is the same regardless of the type of resonance,

$$f_{res} = \frac{1}{2\pi\sqrt{LC}} \quad [\text{Hz}] \tag{2.4}$$

In the per unit system, inductive reactance can be expressed as $X_L = hX_1$ where X_1 is the fundamental frequency per unit reactance, and h is harmonic number. Similarly, capacitive reactance can be expressed as $1/(hB_1)$, where B_1 is the fundamental frequency capacitive susceptance. The per unit resonance frequency, i.e. the harmonic number of the resonance, can then be expressed as,

$$f_{res,pu} = \sqrt{\frac{1}{X_1 B_1}} \quad [\text{pu}] \tag{2.5}$$

A resonance frequency is also the frequency where the inductive reactance and capacitive reactance are equal in magnitude and opposite in sign.

2.3 Methods of Harmonic Analysis

A variety of techniques are available for harmonic analysis in power systems. This thesis focuses primarily on resonance analysis. Because such analysis is usually conducted as part of a broader harmonic study, its relation to techniques such as harmonic

power flow and time variant (EMT) analysis is also given some consideration. A general overview of harmonic analysis methods is given in Figure 2.3, dividing them into four main categories. Descriptions of all these forms of harmonic analysis are available in literature [12, 14, 16, 17].

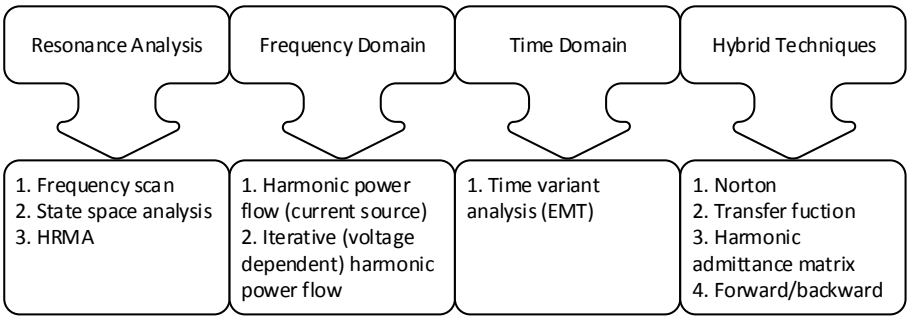

FIGURE 2.3: Classification of harmonic analysis methods [16]

Both the frequency scan method and the HRMA are forms of resonance analysis which are strongly related to the admittance matrix and its variation with frequency for the power system of interest. The nodal admittance matrix of a power system at frequency f is of the form

$$[Y_f] = \begin{bmatrix} Y_{11} & Y_{12} & \cdots & Y_{1i} & \cdots & Y_{1j} & \cdots & Y_{1n} \\ Y_{21} & Y_{22} & \cdots & Y_{2i} & \cdots & Y_{2j} & \cdots & Y_{2n} \\ \vdots & \vdots & \ddots & \vdots & \cdots & \vdots & \ddots & \vdots \\ Y_{i1} & Y_{i2} & \cdots & Y_{ii} & \cdots & Y_{ij} & \cdots & Y_{in} \\ \vdots & \vdots & \ddots & \vdots & \ddots & \vdots & \ddots & \vdots \\ Y_{j1} & Y_{j2} & \cdots & Y_{ji} & \cdots & Y_{jj} & \cdots & Y_{jn} \\ \vdots & \vdots & \ddots & \vdots & \ddots & \vdots & \ddots & \vdots \\ Y_{n1} & Y_{n2} & \cdots & Y_{ni} & \cdots & Y_{nj} & \cdots & Y_{nn} \end{bmatrix} \tag{2.6}$$

where y_{ji} is the mutual admittance between buses j and i, and Y_{ii} is the self-admittance of bus i [12]. The admittance matrix defines the relation between bus voltages and currents at any frequency f:

$$[V_f] = [Y_f]^{-1}[I_f] \tag{2.7}$$

$$[I_f] = [Y_f][V_f] \tag{2.8}$$

A parallel resonance corresponds to some elements of $[V_f]$ being large when a per unit current of frequency f is applied at any busbar. A series resonance corresponds to some

elements of $[I_f]$ being large when applying a voltage with frequency f at any busbar.

Frequency Scan

The first step in a harmonic study often involves carrying out frequency scans. This method, which is also called frequency sweep or impedance/admittance frequency response, requires a minimum of input data. It is effective for detection of harmonic resonance, and is also widely used for filter design [14].

By injecting a one per unit current, the measured voltage magnitude and phase angle at bus i corresponds to the driving point impedance at frequency f,

$$Z_{ii}(f) = \frac{V_i(f)}{I_i(f)}$$

This process can be can be repeated at discrete frequencies throughout the range of interest in order to obtain the impedance frequency response. Mathematically, this corresponds to calculating the the diagonal elements of the impedance matrix, i.e. diagonal elements of $[Y]^{-1}$. For example, the driving point impedance at bus i corresponds to the diagonal element at position ii of the impedance matrix [18]. The admittance frequency response can be obtained by sweeping the frequency of a one per unit voltage and measuring the current, i.e.

$$Y_{ii}(f) = \frac{I_i(f)}{V_i(f)}$$

Impedance and admittance frequency responses are presented as plots showing the magnitude and phase angle as functions of frequency. Sharp peaks in impedance magnitude (or valleys in admittance) are indicative of parallel resonance, while sharp valleys in impedance (or peaks in admittance) are indicative of series resonance.

Frequency scans can be performed with phase or sequence components. If all three phases are represented, a set of positive or zero sequence currents may be injected into three phases of a bus to obtain the positive or zero-sequence driving point impedance respectively [12].

Frequency scans are qualitative in nature as they say little about the actual distortion in the power network in the presence of harmonic sources. Moreover they consider only driving impedance, not transfer impedances. For example, consider the circuit of Figure 2.4. It may be verified that equivalent impedance seen from bus 1 at the fifth harmonic frequency is zero, which indicates a series resonance. However, the impedance between bus 1 and bus 2 is equal to $-j0.5$ at this frequency. Consequently a 5^{th} harmonic current at bus 1 can cause severe voltage distortion at bus 2, with little voltage distortion

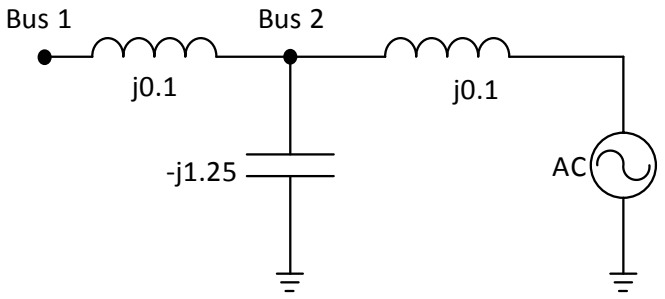

FIGURE 2.4: Impedances are given in per unit at fundamental frequency. At the fifth harmonic frequency there is a series resonances seen from bus 1. Becuase of the non-zero transfer impedance between bus 1 and bus 2, a fifth harmonic current at bus 1 can drive voltage distortion at bus 2 [17].

at bus 1. Frequency scans are therefore used for quick screening and as a supplement, not as substitute, to more formal harmonic power flow studies. The latter quantify the actual harmonic distortion under given operating conditions [17].

Harmonic Power Flow

The simplest form of harmonic power flow, sometimes referred to as Current Source Method, can be considered an extension of the frequency sweep. For frequency scan, current is injected and voltage measured at one bus at the time. A current source harmonic power flow is carried out at some harmonic frequency by specifying all the injected currents at that frequency in the vector $[I_f]$ of (2.7), and then solving for the resulting harmonic voltage vector $[V_f]$. This concept can be expanded to include multiple harmonic sources modelled as either current or voltage source. However, this kind of power flow analysis requires the harmonic injections to be predetermined, i.e. given as input to the simulation. More advanced forms of the power flow uses iterative methods and are able to capture the voltage dependency of many harmonic sources [14, 17]. The harmonic power flow is typically repeated at all frequencies of interest, hence estimating the actual harmonic distortion in the presence of harmonic sources. The requirements in terms of input data can be quite extensive. Quantifying actual distortion in this manner is outside the scope of the thesis.

State Space Modal Analysis

In the field of power system analysis, modal analysis is best recognized as a technique for dynamic small signal stability analysis. The state space representation of a linear

system is written as

$$\dot{x} = Ax + Bu \tag{2.9}$$

where x is a vector of state variables referred to as state vector, A is the state matrix, B is the input matrix, and u is the external excitation input vector. The state space model of a linear electrical circuit can be formulated by selecting inductor currents and capacitor voltages as state variables. Solving the differential equations yields a time domain transient response given by

$$x(t) = e^{A(t-t_0)}x(t_0) + \int_{t_0}^{t} e^{A(t-\tau)}Bu(\tau)d\tau \tag{2.10}$$

where e^A must be determined using eigendecomposition.

Eigenvalues of the state matrix A are the system modes. The number of modes is equal to the rank of the state matrix. Complex eigenvalues can only exist as complex conjugate pairs, and such a pair is often referred to as an oscillatory mode. The complex modes are of the form

$$\lambda_A = \sigma_A \pm j\omega_A \tag{2.11}$$

where σ_A is a mode damping coefficient with unit $1/s$, and ω_A describes the mode damped frequency with unit rad/s. A 2^{nd} order system has 2 eigenvalues, and assuming they are a complex conjugate pair as given by (2.11), a small disturbance will lead to oscillation of the state variables with a frequency determined by ω_A and a damping time-constant of $1/\sigma_A$,

$$\mathbf{x}(t) = K_1 e^{-\sigma_A t}\cos(\omega_A t - \phi) \tag{2.12}$$

where K_1 is a constant and ϕ represents a phase lag. For a higher order system with more than one oscillatory mode, the small disturbance response will be a linear combination of oscillatory responses determined by the modes [6].

As seen, the modes of the state matrix characterise the transient response of the system. The modes also indicate the stability margin of a system when subject to a small disturbance. This kind of modal analysis forms the basis for small signal stability analysis [19]. If there is a disturbance with a frequency close the ω_A of an oscillatory mode, the system transient response tends to be strong. From this perspective, the oscillatory modes can also be used to characterise resonance frequencies. However, the natural frequency ω_A is the same as impedance resonance frequency only for small values of σ_A [6].

2.4 Harmonic Resonance Mode Analysis (HRMA)

There are many applications of modal decomposition and eigenvalue analysis in the field of power system analysis. Eigenvalue analysis can be applied when the system description is based on linear differential equations as well as when the system description is based on algebraic equations. The application in state space analysis has already been mentioned (linear differential equations). Another well-known application of modal decomposition is in the representation of three-phase systems using symmetrical components (algebraic equations). Application is also found in voltage stability analysis, where eigenvalues of the Jacobian matrix (algebraic equations) can be used to quantify the voltage stability margin [5, 19]. HRMA is a form of eigenvalue analysis applied to a system description based on algebraic equations.

It has been found that parallel resonance phenomena is associated to frequencies at which the nodal admittance matrix approaches singularity, which is equivalent to an eigenvalue of the matrix approaching zero. Hence it has been suggested that eigenvalues and associated eigenvectors at such critical frequencies contain information about parallel resonances which can enhance understanding of resonance phenomena and assist in resonance mitigation. The idea of using a modal decomposition of the Y-bus matrix for harmonic resonance analysis was introduced by Xu et al. [5]. The concept was expanded upon by Huang et al. [6], Cui et al. [7, 20], and Hu et al. [8]. Theory and notation regarding HRMA presented in this thesis originates primarily from these papers. Application examples of HRMA can be found in the aforementioned papers, as well as in papers dedicated to exploring particular types of networks, such as distribution networks [21], offshore collection and transmission networks for wind power plants [22–24] and wave power plants [25].

Eigendecomposition

The term *right eigenvector* refers to a column vector t which is placed to the right of matrix A in the defining equation

$$At = \lambda t \tag{2.13}$$

where λ is the eigenvalue associated with the eigenvector. The term *left eigenvector* refers to a row vector l which must be placed to the left of the matrix A in the defining equation

$$lA = l\lambda \tag{2.14}$$

An admittance matrix is symmetric as long as the phase shifting effect of transformers is neglected. The non-conjugate transpose og an admittance matrix Y is therefore equal

to itself. It is therefore easily shown that the (non-conjugate) transpose of any right eigenvector t is equal to a left eigenvector l:

$$(Yt)^T = (t\lambda)^T \quad \Rightarrow \quad t^T Y = t^T \lambda \tag{2.15}$$

Eigendecomposition of an admittance matrix can thus be written as

$$[Y] = [L][\Lambda][T] \tag{2.16}$$

where $[\Lambda]$ is the diagonal eigenvalue matrix, $[L]$ consists of columns of eigenvectors, and $[T]$ consists of rows of eigenvectors, i.e

$$[L] = [T]^T = \left[\begin{array}{c|c|c|c} \vdots & \vdots & \cdots & \vdots \\ l_1 & l_2 & \cdots & l_n \\ \vdots & \vdots & \cdots & \vdots \end{array}\right] \tag{2.17}$$

One can conclude that $[L] = [T]^{-1} = [T]^T$ and vice versa.

The symmetric admittance matrix used in power system analysis is defined by

$$[V_f] = [Y_f]^{-1}[I_f] \tag{2.7 revisited}$$

where $[V_f]$ and $[I_f]$ are the nodal voltage and current vectors respectively at frequency f. The subscript f is dropped for simplicity in the following. Substituting (2.16) into (2.7) yields,

$$[V] = [T]^{-1}[\Lambda]^{-1}[L]^{-1}[I] = [L][\Lambda]^{-1}[T][I]$$

or

$$[T][V] = [\Lambda]^{-1}[T][I] \tag{2.18}$$

Defining the modal voltage vector $[U] = [T][V]$ and modal current vector $[J] = [T][I]$, (2.18) can be simplified to

$$[U] = [\Lambda]^{-1}[J]$$

which in expanded form is given by

$$\begin{bmatrix} U_1 \\ U_2 \\ \vdots \\ U_n \end{bmatrix} = \begin{bmatrix} \lambda_1^{-1} & 0 & 0 & 0 \\ 0 & \lambda_2^{-1} & 0 & 0 \\ 0 & 0 & \ddots & 0 \\ 0 & 0 & 0 & \lambda_n^{-1} \end{bmatrix} \begin{bmatrix} J_1 \\ J_2 \\ \vdots \\ J_n \end{bmatrix} \tag{2.19}$$

The kth modal impedance is defined as

$$Z_{m,k} = \frac{1}{\lambda_k} \tag{2.20}$$

A small eigenvalue λ_k will result in a large modal impedance $Z_{m,k}$, in which case a small modal current J_k at will lead to a large modal voltage U_k. This defines a parallel resonance in the modal domain. If the system has no damping, the admittance matrix becomes singular at resonance frequencies, which is equivalent to having an eigenvalue of zero, or an infinite modal impedance. There is no cross-coupling between the n equations given by (2.19), hence the excitation of one mode only affects a single modal voltage.

One important consideration is that the modal problem formulation of (2.19) is only suitable for detection and analysis of parallel resonances. There is no direct link between the eigenvalues of the admittance matrix and series resonances. Im many cases the behaviour of harmonic sources closely resemble that of a current sources, hence parallel resonances are most critical. However, there is an alternative system description which can be used to analyse series resonances. Such a description is given by

$$[E] = [Z_{loop}][I_{loop}] \tag{2.21}$$

where $[E]$ is the loop voltage vector, $[Z_{loop}]$ is the loop impedance matrix, and $[I_{loop}]$ is the loop current vector. The eigendecomposition of $[Z_{loop}]$ can be obtained in a similar manner to the Y-bus matrix for analysis of series resonance [5]. However, HRMA for parallel resonance analysis has been developed much further than for series resonance analysis. Only the formulation suitable for analysis of parallel resonances is considered further in this thesis.

Modal Participation Factors

Let us assume the eigenvalue λ_1 of (2.19) to be very small at some frequency associated to a parallel resonance. The modal current vector is related to the current vector $[I]$ by $[J] = [T][I]$. The modal current J_1 is therefore given by

$$J_1 = T_{11}I_1 + T_{12}I_2 + T_{13}I_3 + \cdots + T_{1n}I_n \tag{2.22}$$

where $T_{1,n}$ is the n-th element of the eigenvector associated with λ_1. This means the eigenvector associated with λ_1 determines controllability, i.e. contribution of each nodal current to the modal current J_1. The nodal bus voltages are related to the modal

voltages by $[V] = [L][U]$, or

$$\begin{bmatrix} V_1 \\ V_2 \\ \vdots \\ V_n \end{bmatrix} = \begin{bmatrix} L_{11} \\ L_{21} \\ \vdots \\ L_{n1} \end{bmatrix} U_1 + \begin{bmatrix} L_{12} \\ L_{22} \\ \vdots \\ L_{n2} \end{bmatrix} U_2 + \cdots + \begin{bmatrix} L_{1n} \\ L_{2n} \\ \vdots \\ L_{nn} \end{bmatrix} U_n \approx \begin{bmatrix} L_{11} \\ L_{21} \\ \vdots \\ L_{n1} \end{bmatrix} U_1 \tag{2.23}$$

where $L_{n,1}$ is the n-th element of the eigenvector associated to λ_1. The approximation of (2.23) holds because U_1 has a much larger value than the other modal voltages at the resonance associated to the small value of λ_1. The eigenvector associated to λ_1 thus also determines observability, i.e. reveals how observable the modal voltage U_1 is in each of the nodal voltages. The left and right eigenvectors associated to an eigenvalue are non-conjugate transpose of each other, hence the bus that has highest controllability of a modal resonance also has the highest observability of the same modal resonance.

The index of participation factor combines the observability and controllability of modes.

$$\begin{aligned} [V] = [L][\Lambda]^{-1}[T][I] &= [L] \begin{bmatrix} \lambda_1^{-1} & 0 & 0 & 0 \\ 0 & \lambda_2^{-1} & 0 & 0 \\ 0 & 0 & \ddots & 0 \\ 0 & 0 & 0 & \lambda_n^{-1} \end{bmatrix} [T][I] \\ &\approx \begin{bmatrix} L_{11} & L_{12} & \cdots & L_{1n} \\ L_{21} & L_{22} & \cdots & L_{2n} \\ \cdots & \cdots & \cdots & \cdots \\ L_{n1} & L_{n2} & \cdots & L_{nn} \end{bmatrix} \begin{bmatrix} \lambda_1^{-1} & 0 & 0 & 0 \\ 0 & 0 & 0 & 0 \\ 0 & 0 & 0 & 0 \\ 0 & 0 & 0 & 0 \end{bmatrix} \begin{bmatrix} T_{11} & T_{12} & \cdots & T_{1n} \\ T_{21} & T_{22} & \cdots & T_{2n} \\ \cdots & \cdots & \cdots & \cdots \\ T_{n1} & T_{n2} & \cdots & T_{nn} \end{bmatrix} [I] \\ &= \lambda_1^{-1} \begin{bmatrix} L_{11}T_{11} & L_{11}T_{12} & \cdots & L_{11}T_{1n} \\ L_{21}T_{11} & L_{21}T_{12} & \cdots & L_{21}T_{1n} \\ \cdots & \cdots & \cdots & \cdots \\ L_{n1}T_{11} & L_{n1}T_{12} & \cdots & L_{n1}T_{1n} \end{bmatrix} \begin{bmatrix} I_1 \\ I_2 \\ \cdots \\ I_n \end{bmatrix} \end{aligned} \tag{2.24}$$

The approximation is made possible because the critical mode impedance, $1/\lambda_1$, is much larger than the other modal impedances. The diagonal elements of the above matrix are the nodal participation factors in the critical mode. They can be defined as $PF_{ik} = L_{ik}T_{ki}$, where i is the bus number and k is the modal impedance number.

The magnitude of a modal impedance is only meaningful in a physical sense when considered in conjunction with participation factors. The driving point impedances seen from bus i at some frequency can be expressed via participation factors and eigenvalues

at that frequency:

$$\begin{aligned} Z_{ii} &= \frac{1}{\lambda_1}PF_{i1} + \frac{1}{\lambda_2}PF_{i2} + \frac{1}{\lambda_3}PF_{i3} + \cdots + \frac{1}{\lambda_n}PF_{in} \\ &= Z_{m,1}PF_{i1} + Z_{m,2}PF_{i2} + Z_{m,3}PF_{i3} + \cdots + Z_{m,n}PF_{in} \end{aligned} \tag{2.25}$$

Weighted Participation Factor (WPF) can be defined as:

$$WPF_{ik} = Z_{m,k}PF_{ik} \tag{2.26}$$

where i is bus number and k is modal impedance number. Expressing (2.25) in terms of WPFs yields,

$$Z_{ii} = WPF_{i1} + WPF_{i2} + WPF_{i3} + \cdots + WPF_{in} \tag{2.27}$$

A resonance detected from driving point impedance scan at bus i can hence be considered a result of exciting one or more modal resonance modes.

Modal Impedance Sensitivity Index

In addition to participation factors, it has been suggested that the involvement of network components in modal resonances can be quantified using sensitivity indices. These indices indicate how much a modal resonance moves in the impedance-frequency plane following a small change in some network parameter α. The movement of a modal resonance in the three-dimensional f-Z-α domain following a small change of α is illustrated in Figure 2.5. The modal impedance sensitivity index quantifies vertical movement, while the frequency sensitivity index quantifies the horizontal movement in the frequency-impedance plane.

The sensitivity of the k-th eigenvalue of the Y-bus admittance matrix to some parameter α can be expressed as

$$\frac{\partial \lambda_k}{\partial \alpha} = t_k \frac{\partial Y}{\partial \alpha} l_k \tag{2.28}$$

where t_k is the k-th row eigenvector of $[T]$ and l_k is the k-th column eigenvector of $[L]$. This equation suggests the sensitivity of an eigenvalue with respect to some parameter α can be obtained to evaluating the sensitivity of the admittance matrix to the same parameter.

Let's initially consider the evaluation of (2.28) with respect to a *shunt admittance* at bus i given by $y_{sh,i}$. The i-th diagonal element of $\frac{\partial Y}{\partial \alpha}$ takes on value 1, with all other

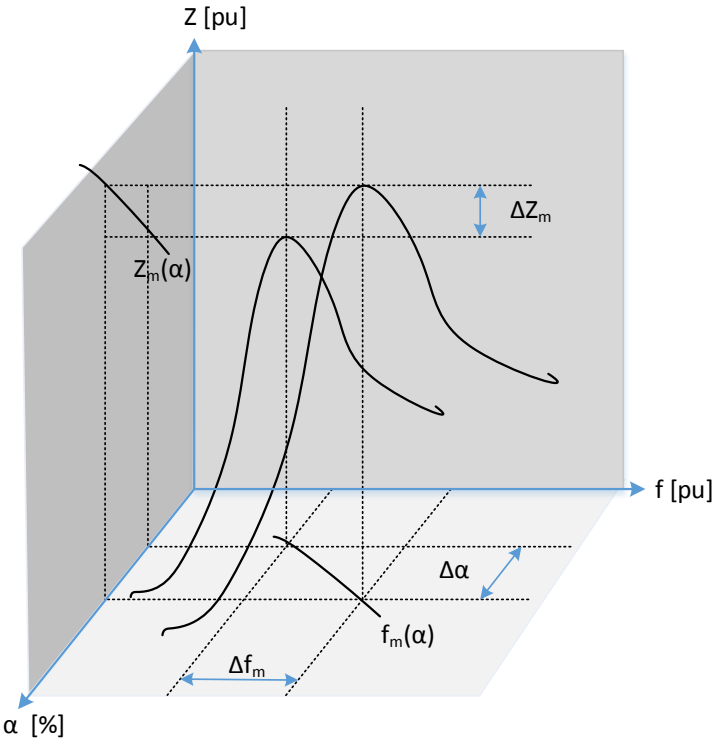

FIGURE 2.5: The small change $\Delta\alpha$ of some network parameter α causes a the modal resonance peak to move a vertical distance ΔZ_m and a horisontal distance Δf_m in the three dimensional f-Z-α domain [7].

elements being zero. For a shunt admittance at bus 2, this yields

$$\frac{\partial Y}{\partial y_{sh,2}} = \begin{bmatrix} 0 & 0 & \cdots & 0 \\ 0 & 1 & \cdots & 0 \\ \vdots & \vdots & \ddots & \vdots \\ 0 & 0 & 0 & 0 \end{bmatrix}$$

Now consider evaluation of (2.28) with respect to a *series admittance* between bus i and bus j. Four elements of $\frac{\partial Y}{\partial \alpha}$ take in non-zero values, e.g. for a *series admittance* between bus 1 and bus 2,

$$\frac{\partial Y}{\partial y_{se,1-2}} = \begin{bmatrix} 1 & -1 & \cdots & 0 \\ -1 & 1 & \cdots & 0 \\ \vdots & \vdots & \ddots & \vdots \\ 0 & 0 & 0 & 0 \end{bmatrix}$$

Defining the sensitivity matrix with respect to eigenvalue λ_k,

$$S_k = l_k t_k = \begin{bmatrix} \vdots \\ \vdots \\ L_{jk} \\ \vdots \end{bmatrix} \begin{bmatrix} \cdots & \cdots & T_{ki} & \cdots \end{bmatrix} = \begin{bmatrix} \cdots & \cdots & \cdots & \cdots \\ \vdots & \ddots & \cdots & \cdots \\ \vdots & \vdots & L_{jk}T_{ki} = s_{k,ji} & \cdots \\ \vdots & \vdots & \cdots & \cdots \end{bmatrix} \tag{2.29}$$

The eigenvalue sensitivity of mode k to a shunt branch at bus i is given by

$$\frac{\partial \lambda_k}{\partial y_{sh}} = t_k \frac{\partial Y}{\partial y_{sh}} l_k = t_k \frac{\partial Y}{\partial Y_{ii}} \frac{\partial Y_{ii}}{\partial y_{sh,i}} l_k = s_{k,ii} \tag{2.30}$$

Hence the sensitivity of eigenvalue k with respect to shunt admittance branches at defined buses are given by the diagonal elements of the sensitivity matrix S_k. The diagonal elements of this matrix are in fact the same as bus participation factors. The eigenvalue sensitivity with respect to a series admittance branch between bus i and bus j can be expressed as

$$\frac{\partial \lambda_k}{\partial y_{se,ij}} = t_k \frac{\partial Y}{\partial y_{se,ij}} l_k = s_{k,ii} + s_{k,jj} - s_{k,ij} - s_{k,ji} \tag{2.31}$$

Admittances y_{sh} and y_{se} and eigenvalues λ_k are complex numbers. However, it is the sensitivity of $|\lambda_k|$, i.e. the sensitivity of the absolute value which is of primary interest. Moreover, the derivative with respect to a complex number is somewhat confusing. Hence it is desirable to obtain the derivative of eigenvalue magnitude with respect to real and imaginary part of admittance. This can be done by defining

$$\begin{aligned} \lambda_k &= \lambda_r + j\lambda_i, & S_k &= S_r + jS_i \\ y &= G_{br} + jB_{br} & F &= |\lambda_k|^2 \end{aligned}$$

where S_k is either given by (2.30) or (2.31) depending on whether the branch in question is shunt or series connected. A change of ΔB_{br} results in a change ΔF which is given by

$$\begin{aligned} \Delta F &= |\lambda_k + \Delta\lambda_k|^2 - |\lambda_k|^2 = |(\lambda_r + j\lambda_i) + (S_r + jS_i)(j\Delta B_{br})|^2 - |(\lambda_r + j\lambda_i)|^2 \\ &= (\lambda_r - S_i \Delta B_{br})^2 + (\lambda_i - S_r \Delta B_{br})^2 - (\lambda_r^2 + \lambda_i^2) \\ &= 2(S_r\lambda_i - S_i\lambda_r)\Delta B_{br} + (S_r^2 + S_i^2)(\Delta B_{br})^2 \end{aligned}$$

Taking only the first order term and letting $\Delta B_{br} \to 0$,

$$\frac{\partial F}{\partial B_{br}} = 2(S_r\lambda_i - S_i\lambda_r)$$

Similarly

$$\frac{\partial F}{\partial G_{br}} = 2(S_r\lambda_r + S_i\lambda_i)$$

Converting back from F to $|\lambda_k|$ results in

$$\frac{\partial|\lambda_k|}{\partial G_{br}} = \frac{S_r\lambda_r + S_i\lambda_i}{\sqrt{\lambda_r^2+\lambda_i^2}} = \mu \tag{2.32}$$

$$\frac{\partial|\lambda_k|}{\partial B_{br}} = \frac{S_r\lambda_i - S_i\lambda_r}{\sqrt{\lambda_r^2+\lambda_i^2}} = \nu \tag{2.33}$$

Lets assume all branches in a harmonic study are fully representable by a series RLC branch with linear components (i.e. constant value of R, L and C). Any branch is then fully defined from its fundamental frequency value or resistance R_1, inductive reactance X_1 and capacitive susceptance B_1. The conductance and susceptance of the branch can be expressed from these properties.

$$G_{br} = \frac{R_1}{R_1^2 + \left(hX_1 - \frac{1}{hB_1}\right)^2} \tag{2.34}$$

$$B_{br} = \frac{\frac{1}{hB_1} - hX_1}{R_1^2 + \left(hX_1 - \frac{1}{hB_1}\right)^2} \tag{2.35}$$

In order to find the modal impedance sensitivity with respect to individual components of the RLC branch, one can employ the chain derivative rule.

$$\frac{\partial|\lambda_k|}{\partial\alpha} = \frac{\partial|\lambda_k|}{\partial G_{br}}\frac{\partial G_{br}}{\partial\alpha} + \frac{\partial|\lambda_k|}{\partial B_{br}}\frac{\partial B_{br}}{\partial\alpha} = \mu\frac{\partial G_{br}}{\partial\alpha} + \nu\frac{\partial B_{br}}{\partial\alpha} \tag{2.36}$$

where α can be R_1, X_1 or B_1 [7, 8]. Mathematical expressions for the derivative of (2.34) and (2.34) with respect to X_1 and B_1 have been obtained using Maple software from Maplesoft. These expressions are included in Appendix B.

The modal impedance sensitivity index can be expressed as

$$\frac{\partial Z_{m,k}}{\partial\alpha} = \frac{\partial Z_{m,k}}{\partial|\lambda_k|}\frac{\partial|\lambda_k|}{\partial\alpha} = -\frac{1}{|\lambda_k|^2}\frac{\partial|\lambda_k|}{\partial\alpha} \tag{2.37}$$

The modal impedance sensitivity can be normalised for easier comparison of network components with different units. Dropping the subscript k for generality,

$$\frac{\partial Z_m}{\partial\alpha}\Big|_{norm} = \frac{\frac{\partial Z_m}{Z_m}}{\frac{\partial\alpha}{\alpha}} = -\frac{\partial|\lambda|}{\partial\alpha}\cdot\frac{\alpha}{|\lambda|} \quad \left[\frac{\%}{100\,\%}\right] \tag{2.38}$$

The unit of the normalised sensitivity index used in this thesis is percent change of modal impedance per 100 percent change of network parameter.

Modal Frequency Sensitivity Index

An important realisation is that the magnitude of a modal impedance near resonance is mainly influenced by resistive and not reactive components of participating branches. For example, in the simple circuit of Figure 2.1, the impedance is purely resistive at the resonance frequency,

$$Z_m = \frac{1}{\lambda} = \frac{1}{\frac{1}{R} + j(\omega C - \frac{1}{\omega L})} = R$$

i.e. the (modal) impedance magnitude is purely a function of resistance R. On the contrary the resonance frequency of the circuit in Figure 2.1 is determined exclusively by the reactive components L and C, as given by (2.4). A frequency sensitivity index, $\partial f/\partial \alpha$ which quantifies the change in resonance frequency with respect to a network component has therefore also been suggested in literature. Such an index is possible to develop, though its calculation becomes more complicated than the modal impedance sensitivity index.

Derivation of the frequency sensitivity index begins with defining a resonance peak of some modal impedance frequency response at frequency $f_{res,1}$,

$$\frac{\partial Z_m}{\partial f}\Big|_{\substack{f=f_{res,1}\\ \alpha=\alpha_1}} = 0 \tag{2.39}$$

The linear Taylor expansion of this expression around the modal impedance peak is given by

$$\frac{\partial Z_m}{\partial f}\left(f_{res,1} + \Delta f, \alpha_1 + \Delta\alpha\right) = \left(\frac{\partial Z_m}{\partial f} + \frac{\partial^2 Z_m}{\partial^2 f}\Delta f + \frac{\partial^2 Z_m}{\partial f \partial \alpha}\Delta\alpha\right)\Big|_{\substack{f=f_{res,1}\\ \alpha=\alpha_1}} \tag{2.40}$$

A small change $\Delta\alpha$ in the magnitude of α will cause a shift of the resonance frequency. This new modal impedance peak can be defined as

$$\frac{\partial Z_m}{\partial f}\Big|_{\substack{f=f_{res,1}+\Delta f_{res}\\ \alpha=\alpha_1+\Delta\alpha}} = 0 \tag{2.41}$$

Expressing (2.41) with the linear Taylor expansion of (2.40) and simplifying with (2.39) yields

$$\frac{\partial f_{res}}{\partial \alpha} = \frac{\Delta f_{res}}{\Delta \alpha} = -\frac{\frac{\partial^2 Z_m}{\partial f \partial \alpha}}{\frac{\partial^2 Z_m}{\partial^2 f}} = -\frac{\frac{\partial^2 |\lambda|}{\partial f \partial \alpha}}{\frac{\partial^2 |\lambda|}{\partial^2 f}} \tag{2.42}$$

The denominator of (2.42), i.e. the second-order derivative of the eigenvalue with respect to frequency can be calculated numerically during the modal impedance scan process. Considering the eigenvalues are calculated at discrete frequencies with step length of Δf,

$$\frac{\partial^2|\lambda|}{\partial^2 f} = \frac{1}{4\Delta f^2}\left(|\lambda|_{f+2\Delta f} + |\lambda|_{f-2\Delta f} - 2|\lambda|_f\right) \tag{2.43}$$

where subscripts denote at which discrete frequency the eigenvalue is obtained relative to the current discrete frequency f.

The nominator of (2.42) can be approximated from the derivative with respect to frequency of

$$\frac{\partial|\lambda|}{\partial\alpha} = \frac{\partial|\lambda|}{\partial G_{br}}\frac{\partial G_{br}}{\partial\alpha} + \frac{\partial|\lambda|}{\partial B_{br}}\frac{\partial B_{br}}{\partial\alpha} \tag{2.36 revisited}$$

which yields

$$\frac{\partial^2|\lambda|}{\partial f\partial\alpha} = \frac{\partial\mu}{\partial f}\frac{\partial G_{br}}{\partial\alpha} + \mu\frac{\partial^2 G_{br}}{\partial f\partial\alpha} + \frac{\partial\nu}{\partial f}\frac{\partial B_{br}}{\partial\alpha} + \nu\frac{\partial^2 B_{br}}{\partial f\partial\alpha} \tag{2.44}$$

Expressions μ and ν are defined in (2.32) and (2.33) respectively. The terms $\partial\mu/\partial f$ and $\partial\nu/\partial f$ can be obtained numerically during the modal impedance scan process,

$$\frac{\partial\mu}{\partial f} = \frac{1}{2\Delta f}\left(\mu|_{f+\Delta f} - \mu|_{f-\Delta f}\right) \ , \quad \frac{\partial\nu}{\partial f} = \frac{1}{2\Delta f}\left(\nu|_{f+\Delta f} - \nu|_{f-\Delta f}\right) \tag{2.45}$$

The remaining terms in (2.44), i.e. $\partial G_{br}/\partial\alpha$, $\partial^2 G_{br}/\partial\alpha\partial f$, $\partial B_{br}/\partial\alpha$ and $\partial^2 B_{br}/\partial\alpha\partial f$ must be explicitly calculated depending on α and the kind if branch which is to be analysed. Again, many branches that are suitable for inclusion in a harmonic study can be fully represented by an RLC branch, in which case G_{br} and B_{br} can be expressed as in (2.34) and (2.35). Expressions for the remaining terms given the RLC branch assumption have been obtained using Maple, and are included in Appendix B.

The modal frequency sensitivity index can be normalised in order to facilitate comparison of network components with different units. The normalised modal frequency sensitivity index utilised in this thesis is defined as the per unit change of resonance frequency to a 100 percent change in parameter α. It can be expressed as

$$\left.\frac{\partial f_{res}}{\partial\alpha}\right|_{norm} = \frac{\partial f_{res}}{\frac{\partial\alpha}{\alpha}} = \frac{\partial f_{res}}{\partial\alpha}\cdot\alpha \quad \left[\frac{\text{pu}}{100\,\%}\right] \tag{2.46}$$

and is achieved simply by multiplication with the value α of the network component [7, 8].

2.5 Comparing Modal Analysis Techniques

As seen in the previous sections, both the state A matrix and the Y-bus admittance matrix can be used to analyse harmonic resonances. The oscillatory modes of A are of the form

$$\lambda_A = \sigma_A \pm j\omega_A \qquad \text{(2.11 revisited)}$$

The resonance modes in HRMA are each associated to a resonance frequency f_{res}, and a modal impedance Z_m. A comprehensive comparison of resonance analysis using HRMA and state state space analysis was carried out by Huang et al. [6]. It was shown that the resonance frequencies obtained from the state matrix A, termed ω_A and expressed in rad/s, coincide with those frequencies obtained from the Y-bus matrix, given by ω_Y in rad/s, only if damping index σ_A is zero or very close to zero. In addition, there is no simple relationship between the damping index of σ_A and the modal impedance Z_m. Hence there is no straightforward correspondence between the oscillatory modes of A and the resonance modes of the admittance matrix Y.

Distinct characteristics which separate the state space modal analysis technique and HRMA include:

- The modes of the A have a unit of 1/s and characterise the time-domain transient response of a network. On the contrary, modal variables of the Y-bus matrix have the unit of impedance (Ω or pu). The resonance modes of the admittance matrix characterise the electrical circuit in frequency domain.
- The admittance matrix is a nodal system description. This results in eigenvectors which carry additional information about nodal participation in resonance modes. A state space model is not a nodal description, hence the eigenvectors of A do not offer information about nodal participation in a resonance.
- The number of modes given by the state matrix is equal to the rank of A, and the oscillatory modes appear as discrete points in the frequency domain. The number of modal variables in HRMA is equal to the rank of the admittance matrix, and these variables are defined at all frequencies.
- Sensitivity indices for the oscillatory modes of A with respect to network components can be calculated as $\mathrm{d}\sigma_A/\mathrm{d}\alpha$ and $\mathrm{d}\omega_A/\mathrm{d}\alpha$. The sensitivity indices for modes of the Y-bus matrix are more elaborate to calculate, though it can be managed as shown in previous sections, or they can be estimated numerically.

In addition, there are modelling limitations with the state-space approach. In particular, network elements with distributed and frequency dependent parameters, such as

transmission lines and cables, are not easily included in the state-space network model, but can be highly important for accurate assessment of harmonic resonance. The representation of such impedances in the state matrix requires synthesizing equivalent RLC networks using special techniques such as vector fitting [26]. On the contrary, the admittance approach used in HRMA allows for recalculating the parameters of admittances at each discrete frequency, which makes it much easier to handle non-linearities and frequency dependency.

3 Modelling for Harmonic Resonance Studies

This chapter presents the modelling of power system components which are later included in HRMA of specific cases. The extent and level of detail in modelling of network components for harmonic studies depends on the analysis technique to be used, problem formulation, frequency range of interest, required accuracy of results and so on. Most HRMA presented in published papers assume linearity of network parameters, i.e. constant values of R, L and C over the frequency range of interest. This chapter present linear models as well as some effects which can cause non-linearities.

3.1 Overhead Lines and Cables

Multiphase cables and transmission lines can be represented with coupled π-equivalent circuits. Most power system analysis software aimed at harmonic and/or electromagnetic transient analysis contain modules for calculation of parameters based on physical arrangements specified by the user [15, 27]. Once the parameters of a line or cable are known, the admittance or impedance matrix describing phase to ground and mutual admittances/impedances can be constructed. For balanced studies, coupled π-equivalent models can be simplified into separate positive, negative and zero sequence π-equivalents as shown in Figure 3.1.

Two important considerations related to the electrical parameters of lines and cables are:

- The distribution of parameter along the line/cable length which yields so-called long line effects
- The frequency dependency of parameters due primarily to skin effect and earth return

If long line and frequency dependent effects of the electrical parameters are neglected, the positive sequence model parameters are given by the unit-length parameters multiplied

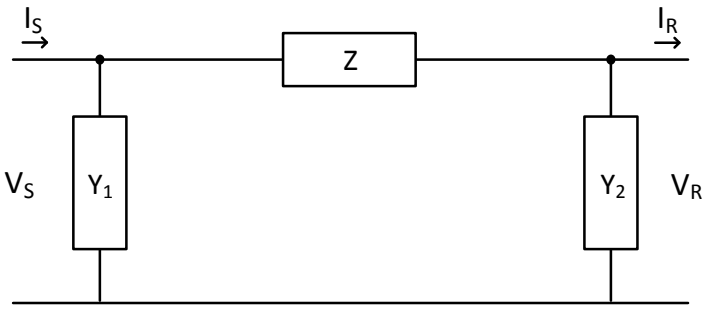

FIGURE 3.1: π-equivalent line/cable model. Subscripts $_S$ and $_R$ denote sending and receiving end respectively. For steady state analysis in frequency domain, the lumped parameters Z, Y_1 and Y_2 can be adjusted with long line correction factors to obtain exact representation of long line effects at a particular frequency.

by length. The total shunt admittance is simply divided equally between the two lumped shunt admittances. This is known as the nominal π-equivalent model.

$$\begin{aligned} Z_{nominal} &= R_1 + jhX_1 \\ Y_{1,nominal} &= Y_{2,nominal} = jhB_1/2 \end{aligned} \tag{3.1}$$

where R_1, X_1 and B_1 are the fundamental frequency values of total length resistance, inductive reactance and capacitive susceptance respectively.

The long line effects can be accounted for by including the long line hyperbolic correction factors.

$$\begin{aligned} Z_{exact} &= Z_0 \sinh(\gamma l) = Z_{nominal} \frac{\sinh(\gamma l)}{(\gamma l)} \\ Y_{1,exact} = Y_{2,exact} &= \frac{1}{Z_0} \tanh(\frac{\gamma l}{2}) = Y_{nominal} \frac{\tanh(\gamma l)}{(\gamma l/2)} \end{aligned} \tag{3.2}$$

where

$$\begin{aligned} \gamma &= \sqrt{zy} \\ Z_0 &= \sqrt{\frac{z}{y}} \end{aligned}$$

and z is the unit-length series impedance, y the unit-length shunt admittance, and l is the total length. The hyperbolic correction factors yield an exact representation of the long-line effects from the cable terminals at the frequency they are calculated for [28].

Skin effect forces alternating currents towards a conductors perimeter, resulting in current density which tapers off from conductor surface towards its centre. Frequency dependency of parameters due to skin and proximity effects is typically accounted for

by using frequency dependent correction factors. All line and cable parameters are frequency dependent, but the effect is most prominent in series resistance. In this thesis, the formula suggested by the National Grid Company is used for series resistance,

$$R = R_1(0.187 + 0.532\sqrt{h}, \quad h > 2.35) \tag{3.3}$$

where R_1 is fundamental frequency resistance, and h is harmonic order [12]. The corrected value of resistance R can then be applied in (3.2).

For calculations at power frequency involving overhead lines, it is often considered acceptable to neglect the shunt admittance for lines shorter than 80 km. A model consisting simply of the series impedances is therefore also known as the short line model. Similarly, the nominal π-equivalent is generally considered acceptable for line lengths up to 250 km at power frequency, hence it is known as the medium line model. Cables generally have much larger shunt capacitances than overhead lines, hence long line effects should be taken into account for much shorter cables. The long line effects are also much more prominent with higher frequencies, making short and medium length approximations less suited for harmonic studies [14, 29].

3.2 Transformers

The short circuit impedance, magnetizing characteristics and vector group (winding connections), are the main characteristics of transformers which impacts on harmonic flows. Transformers are typically modelled in positive sequence (and negative sequence) as T-equivalent circuits like the one shown in Figure 3.2.

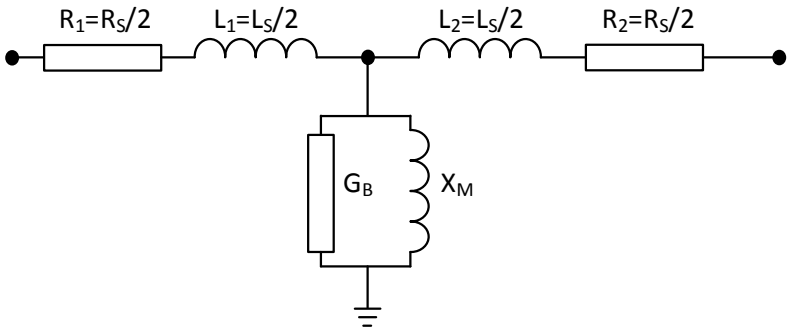

FIGURE 3.2: Transformer T model. Phase shifter due to vector group and harmonic current source for representation of transformer generated harmonics not shown.

For simplified resonance studies, the magnetizing branch may often be ignored, modelling the transformer only by its short-circuit impedance. If any kind of harmonic power flow, current source or iterative, involving more than a single harmonic source is to be carried out, transformers phase shift must be taken into account. The phase shift in transformers typically yields a high impedance in zero sequence, ideally resulting in cancellation of zero-sequence harmonics. Modelling of non-linear effects in transformers due to saturation can be achieved by having a voltage dependent current source in parallel with the magnetizing branch, but this is usually only included when transformer-generated harmonics are the primary concern [14, 29].

3.3 Aggregate Loads

An aggregate load refers to group of buses that are treated as a single network element for harmonic analysis. Typical aggregate loads are feeders seen from the substation of a distribution system, or a larger customer seen from the point of coupling. Such loads may provide the majority of damping component in distribution networks and also affect resonance conditions at higher frequencies. If there are harmonic sources of concern in these loads, they should not be treated as an aggregate load.

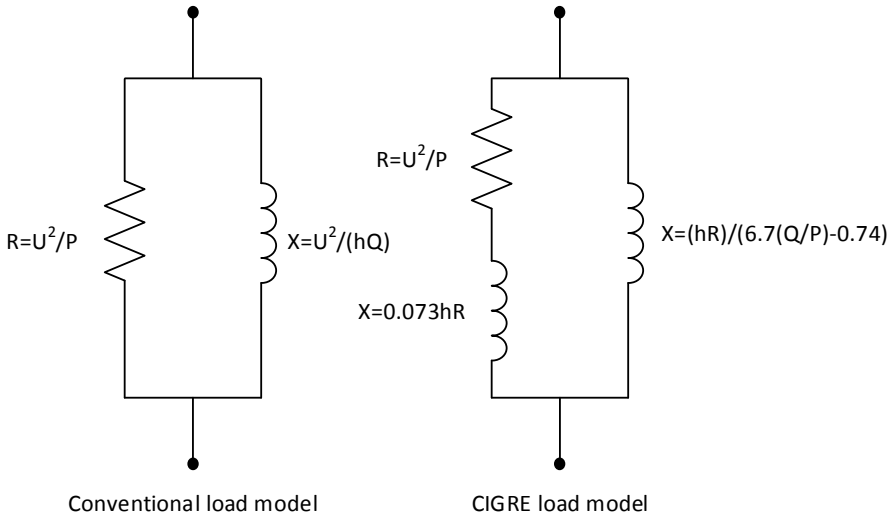

FIGURE 3.3: Aggregate load models for harmonic studies. Parameters are estimated using rated network voltages and stady state power flow.

A load model represents the impedance frequency response of the aggregate loads in a simplified way. The impedance response depends on the type of loads as well as the line or cable which feeds the loads. Consequently, the applicability of general aggregate load

models is quite limited. Nevertheless, suggested representations of aggregate loads are found in literature [29]. Two typical models found in literature are shown in Figure 3.3.

3.4 VSC Grid-side Harmonic Emission Filters

Voltage Source Converters (VSC) are utilised in full-scale converter wind turbines. When emissions and grid interaction of such converters are of concern, they need to be modelled accurately for harmonic studies.

The grid-side terminals of a WTG with full-scale converter is typically connected to the MV collector system via a coupling reactor with inductance L_{mr} and a step-up transformer with short circuit inductance L_{tr}. In addition there are shunt harmonic filters between the reactor and transformer as shown in Figure 3.4. The shunt harmonic filters are capacitive at fundamental frequency, and although the shunt harmonic filter topology can vary, such a combination of inductor L_{mr}, inductor L_{tr} and shunt harmonic filter can be said to constitute an LCL filter.

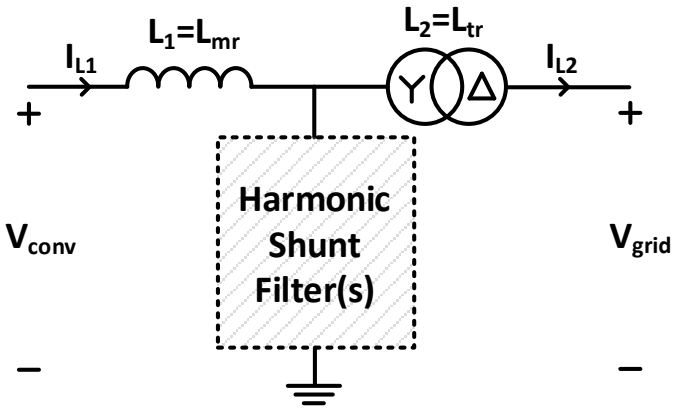

FIGURE 3.4: Basic filtering structure commonly used for grid-tied VSCs. The shunt harmonic filter, generally capcitive at fundametal frequency, can take on different topologies. Overall layout can be refered to as LCL filter.

There are a number of constraints in designing filtering solutions for grid connected converters. The filters must be designed not only to ensure compliance with relevant grid codes, but must also facilitate stable operation of the converter controllers. In the multi-megawatt power range, the capability of semi-conductor switches can further constrain parameters such as switching frequency and maximum DC voltage [30]. Moreover it is desirable to minimize energy losses, volume, weight and cost of the overall filtering solution. Due to increasing numbers of grid connected VSCs in modern power systems,

the optimisation of emission filters is a topic which is receiving attention in research [9, 10].

3.5 Harmonic Sources/Full-Scale VSC Wind Turbines

The classic approach for harmonic studies in frequency domain is to model harmonic sources as fixed ideal current sources. For many harmonic sources, such as line-commutated HVDC converters, this approximation is fairly accurate. However, the emission from other harmonic sources can be highly dependent on existing voltage distortion and controller interaction, in which case the ideal current source method can be insufficient [14, 17].

State of the art WTG harmonic models consist of a number of Norton or Thevenin equivalents with Norton or Thevenin impedance specified for every harmonic frequency of interest. Such models can be derived by the turbine manufacturer, which has full access to the converter control structure and settings. These models facilitate analysis of controller impact on resonances as well as analysis of countermeasures such as active filtering via the converter controller [31, 32].

Converter Control Interaction

In order to investigate the interaction between converter control and harmonic resonances, there is a need to represent the grid-side converter in frequency domain as seen from elsewhere in the network. A VSC with simplified current control and admittance as seen from the AC-side terminals of the converter is shown in Figure 3.5.

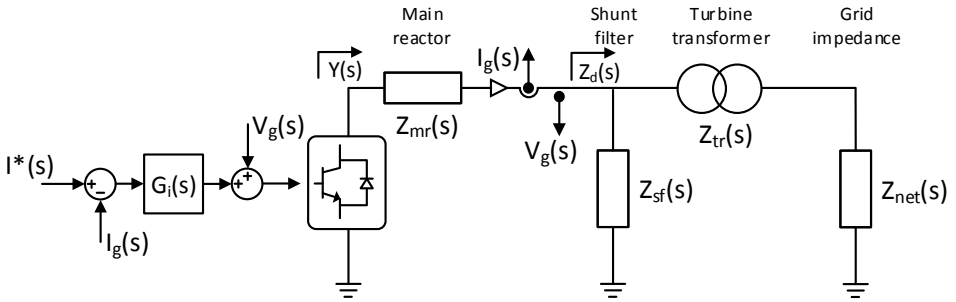

FIGURE 3.5: Grid-tied VSC (of WTG) with indication of current control loops and impedance as seen from converter terminals [33].

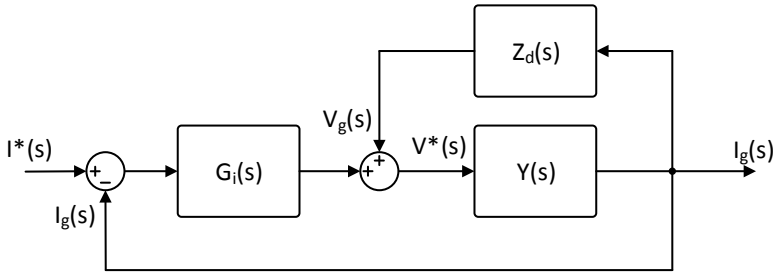

FIGURE 3.6: Current control loops with current feed-back and voltage feed-forward. The voltage feed-forward enhances disturbance rejection of the converter [33].

A typical current control structure with current feed-back and voltage feed-forward is shown in Figure 3.6. The open-loop transfer function can be obtained from the block diagram,

$$H_{ol}(s) = G_i(s)\frac{Y(s)}{1 - Y(s)Z_d(s)} \tag{3.4}$$

$G_i(s)$ is the transfer function of the current control, including any harmonic compensation, filtering and decoupling. The other transfer functions are defined as

$$Z_d(s) = (Z_{tr}(s) + Z_{net}(s)) \| Z_{sf}(s) \tag{3.5}$$

$$Y(s) = \frac{1}{Z_{mr}(s) + Z_d(s)} \tag{3.6}$$

The voltage feed forward can be combined with $Y(s)$ to obtain an equivalent system transfer function,

$$G_{sys}(s) = \frac{Y(s)}{1 - Z_d(s)Y(s)} = \frac{1}{Z_{mr}(s)} = \frac{1}{R_{mr}(1 + s\tau_{mr})} \tag{3.7}$$

where $\tau_{mr} = L_{mr}/R_{mr}$ is the time constant of the main reactor.

The stability of the current control loop can be evaluated based on the open loop transfer function (3.4). For such purposes the delay due to Pulse Width Modulation (PWM) and discrete sampling should also be represented. The stability can be evaluated using Nyquist stability criterion, and different operation conditions of the external grid can be considered by varying the impedance of $Z_{net}(s)$ [33].

From the current control structure it is possible to derive an average harmonic model which can represent the grid-tied VSC as seen from elsewhere in the network. Deviation from the ideal sinusoidal voltage waveform due to forcing external to the converter, i.e. background harmonic voltage, can be considered as a disturbance $V_g(s)$ acting on the process as shown in Figure 3.7 [33].

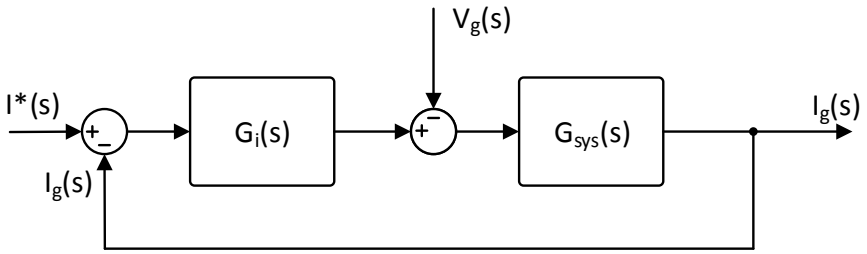

FIGURE 3.7: VSC current control loop with background harmonic voltage modelled as disturbance.

Neglecting PWM and sampling delays, the following relation can be obtained:

$$[(I^*(s) - I_g(s))G_i(s) - V_g]\, G_{sys}(s) = I_g(s) \tag{3.8}$$

Solving for current $I_g(s)$ yields

$$I_g(s) = G_c(s)I^*(s) - Y_{eq}(s)V_g(s) \tag{3.9}$$

where

$$Y_{eq}(s) = \frac{G_{sys}(s)}{1 + G_i(s)G_{sys}(s)} \qquad G_c(s) = G_i(s)Y_{eq}(s) = \frac{G_i(s)G_{sys}(s)}{1 + G_i(s)G_{sys}(s)} \tag{3.10}$$

Expressing the system transfer function $G_{sys}(s)$ via the main reactor impedance $Z_{mr}(s)$, $Y_{eq}(s)$ and $G_c(s)$ can alternatively be written as

$$Y_{eq}(s) = \frac{1}{Z_{mr}(s) + G_i(s)} \qquad G_c(s) = G_i(s)Y_{eq}(s) = \frac{G_i(s)}{Z_{mr}(s) + G_i(s)} \tag{3.11}$$

Equation (3.9) can be visualised as the Norton equivalent harmonic model in Figure 3.8 [34–36]. The Norton equivalent can easily be converted to a Thevenin equivalent if necessary.

The harmonic model of (3.9) does not represent switching harmonics of the converter itself, but rather represent the converter as seen from elsewhere in the network. Qualitatively, the current controller tends to have high open loop gain within the controller bandwidth, i.e. $|G_c(s)| \approx 1$ at lower frequencies. Above the controller bandwidth the current controller tends to have low gain, i.e. $|G_c(s)| \approx 0$, hence the converter acts like as passive component with admittance $Y_{eq}(s)$ [36].

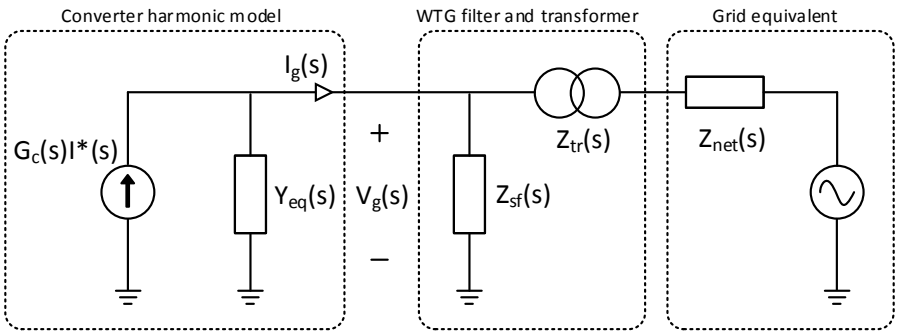

FIGURE 3.8: Norton equivalent harmonic model together with WTG filter, transformer and grid equivalent.

The current control loops can be implemented in a stationary or a synchronous reference frame. Regulating currents in stationary *abc* or $\alpha\beta$ reference frames with Proportional Integral (PI) regulators in theory should be effective. The transfer function of a PI-regulator is given by

$$G_{i,PI}(s) = K_p \left(1 + \frac{1}{T_i s}\right) \tag{3.12}$$

However, PI control of stationary reference frame currents is hampered by PWM and sampling delays which limits the maximum controller gain and hence leads to steady state tracking error. This issue is commonly addressed by transforming the phase currents into a synchronously rotating dq-reference frame and controlling the *d*- and *q*-axis currents. PI current regulators in synchronous *dq*-reference frame is essentially equivalent to a Proportional Resonant (PR) regulator in a stationary reference frame. The PR-regulator transfer function is given by

$$G_{i,PR}(s) = K_p \left(1 + \frac{s}{T_i(s^2 + \omega_0^2)}\right) \tag{3.13}$$

This (ideal) resonant regulator provides infinite gain at the tuned frequency ω_0, which is set equal to the fundamental frequency. Hence steady state tracking error can be eliminated. As frequency increases above the fundamental, the transfer function response of (3.13) approaches that of (3.12) [34]. It therefore seems reasonable to assume PI-regulator behaviour for harmonic frequencies.

Let's now approximate the positive sequence current to be regulated by a conventional PI-regulator. Any specific measures for harmonic rejection, filtering and decoupling in $G_i(s)$ are neglected. The equivalent impedance of the converter can from (3.11) be

written as,

$$\begin{aligned} Z_{eq}(s) &= \frac{1}{Y_{eq}(s)} = Z_{mr}(s) + G_i(s) \\ &= R_{mr}(1 + s\tau_{mr}) + K_p\left(1 + \frac{1}{T_i s}\right) \end{aligned} \tag{3.14}$$

It should be appreciated that the pole of the PI-regulator gives it a capacitive behaviour for the lower frequency range (i.e. below the controller knee-point frequency). Replacing the complex frequency s with $j\omega$ yields an impedance given by

$$\begin{aligned} Z_{eq}(\omega) &= R_{mr} + j\omega L_{mr} + K_p - j\frac{K_p}{\omega T_i} \\ &= (R_{mr} + K_p) + j\left(\omega L_{mr} - \frac{1}{\omega\left(\frac{T_i}{K_p}\right)}\right) \end{aligned} \tag{3.15}$$

When selecting regulator parameters K_p and T_i a first order approximation for PWM and sampling delays is often taken into account. Its time constant can be approximated as

$$T_a = 1.5T_{sw} = \frac{1.5}{f_{sw}}$$

where f_{sw} is the PWM switching frequency. Delays of T_{sw} and $0.5T_{sw}$ are due to sampling and PWM respectively. The system pole represented by τ_{mr} is much larger than the one due to delays. The Modulus Optimum Criterion suggests the zero introduced by the PI-regulator can be set to a value which cancels the slow process pole represented by τ_{mr}. The value of K_p can further be chosen to achieve optimal flatness of the closed loop second order response [9]. The resulting PI-regulator settings are given by

$$K_p = \frac{L_{mr}}{2T_a}; \qquad T_i = \tau_{mr} \tag{3.16}$$

3.6 Wind Power Plant Model Aggregation

There are several techniques for aggregation of WPP array collector systems. Different techniques will yield slightly different impedance values. In this thesis a simple method based on power losses is used for aggregating a certain number of radials into one equivalent radial.

Consider a WPP with M radials, each with N_m turbines distributed along its radial.

Each turbine is assumed to inject the same amount of current. The total current contributed from radial m is given by,

$$I_m = \sum_{n_m=1}^{N_m} I_{n_m}, \quad m = 1, 2, ...M \tag{3.17}$$

where I_{n_m} is the current from turbine n along radial m counting from the end of the radial towards the substation. The series impedance of an equivalent cable representing radial m can be obtained.

$$Z_{eq_m} I_m^2 = \sum_{n_m=1}^{N_m} Z_{n_m} \left(\frac{n_m}{N_m} I_m \right)^2$$

$$\Rightarrow \quad Z_{eq_m} = \sum_{n_m=1}^{N_m} \left(\frac{n_m}{N_m} \right)^2 Z_{n_m} \tag{3.18}$$

where Z_{n_m} the impedance of the cable section connecting the turbines n and $(n+1)$ in the m-th radial. The impedance of the M parallel radials can be further reduced into one equivalent radial,

$$Z_{MV} = \left(\frac{N_1}{\sum_{m=1}^{M} N_m} \right)^2 Z_{eq,1} + \left(\frac{N_2}{\sum_{m=1}^{M} N_m} \right)^2 Z_{eq,2} + \cdots + \left(\frac{N_M}{\sum_{m=1}^{M} N_m} \right)^2 Z_{eq,M} \tag{3.19}$$

The shunt capacitances of all medium voltage radials can be added together, based on the assumption of uniform voltage in the collector system.

$$C_{MV} = \sum_{n_1=1}^{N_1} C_{n_1} + \sum_{n_2=1}^{N_2} C_{n_2} + \cdots + \sum_{n_m=1}^{N_m} C_{n_M} \tag{3.20}$$

where C_{n_m} is the cable shunt capacitance of the section located in radial m between turbine n and $(n+1)$ [33].

4 Test Cases and HRMA Implementation

This chapter is dedicated to HRMA of test cases which have been subject to the similar analysis in published papers. The results obtained thus verify the algorithms which have been implemented in MATLAB for this thesis. In addition, some important considerations in implementation as well as relevant contributions from this thesis are highlighted.

4.1 Three Bus Case

A three bus test case with fundamental frequency parameters is shown in Figure 4.1. Reactances and susceptances are scaled in proportion to harmonic order, and resistances are treated as constant in this simplified example. Calculations for both frequency scan and HRMA are carried out using MATLAB. This test case has been subject to the same kind of analysis in several papers [5, 16, 37].

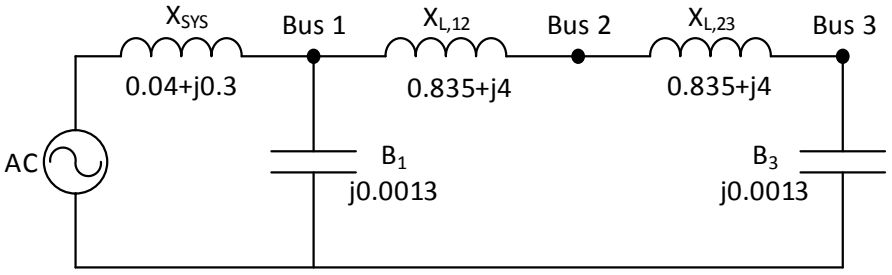

FIGURE 4.1: Three bus case with component data in per unit. Example system used to illustrate frequency scan and modal impedance scan. All parameters values apply at fundamental frequency.

Considering a frequency spectrum from 1 to 60 pu, there are two resonances in this three bus system. Because the system is so simple, resonances can be identified analytically. One parallel resonance is associated to the frequency where X_{B1} is equal in magnitude to $X_{SYS}||(X_{L,12} + X_{L,23})$ (X_{B3} is small and can be ignored). This resonance frequency

is given approximately by

$$f_{res,pu} = \sqrt{\frac{1}{X_{SYS}||(X_{L,12} + X_{L,23}) \cdot B_1}} = \sqrt{\frac{1}{\left(\frac{0.3 \cdot 8}{0.3+8}\right) \cdot 0.0013}} = 51.58\,\text{pu}$$

Another parallel resonance is associated to the frequency where X_{B3} is equal in magnitude to $X_{L,12} + X_{L,23} + X_{SYS}$. ($X_{B1} \ggg X_{SYS}$, X_{B1} can be ignored.) This resonance frequency is given approximately by

$$f_{res,pu} = \sqrt{\frac{1}{(X_{SYS} + X_{L,12} + X_{L,23})B_3}} = \sqrt{\frac{1}{8.3 \cdot 0.0013}} = 9.63\,\text{pu}$$

Frequency Scan

The frequency scan, or nodal impedance frequency response, is equivalent to plotting the diagonal elements of the impedance matrix $[Y]^{-1}$ over the frequency range of interest. The result from such a calculation in the frequency range of 1 to 60 per unit is shown in Figure 4.2. Both resonance frequencies are identifiable from the frequency scan. The resonance near 51.6 pu is most visible at bus 1, the resonance near 9.6 pu is most visible at bus 3, while both resonances can be seen in the driving point impedance at bus 2. The magnitude of driving point impedance at each bus for the two resonance frequencies are listed in Table 4.1.

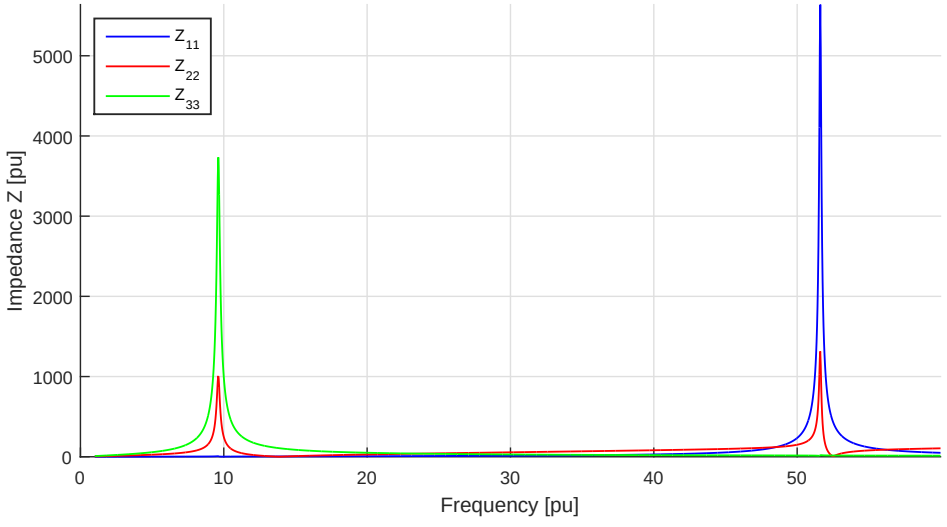

FIGURE 4.2: Frequency scan of three bus system. The two resonance frequencies are detected in the impedance frequency responses.

TABLE 4.1: Driving point impedance magnitudes at resonance frequencies.

Resonance frequency [pu]	51.61	9.62
Z_{11} [pu]	5637	9.48
Z_{22} [pu]	1313	1005
Z_{33} [pu]	17.5	3733

HRMA

The modal impedance frequency responses are shown in Figure 4.3 for the three bus test case. Some papers refers to the modal variables themselves as modes, in which case the modes are defined at every frequency. In other papers the modal impedance resonance peaks are defined as the modes, a definition which is adapted in this thesis. It is common practise to number the modes based on the magnitude of modal impedance at resonance. The modes near 51.61 pu and 9.62 pu are therefore defined as Mode 1 and Mode 2 respectively. The third modal variable has no resonance in the investigated frequency range.

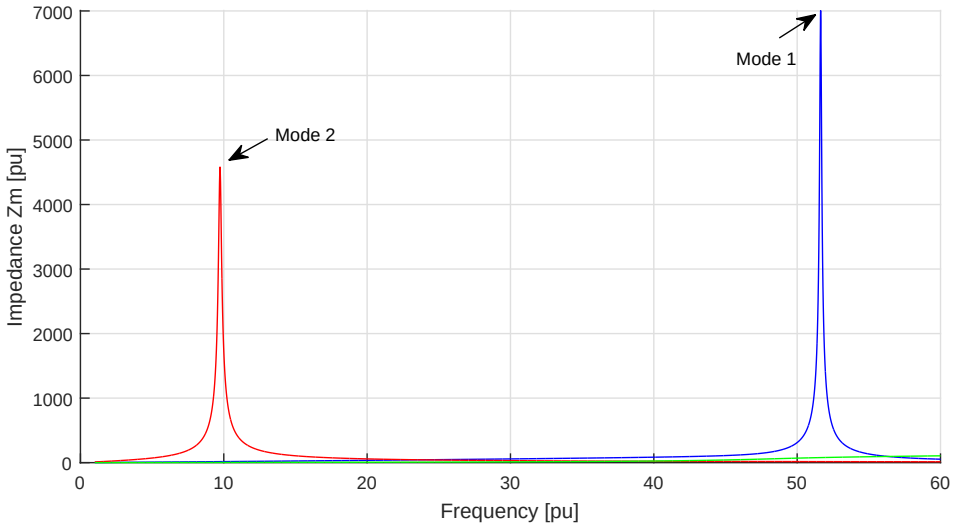

FIGURE 4.3: Modal impedance scan of three bus system. There are two modal resonances, or simply modes, in the investigated frequency range. The modal impedances are defined at all frequencies and have continous frequency responses.

Comparing the nodal impedance frequency scan of Figure 4.1 and the modal impedance frequency scan of Figure 4.3, one can see each nodal resonance is linked to the excitation of a particular resonance mode. Table 4.2 lists the participation factors for the three defined buses in each of the two resonance modes. Bus 1 has the highest participation factor in Mode 1, and bus 3 has the highest participation factor in Mode 2. Based on this result, Xu et al. [5] suggested the participation factors can indicate the center of resonance, i.e. where the resonating branches are connected. However, it will be

shown later that participation factors can be misleading when it comes to locating the resonating branches.

TABLE 4.2: Participation factors calculated at frequencies of the modal resonance peaks.

	Mode 1	Mode 2
Resonance freq. [pu]	51.61	9.62
Modal impedance peak value Z_m [pu]	6951	4743
PF bus 1	0.8103	0.0011
PF bus 2	0.1887	0.2121
PF bus 3	0.0011	0.7868

Previously it was shown how driving point impedance at bus i for any frequency can be expressed as,

$$Z_{ii} = Z_{m,1}PF_{i1} + Z_{m,2}PF_{i2} + Z_{m,3}PF_{i3} + \cdots + Z_{m,n}PF_{in} \qquad (2.25 \text{ revisited})$$

or in terms of weighted participation factors,

$$Z_{ii} = WPF_{i1} + WPF_{i2} + WPF_{i3} + \cdots + WPF_{in} \qquad (2.27 \text{ revisited})$$

In the considered three bus test case, one modal impedance is much larger than the others at the frequencies of the resonance modes. One term on the right hand side of (2.25) is thus much larger than the other terms, i.e. one weighted participation factor is almost equal to the driving point impedance at the resonance frequencies. For example, the weighted participation factor of bus 1 in Mode 1 is given by

$$WPF_{11} = Z_{m,1}PF_{11} = 6951 \cdot 0.8103 = 5632\,\text{pu}$$

It may be confirmed that $WPF_{11} \approx Z_{11}$ by comparing WPF_{11} with the value of Z_{11} listed in Table 4.1. This indicates that the resonance observed from bus 1 is linked to excitation of Mode 1. Similarly the weighted participation factor of bus 3 in Mode 2 is given by

$$WPF_{32} = Z_{m,2}PF_{32} = 4743 \cdot 0.7868 = 3732 \approx Z_{33} \qquad (4.1)$$

It is worth pointing out that the sum of participation factors with respect a mode is equal to one. This can be confirmed by taking the sum of participation factors in each column of Table 4.2. This is due to the fact that eigenvectors calculated with MATLAB's eig()-function always have a 2-norm equal to one (see Appendix B).

A good indicator of how involved a network element is in a resonance mode is how much the resonance frequency changes when parameters of the network element are changed.

This is quantified by the frequency sensitivity index,

$$\left.\frac{\partial f_{res}}{\partial \alpha}\right|_{norm} = \frac{\partial f_{res}}{\frac{\partial \alpha}{\alpha}} = \frac{\partial f_{res}}{\partial \alpha} \cdot \alpha \quad \left[\frac{\text{pu}}{100\,\%}\right] \qquad \text{(2.46 revisited)}$$

Figures 4.4 and 4.5 show for the two resonance modes the frequency and impedance sensitivity index of the network parameters in bar chart and table format. The indices are calculated as outlined in Chapter 2. In the bar diagram the parameters are ranked from left to right in descending order of frequency sensitivity index magnitude. Increasing the value of an inductive reactance or capacitive susceptance will generally reduce associated resonance frequencies, hence the frequency sensitivity index is negative in sign. The sign of the impedance sensitivity index is positive for some parameters and negative for others. Parameters with high magnitude of frequency sensitivity index mostly also have high magnitude of impedance sensitivity index. Sensitivity indices for this three bus case have not been presented in past papers.

For the modal resonance peak at h=51.61 pu frequency, also known as Mode 1, the frequency sensitivity is high for B_1 and X_{SYS}, and low for every other parameter. Similarly for Mode 2, the frequency sensitivity index is high for B_3, $X_{L,12}$ and $X_{L,23}$, and low for other parameters. The frequency sensitivity index hence effectively identifies the network branches most involved in the resonance modes.

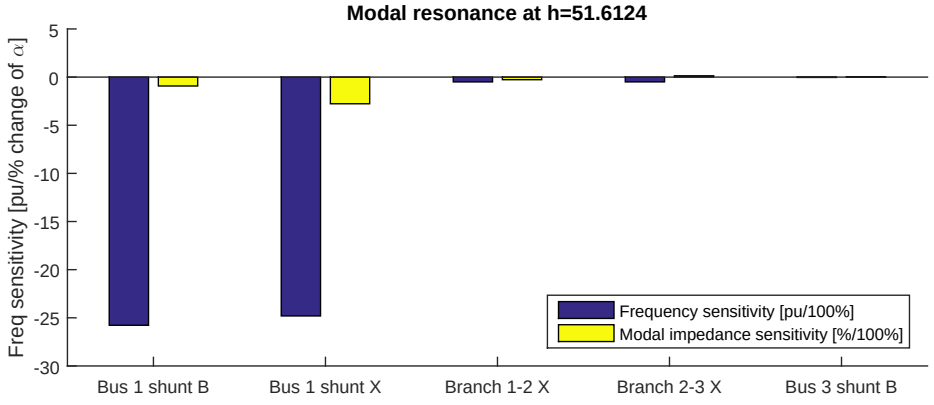

FIGURE 4.4: Frequency sensitivity of resonance mode at h=51.61 pu with respect to capacitive susceptances and inductive reactances of the three bus test system.

Network branch	Freq. sens. [pu/100%]	Impedance sens. [%/100%]
Bus 1 shunt B	-25.7719	-0.9239
Bus 1 shunt X	-24.8060	-2.7704
Branch 1-2 X	-0.5006	-0.2712
Branch 2-3 X	-0.5000	0.1337
Bus 3 shunt B	-0.0361	0.0160

A better understanding of the sensitivity indices can be obtained by considering Figure 4.6, which shows movement of the modal resonance peak near h=9.62 per unit frequency following a 5 % increase and decrease of the shunt connected susceptance at

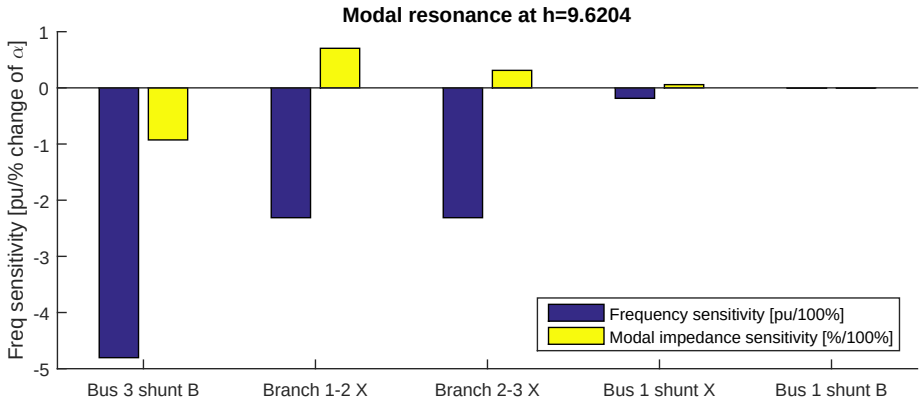

FIGURE 4.5: Frequency sensitivity of resonance mode at h=9.62 pu with respect to capacitive susceptances and inductive reactances of the three bus test system.

Network branch	Freq. sens. [pu/100%]	Impedance sens. [%/100%]
Bus 3 shunt B	-4.8038	-0.9271
Branch 1-2 X	-2.3118	0.7041
Branch 2-3 X	-2.3118	0.3113
Bus 1 shunt X	-0.1866	0.0572
Bus 1 shunt B	-0.0067	0.0003

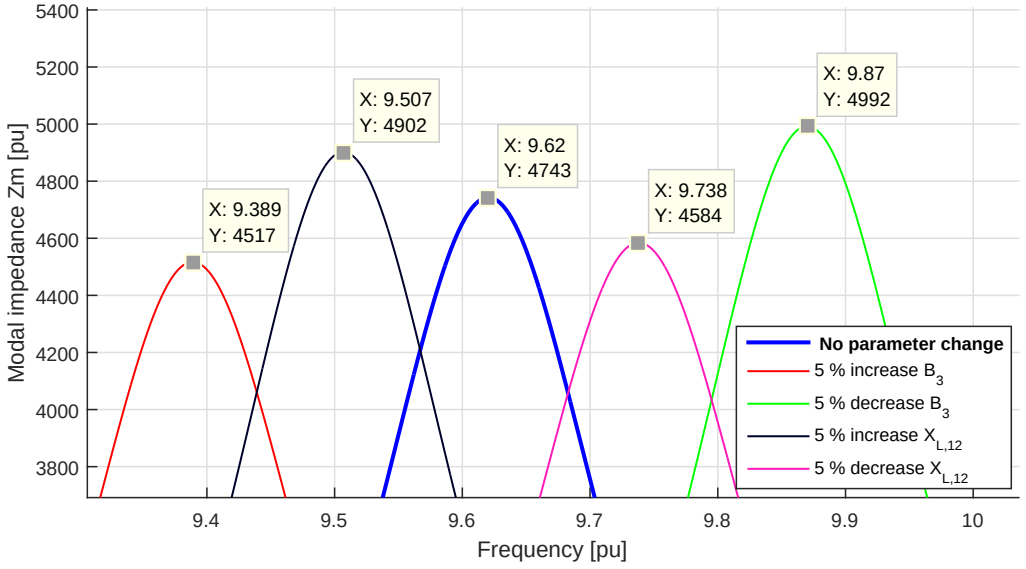

FIGURE 4.6: Movement of resonance mode peak near 9.62 pu following change of B_3 (bus 3 shunt B), and $X_{L,12}$ (branch 1-2 X).

bus 3 and reactance of branch 1-2. The normalised sensitivity indices with respect to these parameters can be estimated based on the coordinates given in Figure 4.6. The modal sensitivity indices are approximately given by,

$$\begin{aligned}\frac{\partial Z_m}{\partial B_3}\Big|_{norm} &= \frac{\partial Z_m}{\partial B_3}\cdot\frac{B_3}{Z_m} \approx \frac{\Delta Z_m}{\Delta B_3}\cdot\frac{B_3}{Z_m} \\ &= \frac{(4517-4992)}{0.1\cdot \cancel{B_3}}\cdot\frac{\cancel{B_3}}{4743} = -1.001\ [\frac{\%}{100\%}]\end{aligned} \tag{4.2}$$

and

$$\begin{aligned}\frac{\partial Z_m}{\partial X_{L,12}}\Big|_{norm} &= \frac{\partial Z_m}{\partial X_{L,12}} \cdot \frac{X_{L,12}}{Z_m} \approx \frac{\Delta Z_m}{\Delta X_{L,12}} \cdot \frac{X_{L,12}}{z_m} \\ &= \frac{(4902 - 4584)}{0.1 \cdot \cancel{R}} \cdot \frac{\cancel{R}}{4743} = 0.6705 \ [\frac{\%}{100\%}] \end{aligned} \tag{4.3}$$

The modal frequency sensitivity indices are approximately

$$\begin{aligned}\frac{\partial f_{res}}{\partial B_3}\Big|_{norm} &= \frac{\partial f_{res}}{\partial B_3} \cdot B_3 \approx \frac{\Delta f_{res}}{\Delta B_3} \cdot B_3 \\ &= \frac{9.389 - 9.870}{0.1 \cdot \cancel{B_3}} \cdot \cancel{B_3} = -4.810 \ [\frac{pu}{100\%}] \end{aligned} \tag{4.4}$$

and

$$\begin{aligned}\frac{\partial f_{res}}{\partial X_{L,12}}\Big|_{norm} &= \frac{\partial f_{res}}{\partial X_{L,12}} \cdot X_{L,12} \approx \frac{\Delta f_{res}}{\Delta X_{L,12}} \cdot X_{L,12} \\ &= \frac{9.507 - 9.738}{0.1 \cdot \cancel{X_{L,12}}} \cdot \cancel{X_{L,12}} = -2.310 \ [\frac{pu}{100\%}] \end{aligned} \tag{4.5}$$

The numerical estimates of frequency sensitivity index shown in (4.4) and (4.5) are very close to the ones obtained in simulation. The numerical estimates of impedance sensitivity index shown in (4.2) and (4.3) are relatively close, but with some deviation compared to simulation results. The discrepancy between numerical estimate and simulation is likely due to the impedance-parameter relationship not being exactly linear. Based on this kind of simple calculation one can see the usefulness of sensitivity indices for predicting movement of the modal resonance peaks in the impedance-frequency plane.

4.2 IEEE 14 Bus Case

The IEEE 14 bus test system is in this section analysed using HRMA. Despite this system representing a power distribution network, not an offshore WPP, it is chosen for analysis because results from HRMA of this system are available in published papers [6, 7]. The details of the IEEE 14 bus test case can be found in [38]. Bus and branch data for the case is included in Appendix A. The frequency range of interest is from fundamental frequency up to 30 pu due to this range being considered in the aforementioned papers.

The following key points are considered in construction of the admittance matrix for frequency scan and HRMA:

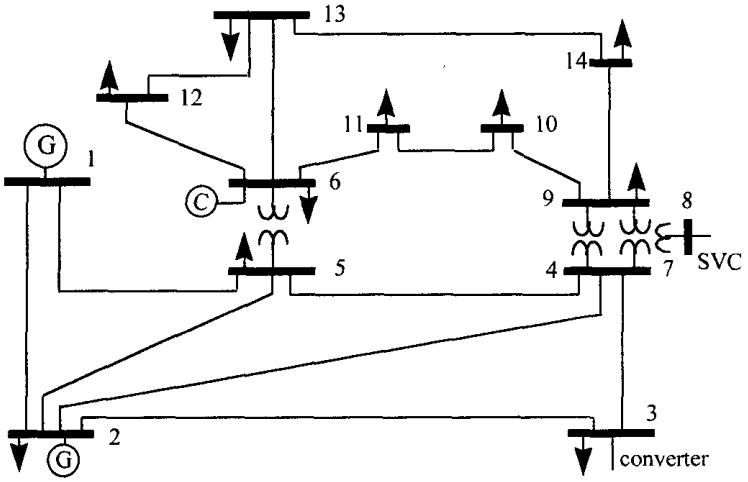

FIGURE 4.7: Single line diagram of IEEE 14 bus system [38]. (G) indicates generator and (C) indicates synchronous condenser.

- The generators at buses 1 and 2 and the synchronous condenser at bus 6 are all modelled by their subtransient reactances, which is equal to 0.25 pu at fundamental frequency.
- Transformers are modelled by their respective short-circuit reactances.
- The loads are modelled using the CIGRE load model, based on the fundamental frequency load flow included in Appendix A.
- All harmonic filters are of the single tuned type [12].
- The harmonic sources, i.e. the twelve-pulse HVDC converter at bus 3 and SVC at bus 8, are assumed to behave like current sources and are thus ignored in construction of the admittance matrix for frequency scan and HRMA.
- Frequency dependency of parameters is ignored.
- The lines which have specified values of charging susceptance are modelled using the long line corrected π-equivalent, with the correction factors calculated at each discrete frequency. Lines without specified values of charging susceptance are modelled using the short-line approximation.

The driving point impedance frequency responses are plotted in Figure 4.8, and the modal impedance scan is shown in Figure 4.9. The decoupling of the resonances achieved by the modal analysis approach is evident. However, unlike for the three bus case, some modal impedances do exhibit more than one local maxima. Hence a modal variable can not be associated to a single resonance mode.

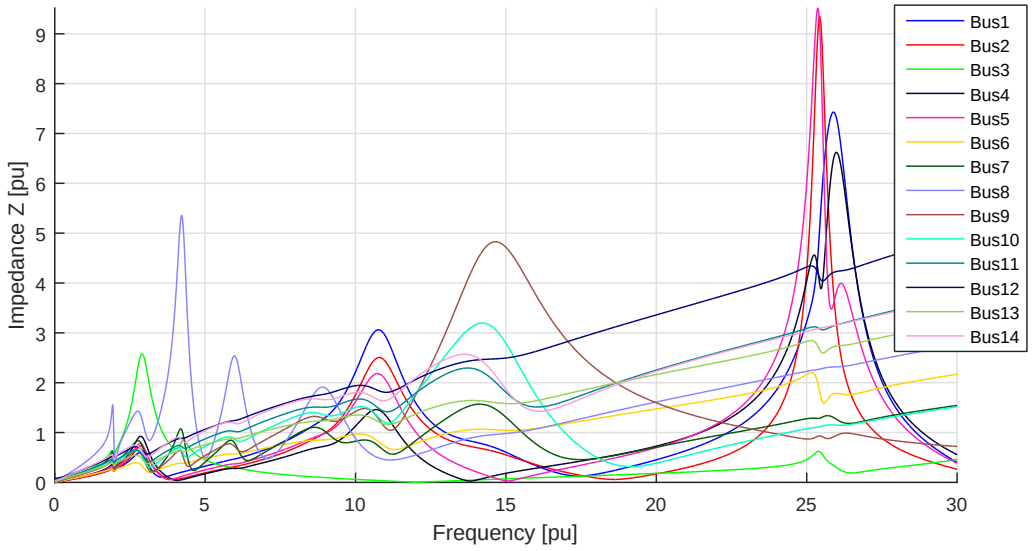

FIGURE 4.8: Frequency scan of all buses in IEEE 14 bus test system.

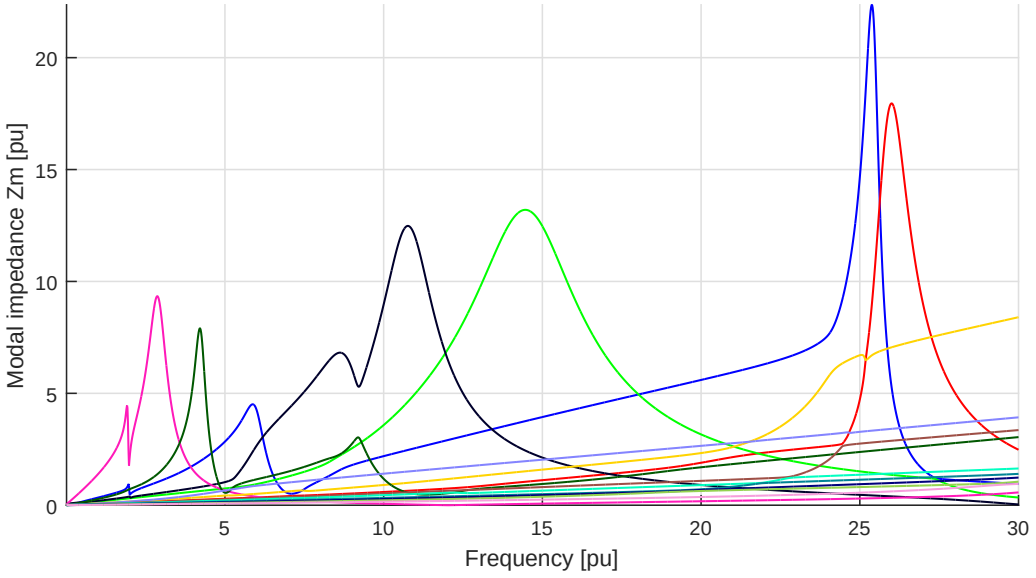

FIGURE 4.9: Modal impedance scan of IEEE 14 bus system. Certain modal variables have several resoance peaks in the investigated freuqency range. The modal scan is similar to the one obtained in papers [6, 7].

The envelope of the modal impedance curves has 9 local maxima in the frequency range up to 30 pu. The participation factors for buses in each if these 9 resonance modes have been calculated and results are included in Appendix A. Table 4.3 sums up the resonance modes in terms of mode frequency and magnitude, the most participating bus and its participation factor.

The weighted participation factor of the most participating bus in each resonance mode

TABLE 4.3: IEEE 14 bus system, magnitude and frequency of envelope local maxima, most participating bus and its participation factor.

Modal resonance freq order h [pu]	Modal impedance magnitude [pu]	Largest PF	Most participating bus #
1.917	4.4553	0.2705	8
2.869	9.3417	0.2632	3
4.212	7.9056	0.6543	8
5.874	4.5109	0.4359	8
8.627	6.8356	0.1376	9
10.738	12.4556	0.2027	1
14.458	13.1867	0.3618	9
25.261	22.5070	0.4138	5
25.943	18.0491	0.3742	1

can be found by multiplying the modal impedance magnitude with the participation factor of that bus, i.e. by multiplying elements in the second and third column in Figure 4.3. Principally the weighted participation factor of the most participating bus approaches the largest driving point impedance at the resonance frequencies. For example, at the resonance mode near 14.458 pu frequency,

$$WPF_{39} = 13.1867 \cdot 0.3618 = 4.868 \approx Z_{99}$$

The actual value of Z_{99} can be observed in Figure 4.8. Similar results can be obtained for the other most participating buses listed in Table 4.3. The driving point impedance resonances can hence predominantly be linked to excitation of individual resonance mode.

FIGURE 4.10: Sensitivity indices of the five most participating branches in modal resonance located at h=4.212 pu frequency.

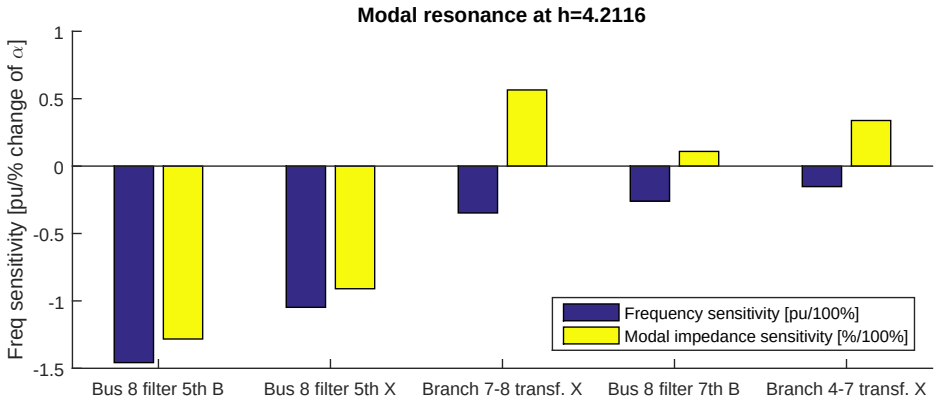

Network branch	Freq. sens. [pu/100%]	Impedance sens. [%/100%]
Bus 8 filter 5th B	-1.4578	-1.2826
Bus 8 filter 5th X	-1.0477	-0.9098
Branch 7-8 transf. X	-0.3477	0.5649
Bus 8 filter 7th B	-0.2598	0.1089
Branch 4-7 transf. X	-0.1522	0.3382

The sensitivity indices can also in this case be used to locate the most participating network branches in resonance modes of interest, and to predict movement of the resonance mode in the frequency-impedance plane following a parameter change. As an example, the sensitivity indices are shown in Figure 4.10 for the five parameters that have the largest frequency sensitivity index with respect to the resonance mode at 4.212 pu frequency. The sensitivity indices show that the 5^{th} harmonic filter located at bus 8 is heavily involved in this resonance mode. In this case the most participating bus is also the location of the network component with highest sensitivity indices.

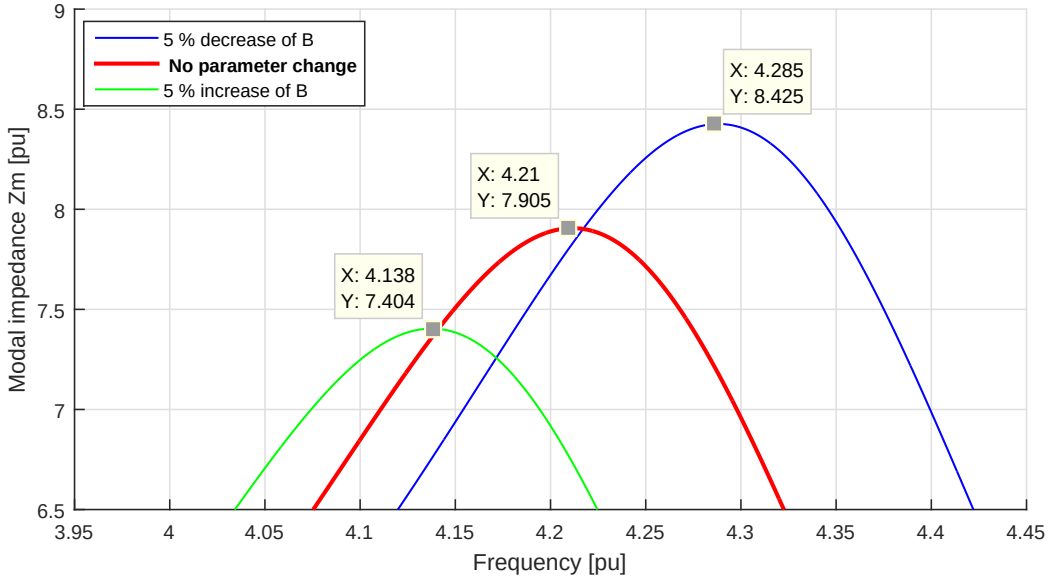

FIGURE 4.11: Movement h=4.212 pu modal resonance with 5 % variation of 5^{th} harmonic filter capacitive susceptance B_1 at bus 8.

Figure 4.11 shows how the resonance mode around harmonic order h=4.212 pu changes with a ±5 % parameter change of capacitive susceptance B_1 of the 5th harmonic filter at bus 8. A 5 % parameter increase reduces the magnitude and frequency of the modal resonance, while a 5 % decrease of the capacitive susceptance has the opposite effect. The coordinates of the modal impedance peaks are marked in the figure, and allows for numerical verification of sensitivity indices. The impedance sensitivity is approximately

$$\begin{aligned}\frac{\partial Z_m}{\partial B}\Big|_{norm} &= \frac{\partial Z_m}{\partial B}\cdot\frac{B}{Z_m} \approx \frac{\Delta Z_m}{\Delta B}\cdot\frac{B}{z_m} \\ &= \frac{(7.404-8.425)}{0.1\cdot \cancel{B}}\cdot\frac{\cancel{B}}{7.905} = -1.292\ [\frac{\%}{100\%}]\end{aligned}$$

and the frequency sensitivity is approximately

$$\begin{aligned}\frac{\partial f_{res}}{\partial B}\Big|_{norm} &= \frac{\partial f_{res}}{\partial B}\cdot B \approx \frac{\Delta f_{res}}{\Delta B}\cdot B \\ &= \frac{4.138-4.285}{0.1\cdot \cancel{B}}\cdot \cancel{B} = -1.470\ [\frac{pu}{100\%}]\end{aligned}$$

Both of these estimates are very close to the values obtained in simulation which are listed in the table of Figure 4.10.

Lines and cables often play a crucial role in harmonic resonances in power system. Hence the importance of accurate line and cable models for harmonic studies must be stressed. Figure 4.12 shows a comparison of the driving point impedance at bus 3 when the lines are modelled using short line models, nominal π-equivalent models and long-line corrected π-equivalent models. The long line effects are prominent from about the 25^{th} harmonic order and above. A similar figure and associated observations can be found in the documentation of this 14 bus test system [38].

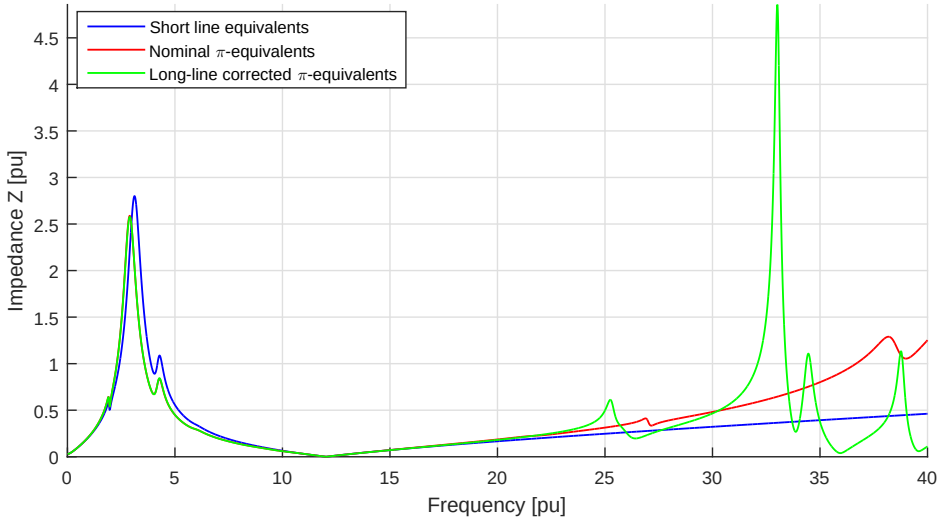

FIGURE 4.12: Frequency scan at bus 3 showing effect of various cable models in frequency range up to 40^{th} harmonic. Long line effects are prominent from about the 25^{th} harmonic order and higher.

The modal impedance scan obtained using nominal π-equivalent line models is shown in Figure 4.13. Comparing with Figure 4.9, the two resonance modes of highest frequency are different. It can be verified that several lines are heavily involved in these resonances. Long line correction factors hence should not be neglected when analysing resonances where lines or cables are heavily involved.

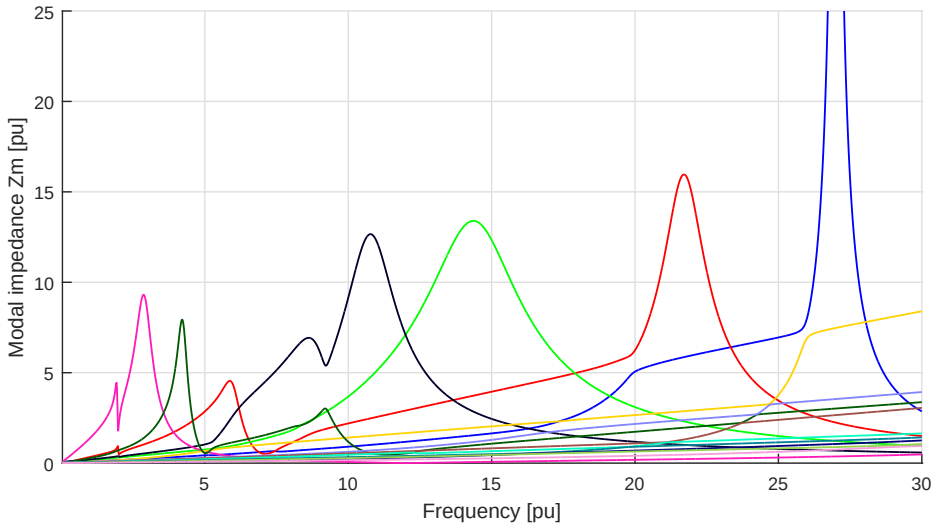

FIGURE 4.13: Modal impedance scan of IEEE 14 bus system using nominal π-equivlaent line models.

4.3 HRMA Implementation

Results obtained from the three and 14 bus test cases are mostly consistent with the what has been presented in past papers. This inspires confidence in the HRMA algorithms implemented in MATLAB. This section is used to highlight some important considerations in implementation of HRMA. In the authors opinion some aspects have not been properly presented in past papers, hence the presentation here is considered a contribution of this thesis.

Modal Switching

Modal impedances plotted against frequency generally appear as smooth, continuous curves, exemplified by Figure 4.3 and Figure 4.9. An issue encountered when implementing the algorithms for HRMA is that the standard MATLAB eig()-function, which returns the eigenvectors and eigenvalues of a matrix, does not sort the eigenvalues and eigenvectors in a predictable way. As an example consider the Y-bus matrix of a three bus system. The eigenvalues and eigenvectors at discrete frequency f are returned by the eig()-function respectively in the diagonal $[\Lambda_f]$-matrix, and as columns of $[L_f]$,

$$[\Lambda_f] = \begin{bmatrix} \lambda_{1,f} & 0 & 0 \\ 0 & \lambda_{2,f} & 0 \\ 0 & 0 & \lambda_{3,f} \end{bmatrix}, \quad [L_f] = \left[\begin{array}{c|c|c} \vdots & \vdots & \vdots \\ l_{1,f} & l_{2,f} & l_{3,f} \\ \vdots & \vdots & \vdots \end{array}\right] \tag{4.6}$$

where for example $l_{1,f}$ is the eigenvector of $\lambda_{1,f}$, the inverse of which is the modal impedance $Z_{m,1}$. At the next discrete frequency, separated from f by a small step Δf, there will be minor changes in eigenvalues and eigenvectors. However, the random nature in which the eigenvalues are returned by the eig()-function might result in a new order of the eigenvalues, for example,

$$[\Lambda_{f+\Delta f}] = \begin{bmatrix} \lambda_{2,f+\Delta f} & 0 & 0 \\ 0 & \lambda_{3,f+\Delta f} & 0 \\ 0 & 0 & \lambda_{1,f+\Delta f} \end{bmatrix}, \quad [L_{f+\Delta f}] = \left[\begin{array}{c|c|c} \vdots & \vdots & \vdots \\ l_{2,f+\Delta f} & l_{3,f+\Delta f} & l_{1,f+\Delta f} \\ \vdots & \vdots & \vdots \end{array}\right] \tag{4.7}$$

In other words the eigenvalue associated to a particular modal impedance can be returned from the eig()-function at a seemingly random position in the diagonal Λ-matrix. Modal switching refers to such swapping of places in the eigenvalue and eigenvector matrices while obtaining the frequency response. If no countermeasures are taken, the resulting modal impedance scan might look like the one in Figure 4.14. Such plots are presented in several papers on the topic of HRMA [21, 24, 25].

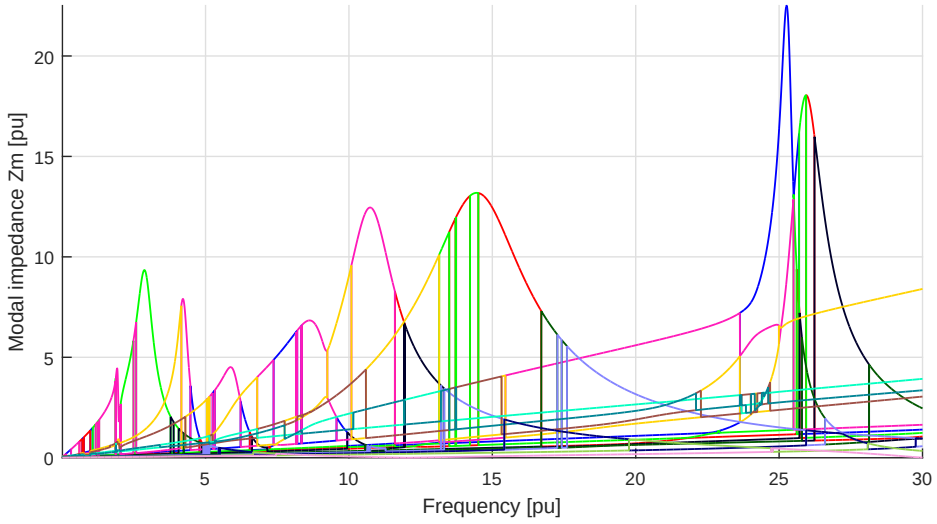

FIGURE 4.14: Modal switching observed when analysing the 14-bus test system without countermeasures. The eigenvalues swap places in the diagonal eigenvalue matrix Λ as the frequency is sweept.

There are several ways to deal with the issue of modal switching. A straightforward way to approach the problem is to use a combination of the eig()-function and a correlation technique to reorder the eigenvalues and eigenvectors whenever a switch occurs. Correlation technique is one of three methods covered in a paper by Zlatunić et al. [39]. From basic matrix algebra it is known that eigenvectors associated with distinct eigenvalues are orthogonal to each other, i.e. they have a vector-product equal to zero. Moreover, eigenvectors returned by the eig()-function are normalised so that the 2-norm of each

eigenvector is equal to one. Hence multiplying an eigenvector with itself gives a product of one, and multiplying eigenvectors associated with different eigenvalues gives a product of zero. The correlation technique can be summarized as follows:

- Obtain the eigenvector-matrix $L_{f-\Delta f}$ for the previous discrete frequency and eigenvector-matrix L_f for the current frequency which is increased by Δf from the previous step.
- Obtain the matrix product of the transpose eigenvector-matrix from current step with the eigenvector matrix from previous step, $L_f^T \cdot L_{f-\Delta f}$.
- In each column of the aforementioned matrix-product, one element will be close to unity, while the other elements will be close to zero. The row and column number of the unity-elements define the column numbers of associated eigenvectors at the current and previous frequency respectively.
- Sort the eigenvectors and eigenvalues at the current frequency according to the order of the previous frequency.

With this correlation technique, the result at the initial frequency defines the order of the eigenvalues and eigenvectors. Mode switching is inevitable, but is tracked and corrected as one moves from one frequency to the next. Because eigenvalues and eigenvectors change a little as on moves from one discrete frequency to the next, a relatively small step between discrete frequencies is required for the method to work reliably. In the authors experience with the test cases, discrete steps of 0.01 pu frequency and smaller gives reliable correction of modal switching.

An entirely different approach is to ignore the issue of modal switching and only consider the envelope of the modal impedance curves. At a modal resonance frequency, one eigenvalue is usually much smaller than the others, hence there is only one large modal impedance, and this impedance is visible in the envelope of modal impedance scan. However, if several resonances appear at frequencies close to each other, resonance peaks may not appear in the envelope. The modal envelope approach is referred to as critcal mode scan by Xu et al. [5].

Complex vs. Real Number Admittance Matrix

An admittance matrix is usually formulated as a matrix of complex numbers, but can however also be formulated as a matrix of real numbers. By splitting the real and

imaginary parts of phasors, the real number Y-matrix for a 2-node network is obtained.

$$\begin{bmatrix} V_{1x} \\ V_{2x} \\ V_{1y} \\ V_{2y} \end{bmatrix} = \begin{bmatrix} G_{11} & G_{12} & -B_{11} & -B_{12} \\ G_{21} & G_{22} & -B_{21} & -B_{22} \\ B_{11} & B_{12} & G_{11} & G_{12} \\ B_{11} & B_{12} & G_{21} & G_{22} \end{bmatrix}^{-1} \begin{bmatrix} I_{1x} \\ I_{2x} \\ I_{1y} \\ I_{2y} \end{bmatrix} \tag{4.8}$$

where subscripts x and y denote the real and imaginary parts of complex phasors. The real number Y-matrix has twice the rank and therefore twice the number of eigenvalues with respect to the complex number Y-matrix. It may be verified that half of the eigenvalues of the real Y-matrix are identical to those of the complex Y-matrix, and the other half are complex conjugate of the first half. Consequently, both the real and complex admittance matrices are suitable for HRMA and will yield the same results [5–7, 20].

From (4.8) one can see that the conversion from one form to the other is rather straightforward. Some power analysis software use the real Y-matrix formulation, hence one can envision a real matrix approach to be preferable [5]. An argument can also be made in favour of the real matrix representation due to the eigendecomposition being more efficient for real matrices [20]. However, the complex matrix has been used in this thesis as it allows for avoiding the complex conjugate set of eigenvalues. In addition, the author perceives the implementation of HRMA sensitivity indices as easier when using complex matrix formulation.

Real Y-matrix Envelope Using Power Method

If only the modal impedance envelope is of interest, the power method can be used. This method calculates only the smallest eigenvalue, and is less computer intensive than algortims which calculate every eigenvalue. Xu et al. [5] suggested using the power method for calculation of the modal envelope, and found the real admittance matrix to be preferable. They also found some discrepancy in critical mode scan envelope obtained with the two different matrix formulations [20].

Calculation of the modal envelope using the real Y-bus matrix and the power method was carried out to investigate if there really is a difference in the envelope obtained with the two different Y-bus matrix formulations. Figure 4.15 shows the modal envelope of the 14 bus test system calculated using the real Y-matrix. The critical eigenvalue was calculated using the power method algorithm, and the number of iterations required for an accuracy of 0.005 is shown on the right y-axis. The power method is known to require a high number of iterations when two eigenvalues are of equal magnitude. The

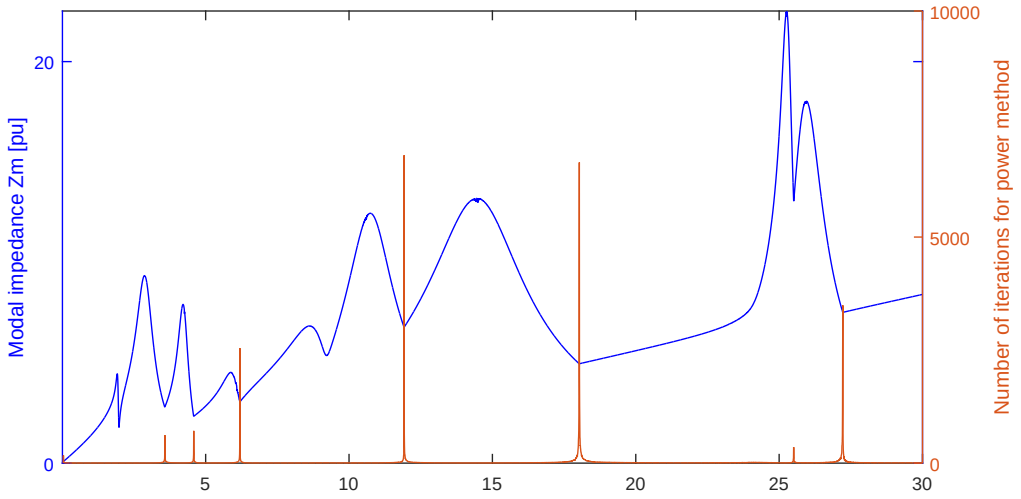

FIGURE 4.15: Modal impedance envelope and number of iterations using real admittance matrix formulation and power method with accuracy of 0.005. Good agreement with complex admittance formulation is obtained. Notice the high number of iterations required when two eigenvalues are of similar magnitude.

agreement with the envelope of modal impedance scan of Figure 4.9 is excellent, with none of the discrepancy seen in aforementioned papers. Hence the discrepancy which was identified in past papers can most likely be attributed to a poor implementation of the power method.

Sensitivity Indices and Non-RLC Branch Network Elements

The information provided by the participation factors as well as modal impedance sensitivity index and frequency sensitivity index was demonstrated for the test cases of this chapter. Among these, participation factors are by far the least burdensome to calculate in terms of computational effort required. Impedance and frequency sensitivity indices require far more computational time and/or power. They rely on numerical calculation of several terms, and experience with the presented test cases suggest discrete steps of frequency as low as 1×10^{-4} pu are required for decent accuracy.

Calculation of sensitivity indices require the explicit calculation of terms such as $\partial G_{br}/\partial\alpha\partial h$, where α can be the fundamental frequency parameter R_1, X_1 or B_1. In order to obtain a general algoritm it was assumed that all relevant network branches of interest are fully representable by an RLC-branch. This is not the case for cables or lines when long line correction factors are taken into account. The hyperbolic correction factors of the long line corrected model makes it difficult to derive straightforward expressions for sensitivity indices. Hence it is arguably easier to simply calculate the sensitivity indices numerically. This can be done by recalculating the modal impedance resonance

magnitude and frequency when α is subject to a small change of value, i.e. $\pm\Delta\alpha$. Such an approach is taken in this thesis whenever long line corrected models are used.

5 Offshore WPP Resonance Analysis

In this chapter HRMA is applied for resonance analysis of a WPP model based on the real 400 MW Anholt offshore WPP.

HRMA has in the past been applied to offshore WPPs [22, 24]. In those papers a number of simplifying assumptions are used in modelling of the WPPs, such as uniform and heavily aggregated radials in the array collector system. Moreover they constrain analysis to below the 25^{th} harmonic frequency, a choice likely motivated by the limitations of the nominal π-equivalent cable models. Modal switching is not corrected, resulting in some confusion in terminology and results. Further investigation of the capabilities of the HRMA method when it comes to resonance analysis of offshore WPPs is therefore warranted.

The sensitivity of HRMA results with respect to the following aspects and simplifications in modelling of the WPP will be investigated:

- WPP radial collector system aggregation
- Type of cable models, nominal or long-line corrected π-equivalents
- Uniform collector radials
- Frequency dependent resistance/skin effect
- WTG modelling, emission filters and converter current controller

5.1 Anholt Offshore WPP Layout

The 400 MW Anholt offshore WPP is comprised of 111 turbines, each rated at 3.6 MW and equipped with a full-scale frequency converter. An overview of the WPP layout and export system is shown in Figure 5.1. As indicated in the figure, there are three 140 MVA transformers located at the offshore substation, and the points of common coupling (PCC) are defined on the 33 kV side of these transformers. Downstream of the

PCCs are the collector array cables and wind turbines. This part of the system was installed and is operated DONG Energy Wind Power. The Danish TSO, Energinet.dk, is responsible for the part of the system which is upstream of the PCC, i.e. the export system.

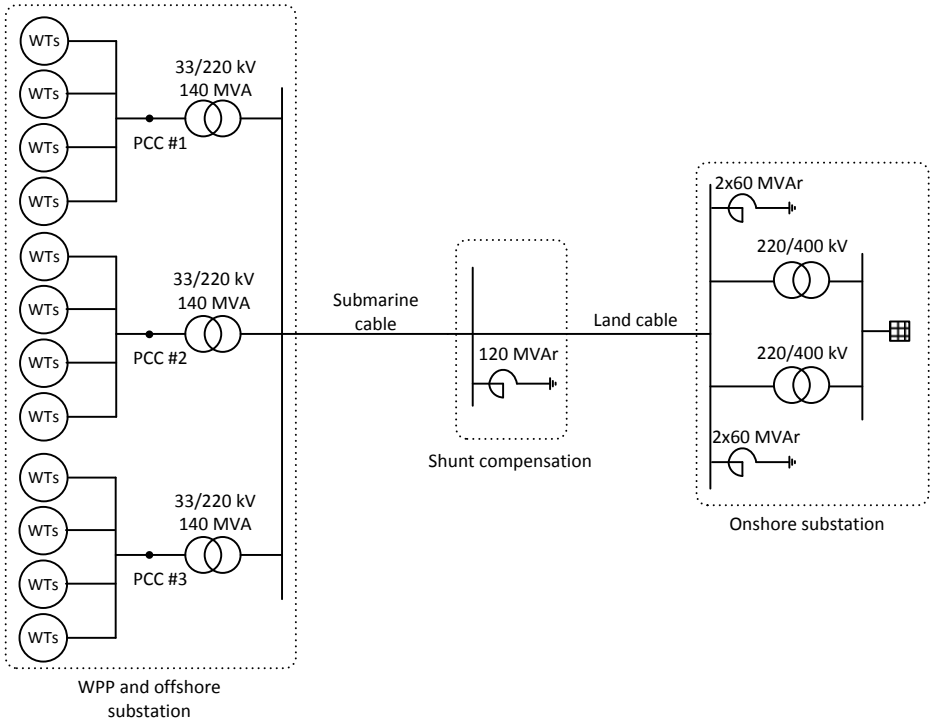

Connected to	WTGs	Arrays	Total array cable length	Total capacitance of array cables
PCC #1	37	4	50km	14uF
PCC #2	37	4	48km	13uF
PCC #3	37	4	54km	15uF

FIGURE 5.1: Single line diagram of Anholt WPP and export system. Table shows key data about radial arrays downstream of each point of common coupling [32].

Each 140 MVA transformer connects 37 WTGs across 4 radials to the 220 kV export system. Hence there are in total 12 radials, each one collecting the power from either 9 or 10 turbines. An overview of the array collector system is given in Appendix C. The array layout is non-uniform, and each radial uses a combination of 150 mm^2, 240 mm^2 and 500 mm^2 copper cables. There is also a difference in total length and capacitance of the array cables connected to each PCC, as indicated in the table of Figure 5.1.

The high voltage (220 kV) export system includes one 24.5 km aluminium 3x1600 mm^2 submarine cable, and one 58 km aluminium 3x2000 mm^2 underground cable. There is

reactive compensation of 120 MVAr placed in between the cables. The onshore substation includes 2x450 MVA transformers connecting the underground cables to the central grid, as well as another 4x60 MVAr of reactive compensation.

Beyond the aforementioned data, little is public knowledge when it comes to parameter values of the Anholt WPP. Hence it is not an objective to achieve a model with the exact parameter values of the real system. Cable data is estimated based on ABB's user's guide for submarine and land cable systems [40, 41], and transformer data is estimated roughly based on rule of thumb.

Wind Power Plant Models

Three different WPP models with varying degree of aggregation are implemented for HRMA. All models are based on the simplifying assumption that the four radials connected to each PCC are symmetrical. Those four radials are further reduced into one equivalent radial using the aggregation technique of Section 3.6. Assuming there are 9 turbines in each radial, this aggregation results in a WPP model with 27 turbine equivalents and 33 buses as shown in Figure 5.2. The total length and capacitance of radials connected to each PCC is given in Figure 5.1. In obtaining the 33 bus model the total length of the four aggregated radials at each PCC is set equal to the listed value. Cross-section and share of total length for each cable section is selected to achieve good fitting with the listed capacitance values.

The 33 bus WPP model has a relatively high number of buses and branches, and this might make it unnecessarily complicated for getting an overview of resonances in the system. Two models with higher degree of radial collector cable aggregation are therefore also defined. Those models are further reductions of the 33 bus model obtained using the aggregation technique of Section 3.6. A 15 bus model, shown in Figure 5.3, represents all collector cable sections with the same cross-section as a single cable and with 3 equivalent WTGs per radial. The 9 bus model, shown in Figure 5.4, represents each radial with one cable and one WTG equivalent.

Wind turbines, including main reactors, shunt harmonic filter and transformers, are initially modelled as harmonic current source, hence these components do not appear in the Y-bus matrix. It can also be regarded as a situation where all turbines are disconnected and WTG main circuits are de-energised, i.e. transformers, shunt harmonic filters and main reactors are disconnected.

The modal envelope and participation factors can be obtained for the most comprehensive model without much computational burden. However, calculation of the modal

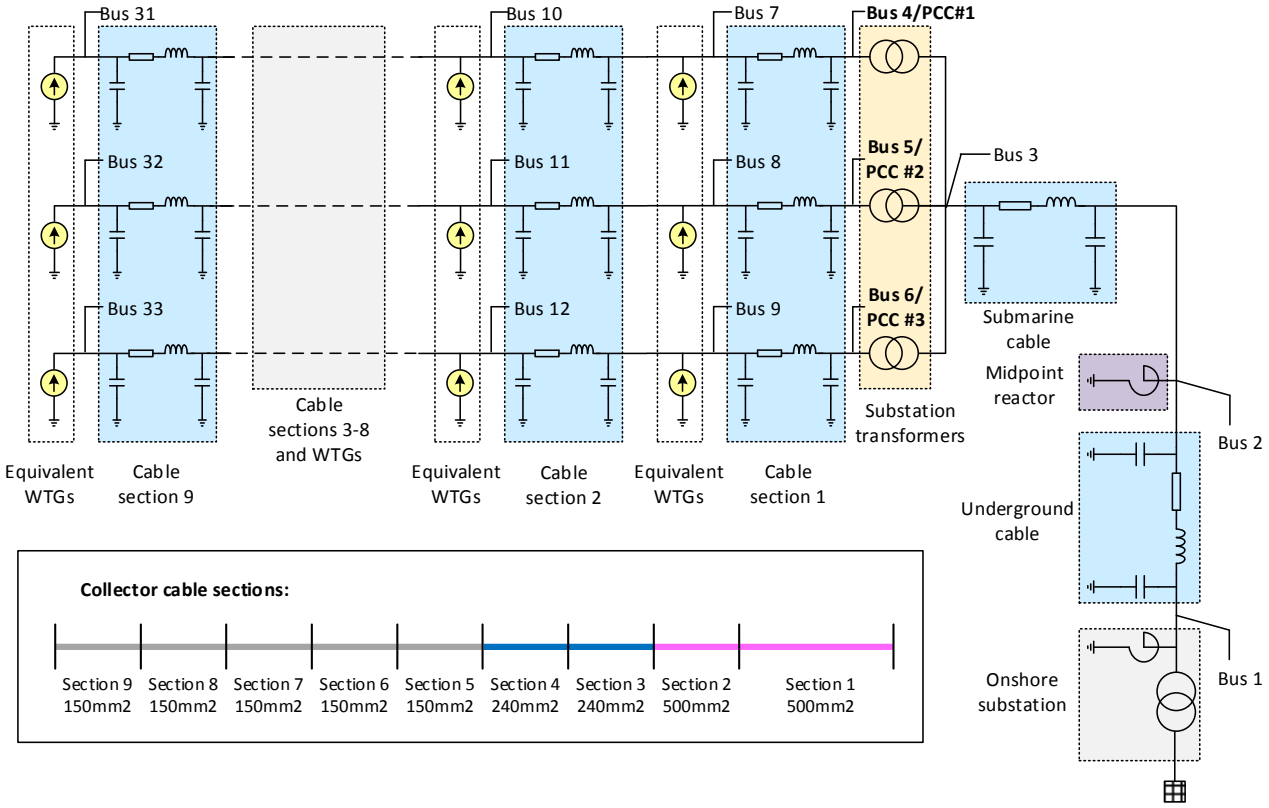

FIGURE 5.2: Single line diagram of Anholt offshore WPP model with simplified array representation. 33 buses are defined as given in the figure.

sensitivity indices becomes burdensome with the large 33 bus model. It is generally observed that the most critical resonances appear in the simplified 9 and 15 bus models. Figure 5.5 shows a comparison of the modal impedance envelope obtained with the three WPP models with long line corrected cables and skin effect included. Because, the main resonances are reflected in all three models, the 9 bus model is used to gain further insight about these resonances.

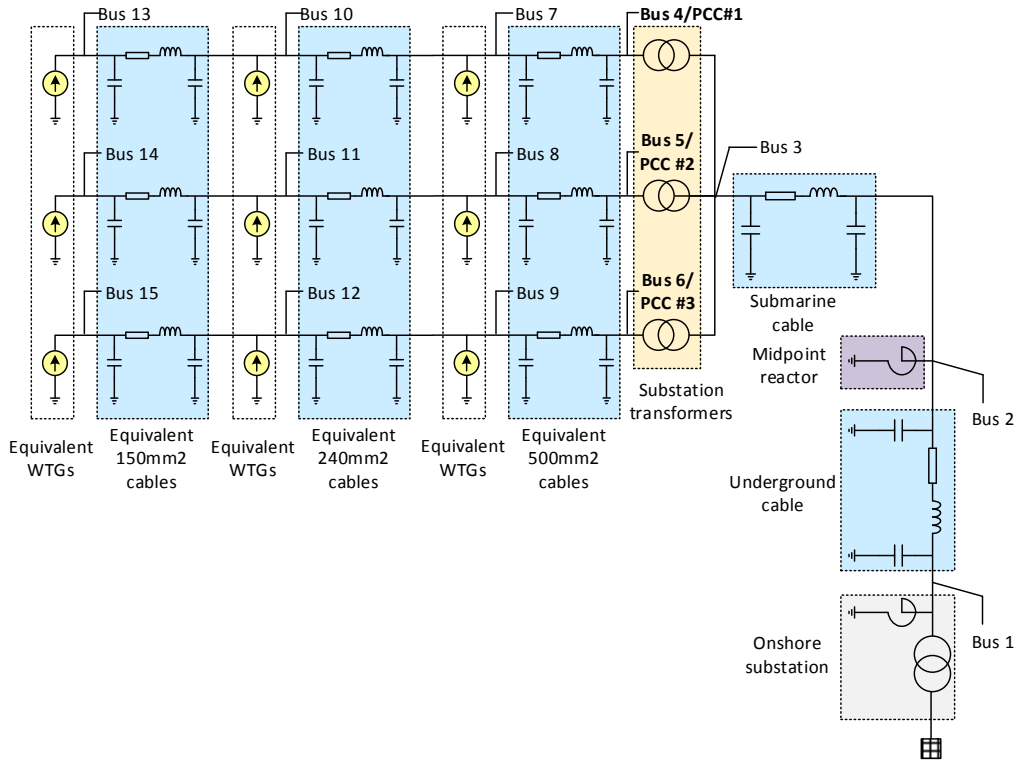

FIGURE 5.3: Single line diagram of Anholt offshore WPP model with simplified array representation. 15 buses are defined as given in the figure.

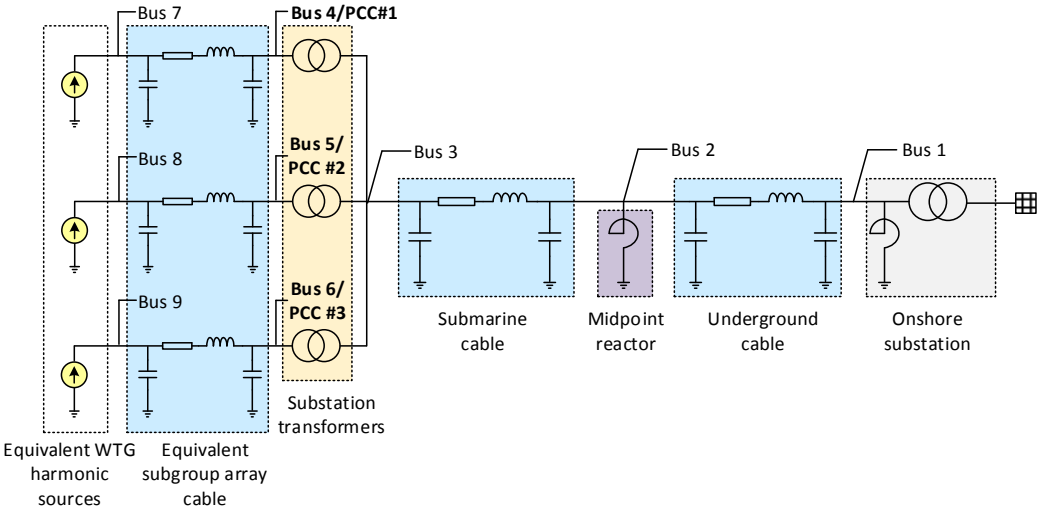

FIGURE 5.4: Single line diagram of Anholt offshore WPP model with simplified array representation. 9 buses are defined as given in the figure.

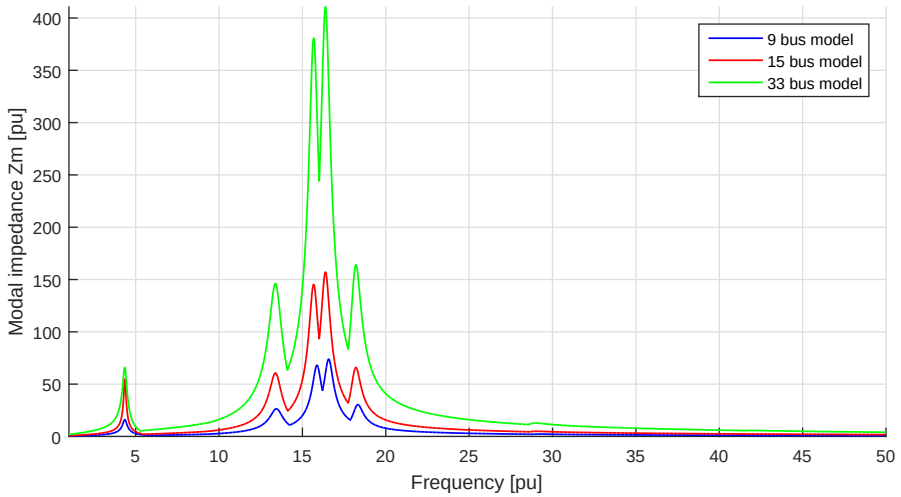

FIGURE 5.5: Modal envelope of 9, 15 and 33 bus models with skin effect included. The same resonances are visible in the evelope of all WPP models. The 9 bus model is therefore considered adequate for investigating these resonances.

5.2 9 Bus Model HRMA

Nominal π-equivalent cable models

HRMA is now carried out for the 9 bus WPP model constructed with nominal π-cable models. The simple structure of this WPP model yields predictable results and allows for calculation of modal sensitivity indices as outlined in Chapter 2. The modal impedance frequency response is shown in Figure 5.6. There are six resonance modes in the investigated frequency range, with no modal variable involved in more than one resonance mode. Bus participation factors associated to the resonance modes are shown in Table 5.1.

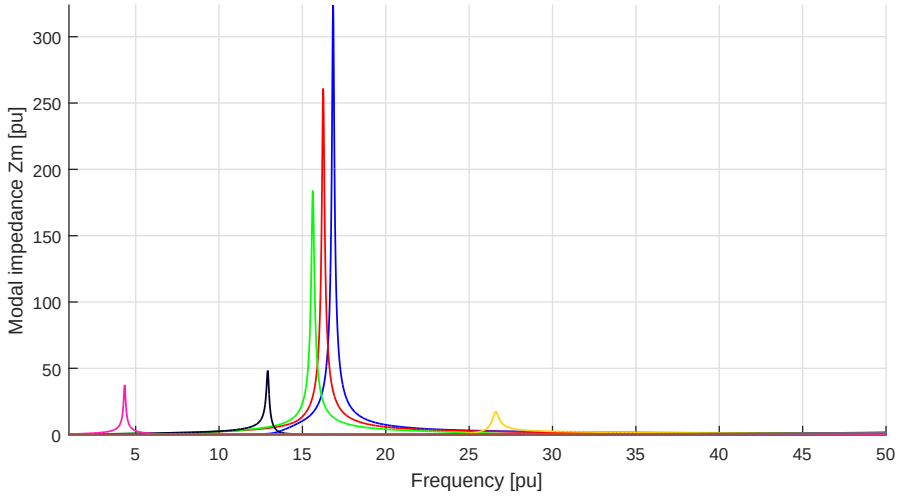

FIGURE 5.6: Modal impedance scan of 9 bus WPP model with nominal cable models. Modes are numbered in descending order of modal impedance at their respective resonance frequencies.

TABLE 5.1: Participation factors in resonance modes of 9 bus WPP model with nominal cable models. The largest participation factor in each resonance mode is underlined.

f_{res} [pu]	4.340	12.920	15.623	16.246	16.841	26.597
Z_m [pu]	37.320	48.229	183.986	260.900	323.853	17.150
Bus 1	0.0256	0.1023	0.0024	0.0005	0.0001	0.0003
Bus 2	0.0977	0.0013	0.0033	0.0011	0.0003	0.0151
Bus 3	0.1104	0.0199	0.0002	0.0002	0.0001	<u>0.2879</u>
Bus 4	0.1263	0.1255	0.0153	0.3499	0.0488	0.0670
Bus 5	0.1252	0.1041	0.0061	0.0263	0.3744	0.0909
Bus 6	0.1277	0.1670	0.3976	0.0489	0.0058	0.0450
Bus 7	0.1289	0.1506	0.0201	<u>0.4697</u>	0.0671	0.1640
Bus 8	0.1275	0.1223	0.0077	0.0340	<u>0.4947</u>	0.1957
Bus 9	<u>0.1307</u>	<u>0.2070</u>	<u>0.5474</u>	0.0693	0.0085	0.1342

The participation factors indicate at which buses the resonance modes are most observable in the driving point impedance. For example, the resonance mode near the 16.841 pu frequency is most observable at bus 5 and 8. Similarly, the resonance mode near 16.25 pu is most observable at bus 4 and bus 7, and the the resonance mode near 15.62 pu is most observable at bus 6 and bus 9. The modal sensitivity indices of the five parameters with highest frequency sensitivity with respect to these three resonance modes are shown in Figure 5.7, Figure 5.8, and Figure 5.9 respectively. Frequency sensitivity indices reveal that these resonance are due to the collector cables resonating with the offshore substation transformers. For example, the modal resonance frequency near 16.84 pu is most sensitive to shunt capacitance of cable section 5-8 and reactance of transformer 3-5.

In addition to the three resonance modes due to offshore transformers and collector cables, there is one resonance mode at 4.34 pu, another at 12.92 pu and a third at 26.60 pu frequency. The resonance mode at 4.357 pu frequency stands out due every bus except for bus 1 having a participation factor of comparable magnitude. This indicates that, with the exception of bus 1, observability of this mode is similar in the driving point impedance at all buses. The driving point impedance at every bus near this frequency is shown in Figure 5.10, and the impedance magnitudes are clearly proportional to the bus participation factors.

The sensitivity indices of the five parameters with highest frequency sensitivity with respect to the 4.34 pu resonance mode are shown in Figure 5.11. They reveal this mode is due to interaction between the grid reactance (i.e. onshore substation transformer), underground and submarine export cables. Notice the participation factors for this resonance mode are smallest close to where the resonating branches are connected. This illustrates the important distinction between observability, which is quantified by participation factors, and branch involvement in the resonance mode, which is quantified by the frequency sensitivity index.

Similar analysis can be carried out for the other resonance modes. It can be verified that the resonance mode at 12.92 pu is due to the underground export cable resonating with the onshore substation transformer. The resonance mode at 26.60 pu frequency is due to interaction between the shunt capacitance and series reactance of the submarine export cable. Sensitivity indices for these resonance modes are included in Appendix C.

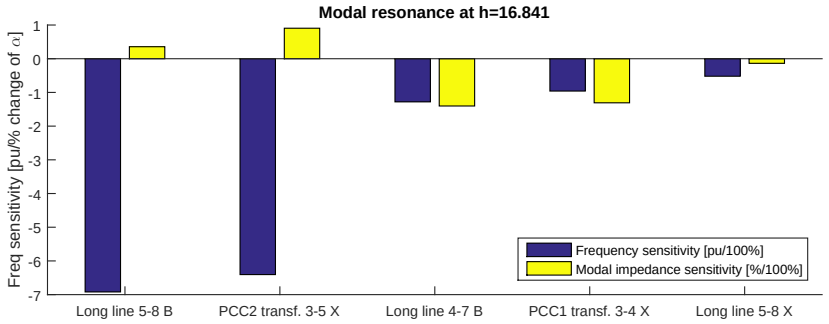

FIGURE 5.7: Sensitivty indices of the five parameters with highest frequency sensitivty index with respect to the modal resoance at 16.84 pu frequency. The collector cable of section 5-8 and the transformer of section 3-5 are the network components most involved in the resonance.

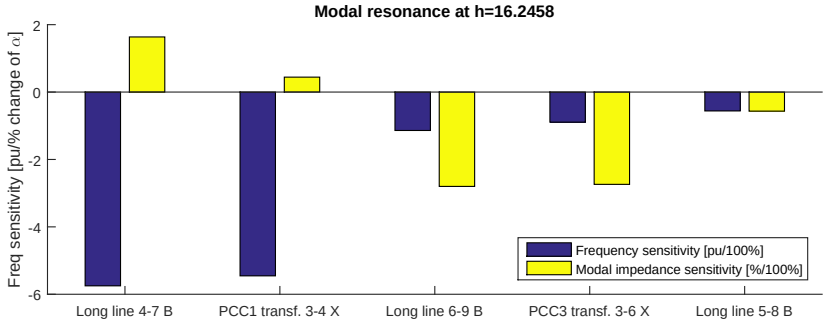

FIGURE 5.8: Sensitivty indices of the five parameters with highest frequency sensitivty index with respect to the modal resoance at 16.25 pu frequency. The collector cable of section 4-7 and the transformer of section 3-4 are the network components most involved in the resonance.

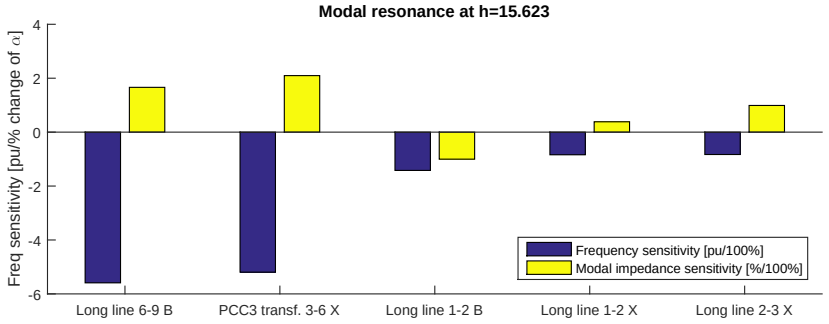

FIGURE 5.9: Sensitivty indices of the five parameters with highest frequency sensitivty index with respect to the modal resoance at 15.62 pu frequency. The collector cable of section 6-9 and the transformer of section 3-6 are the network components most involved in the resonance.

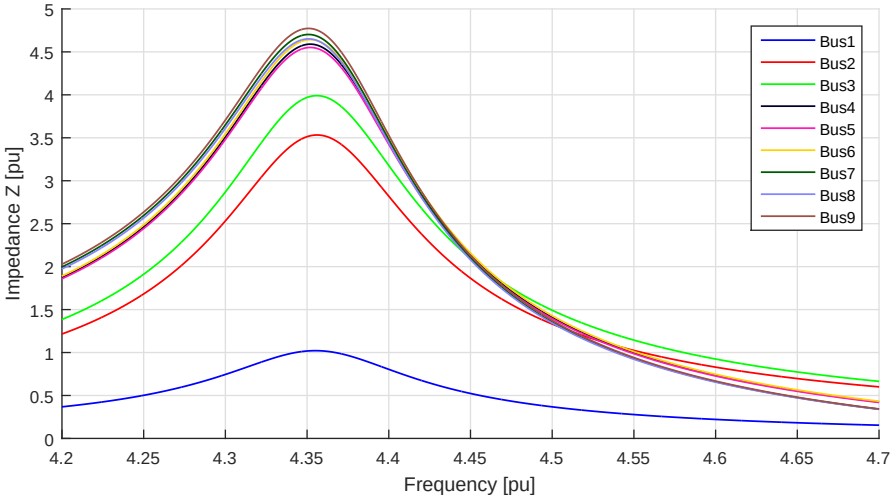

FIGURE 5.10: Driving point impedance around 4.36 pu resonance frequency for every defined bus. The driving point impedance amplitudes are roughly proprtional to the participation factors in the resonance mode, listed in the first column of Table 5.1.

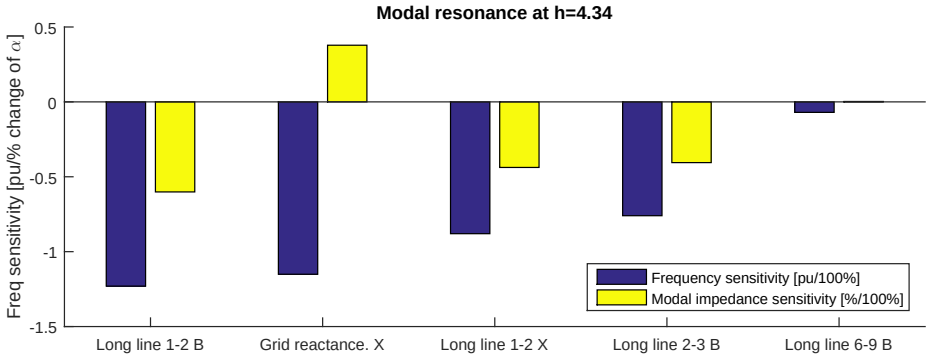

FIGURE 5.11: Sensitivty indices of the five parameters with highest frequency sensitivty index with respect to the modal resoance at4.36 pu frequency. The export cables resonate with the reactance of the onshore substation transformers.

Radial symmetry

The driving point impedances obtained at buses 7, 8 and 9 are shown in Figure 5.12 in the vicinity of the cable-offshore transformer resonance modes. At each of the three buses, one mode clearly dominates the impedance response.

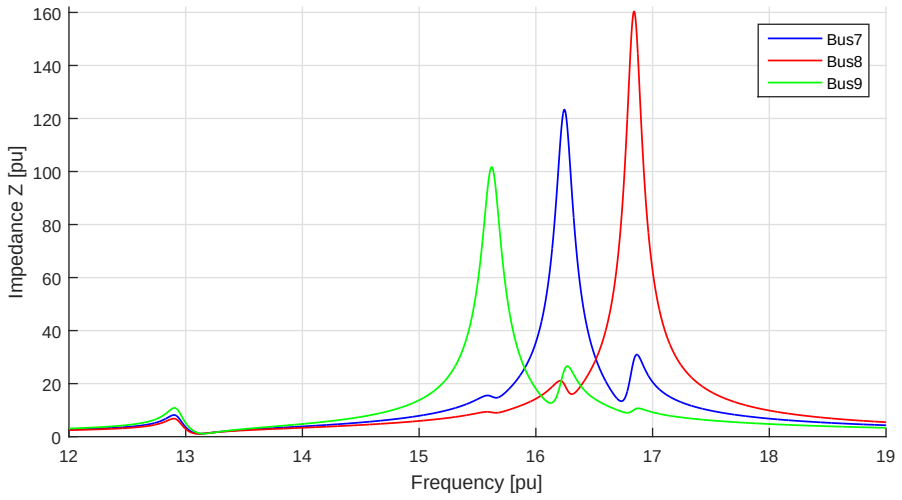

FIGURE 5.12: Driving point impedance obtained at end of collector radials 9 bus WPP model with asymmetric radials and nominal cable modes.

Let's now investigate what happens to the three resonance modes in the 15 pu to 17 pu frequency range when the three radials of the WPP modal are made symmetrical. The driving point impedance and modal impedance frequency responses are shown in Figure 5.13 respectively on the left and right hand side. The driving point impedance frequency response at buses 7, 8 and 9 become identical. Two of the modal variables now have the same frequency response, resulting in two resonance modes in the same location near 16.44 pu frequency. The third modal variable has a different frequency response, with a resonance mode near the 15.93 pu frequency.

Care must be taken in HRMA when two modal variables have identical frequency responses, as is the case for two modal variables in Figure 5.13. Two of the resonance modes are seemingly identical, but the participation of corresponding buses in different radials, for example buses 7, 8 and 9, are different. as given in Table 5.2. Bus 9 participates most in Mode 2, bus 8 participates most in Mode 1, while bus 7 participates equally in both resonance modes. Notice the sum of participation factors in Mode 1 and Mode 2 for each bus is equal, hence the driving point impedance at each bus is also equal. Because two modes are identical, analysing only the modal impedance envelope would obviously be insufficient in this case.

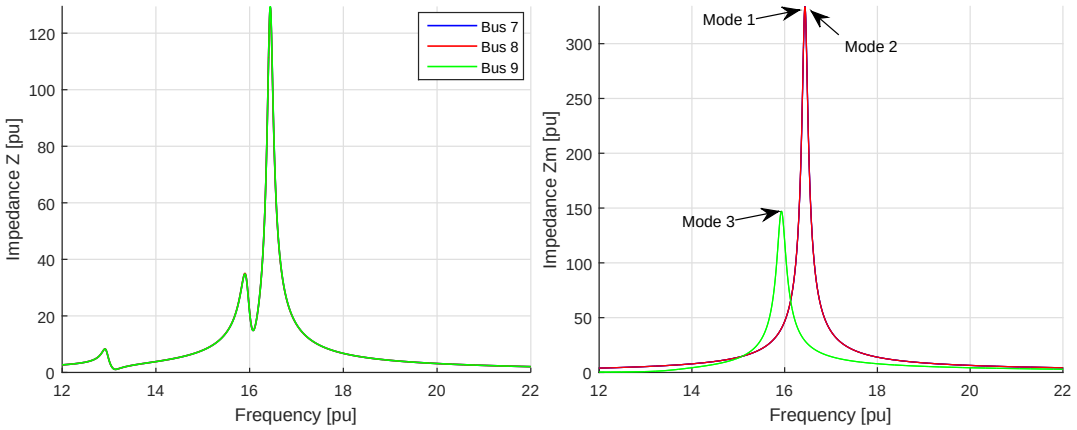

FIGURE 5.13: Driving point impedance at buses 7, 8, and 9 (l.h. figure), and modal scan of three most critical modes (r.h. figure) with symmetric radials. Driving point impedance is identical for the three buses at the end of the radials. The frequency response of two modal variables are identical, while the third modal variable has a differenct frequency response.

TABLE 5.2: Particpation factors of buses 7, 8, and 9 in two most critical modal resoances, i.e. Mode 1 and and Mode 2

	Mode 1	Mode 2
Resonance freq. [pu]	16.44	16.44
Modal impedance peak value Z_m [pu]	344.0	344.0
PF bus 7	0.1917	0.1916
PF bus 8	0.3576	0.0257
PF bus 9	0.0257	0.3577

Long line corrected cable models

In the WPP models presented this far, there are no capacitances besides those associated to cables. Any detected resonance must therefore involve one or more cable capacitances. In the analysis of the 14 bus test case it was suggested that long line corrected cable models should be used when analysing resonances where cable capacitances are heavily involved. HMRA is in this section carried out with such cable models.

The modal impedance scan obtained for the 9 bus WPP model with long line corrected cable models is shown in Figure 5.14. The overall characteristics of the modal impedances are rather similar to the case with nominal cable models, though there are some differences. Bus participation factors for the 7 detected resonance modes are shown in Table 5.3.

Investigation of the resonance modes can be carried out in a similar fashion to the case with nominal cable models. Participation factors quantify the impact of resonance modes in the impedance characteristic at different buses. Sensitivity indices reveal which

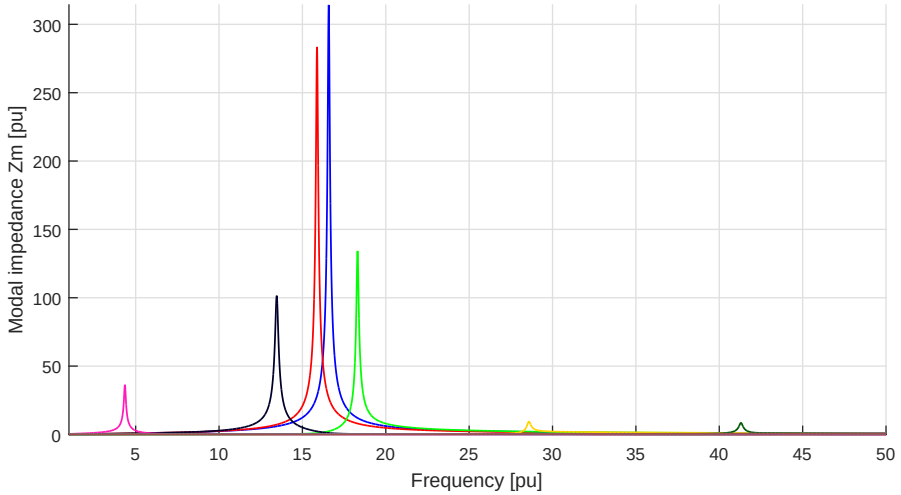

FIGURE 5.14: Modal scan of 9 bus Anholt WPP. There are seven resonance modes, each in a different modal variable.

TABLE 5.3: Participation factors of modal resonances. The largest PF of each mode is marked with solid underline.

f_{res} [pu]	4.356	13.460	15.864	16.569	18.296	28.580	41.298
Z_m [pu]	36.265	101.126	274.587	304.823	132.144	9.313	8.440
Bus 1	0.0281	0.0130	0.0003	0.0002	0.0145	0.2640	0.3219
Bus 2	0.0973	0.0005	0.0001	0.0001	0.0134	0.0101	0.2720
Bus 3	0.1100	0.0151	0.0004	0.0003	0.0099	<u>0.3195</u>	<u>0.3390</u>
Bus 4	0.1259	0.1324	0.1391	0.1621	0.1073	0.0355	0.0010
Bus 5	0.1249	0.1032	0.0275	0.2514	0.2354	0.0485	0.0020
Bus 6	0.1274	0.1980	0.2545	0.0131	0.0503	0.0235	0.0003
Bus 7	0.1286	0.1625	0.1855	0.2222	0.1583	0.0995	0.0212
Bus 8	0.1272	0.1235	0.0354	<u>0.3316</u>	<u>0.3312</u>	0.1176	0.0231
Bus 9	<u>0.1306</u>	<u>0.2518</u>	<u>0.3572</u>	0.0190	0.0797	0.0818	0.0195

parameters the modes are most sensitive to, and hence which circuit elements are most involved in the resonance modes.

Though sensitivity indices are not included, it may be verified the resonance modes at 4.36 pu and 13.46 pu frequency are of similar nature to the resonance modes at 4.34 pu and 12.92 pu frequency for the case with nominal cable models. The resonance modes at 28.58 pu and 41.30 pu are due to export cables, and are also most observable at buses 1 and 3, close to the resonating branches.

The three most critical resonance modes, i.e. those of highest amplitude in the modal domain, are located in close proximity between 15 pu and 19 pu frequency. These resonances are mainly due to array collector cables resonating with offshore substation transformers. However, the characteristics of these modes are somewhat different to the case with nominal cable models. Firstly, two of the modes are most observable at bus 8,

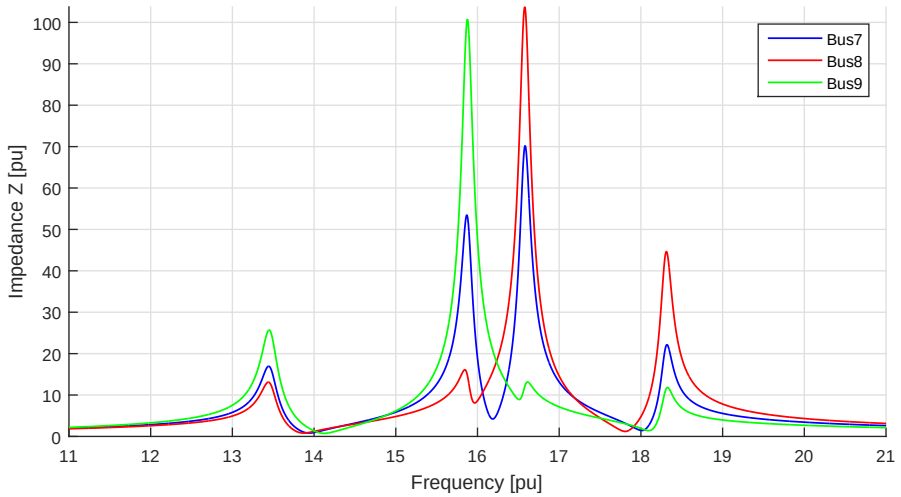

FIGURE 5.15: Driving point impedance at buses 7, 8 and 9 near resonance frequecies due to offshore transformers and collector cables. The three most critical modes are observable at more than one of these buses.

and one mode is most observable at bus 9. This is evident from the participation factors as well as the driving point impedances shown in Figure 5.15. Secondly, the modes are more collaborative in the sense that frequency sensitivity is of comparable magnitude for more parameters than in the case with nominal cable models. This can be observed in the frequency sensitivities for these modes which are shown in Figure 5.16. The export cables are also rather involved in the resonance at 18.31 pu.

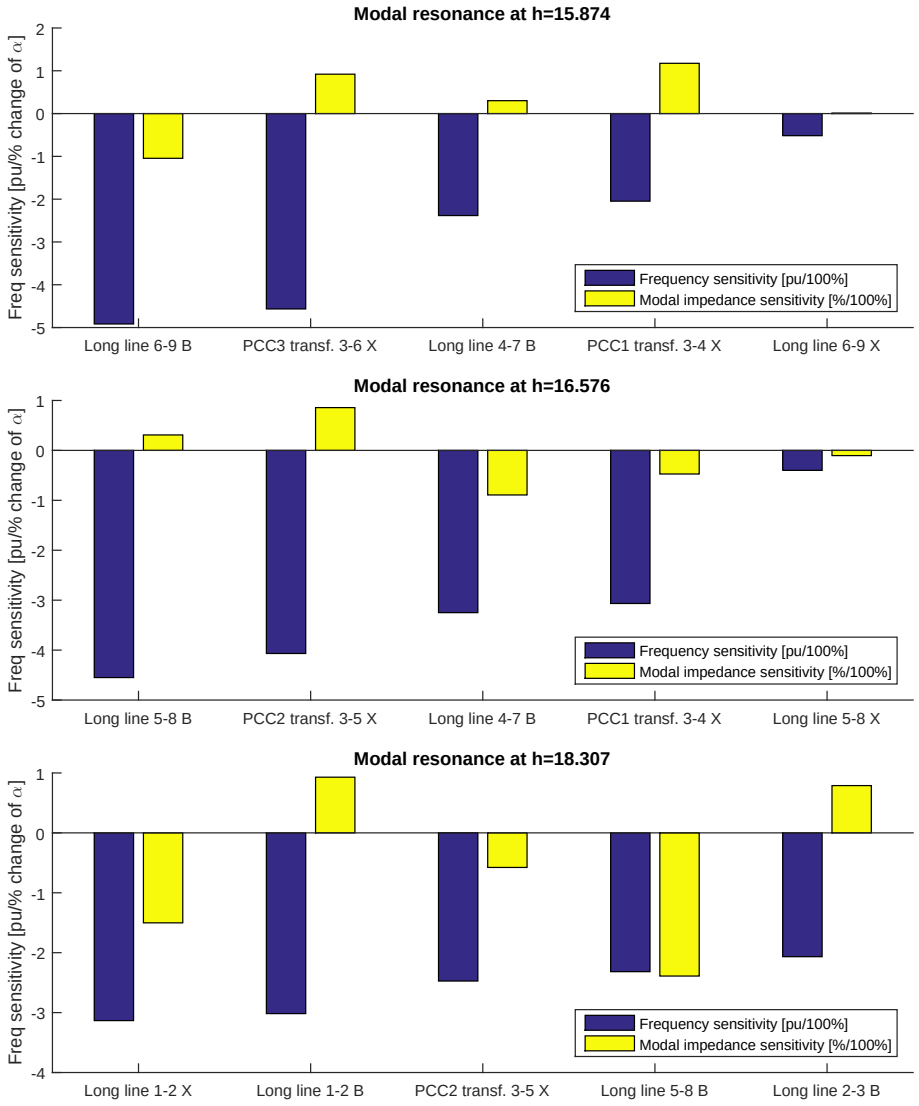

FIGURE 5.16: Sensitivty indices of network parameters with highest frequency sensitivity index for 15.86 pu, 16.57 pu, and 18.31 pu modes.

Skin effect

Skin effect forces the flow of current towards the perimeter of conductors, hence decreasing effective cross-section and increasing resistance. Up to this point, skin effect has been neglected. The impact of taking skin effect into account via the following empirical formula will now be investigated.

$$R = R_1(0.187 + 0.532\sqrt{h}, \quad h > 2.35) \qquad (3.3 \text{ revisited})$$

Figure 5.17 shows the modal impedance envelopes calculated with and without skin effect taken into account. The increased resistance due to skin causes damping of the

resonances peaks, but the mode frequencies remain largely unaltered. The two modes of highest frequency are completely damped when including skin effect.

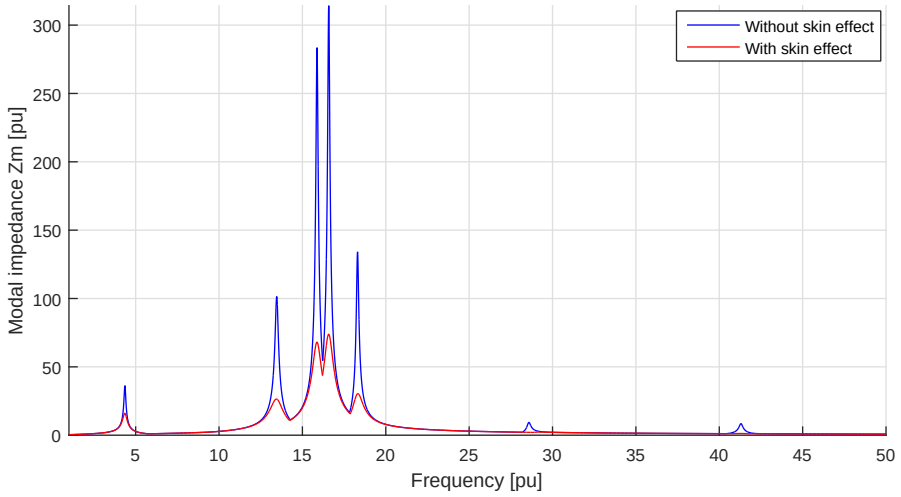

FIGURE 5.17: Modal impedance envelopes of the 9 bus WPP model with long line corrected cable models, with and without inclusion of skin effect. Skin effect dampens resonance peaks, but has little effect on mode frequencies.

The participation factors calculated with skin effect included are shown in Table 5.4. Because participation factors are a relative measure of mode observability at defined buses, there are only minor changes in the participation factors compared to the case without skin effect. Moreover, due to the normalisation of sensitivity indices, these are also virtually unchanged compared to the case without skin effect.

TABLE 5.4: Participation factors of modal resonances with skin effect included. The largest participation factor of each mode is marked with solid underline. Only minor changes is resonance frequencies and participation factors observed due to inclusion of skin effect.

f_{res} [pu]	4.349	13.442	15.861	16.566	18.319
Z_m [pu]	16.016	26.357	65.896	71.649	29.925
Bus 1	0.0279	0.0128	0.0003	0.0002	0.0138
Bus 2	0.0966	0.0005	0.0001	0.0001	0.0128
Bus 3	0.1097	0.0152	0.0004	0.0003	0.0095
Bus 4	0.1260	0.1324	0.1391	0.1615	0.1083
Bus 5	0.1249	0.1034	0.0275	0.2518	0.2352
Bus 6	0.1274	0.1971	0.2543	0.0131	0.0506
Bus 7	0.1290	0.1630	0.1857	0.2216	0.1596
Bus 8	0.1276	0.1242	0.0354	0.3324	0.3304
Bus 9	0.1310	0.2515	0.3571	0.0190	0.0799

5.3 9 Bus Model with WTG Terminal Filters

The sensitivity of HRMA results with respect to WTG harmonic models is investigated in this section. As mentioned in Chapter 3, harmonic sources are often modelled as harmonic current source in frequency domain harmonic studies. It was previously assumed the entire wind turbine circuit, i.e. main reactor, shunt filter and transformer, can be modelled as harmonic current source. Now the wind turbine circuit components are modelled separately, as shown in Figure 5.18. A converter in operation is modelled by short circuiting its terminals. This corresponds to a converter with ideal harmonic rejection, i.e. ideal voltage source behaviour.

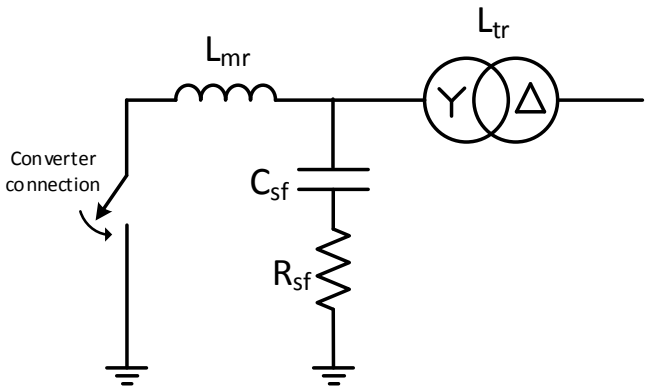

FIGURE 5.18: WTG main circuit model with main reactor, step-up transformer and shunt harmonic filter modelled separately. Ideal harmonic rejection, i.e. ideal voltage source behavior of converter when WTG is connected.

WTG Emission Filter

A set of parameters for the LCL filter of a grid-tied VSC can be determined based on knowledge of the converter topology and ratings as well as step-up transformer short-circuit inductance. Suggested parameters in per unit expressed on a power base equal to Anholt per WTG active power rating of 3.6 MW are given by,

$$L_{mr} = L_{tr} = 0.064\,\text{pu}; \quad C_{sf} = 0.0892 \cdot C_{base} = 11.21\,\text{pu}; \quad R_{sf} = 0.220\,\text{pu}$$

The calculations leading to selection of these parameters are based on well established principles. Further details are included in Appendix D.

HRMA results

The modal impedance envelope is shown in Figure 5.19 for all three WPP models with WTG main circuits energised and all converters connected. Skin effect is also modelled. From the figure one can observe that the shape of the envelope curve is preserved in the aggregated 15 and 9 bus WPP models. The 9 bus model is therefore chosen for further analysis.

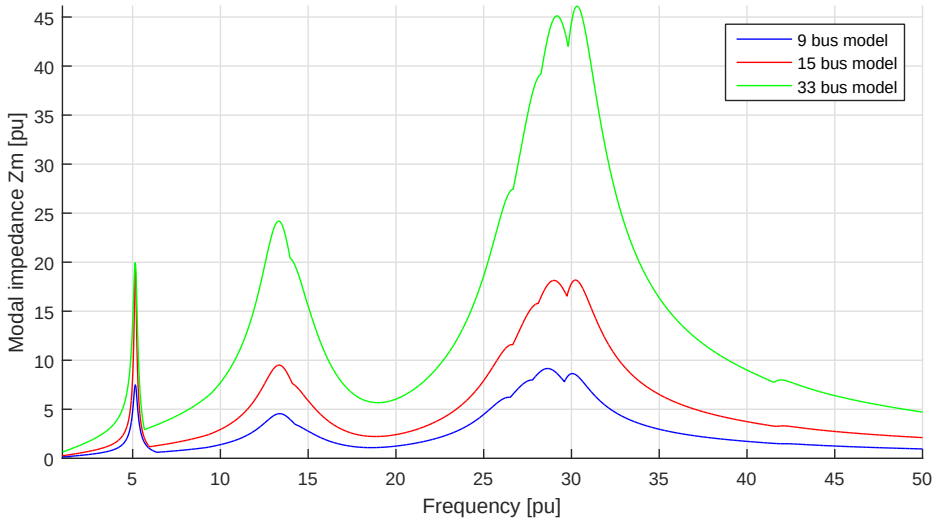

FIGURE 5.19: Modal impedance envelope obtained with WTG main circuits included and all converters connected. The envelope shape is similar for all three WPP models, hence it is assumed the 9 bus model is sufficient.

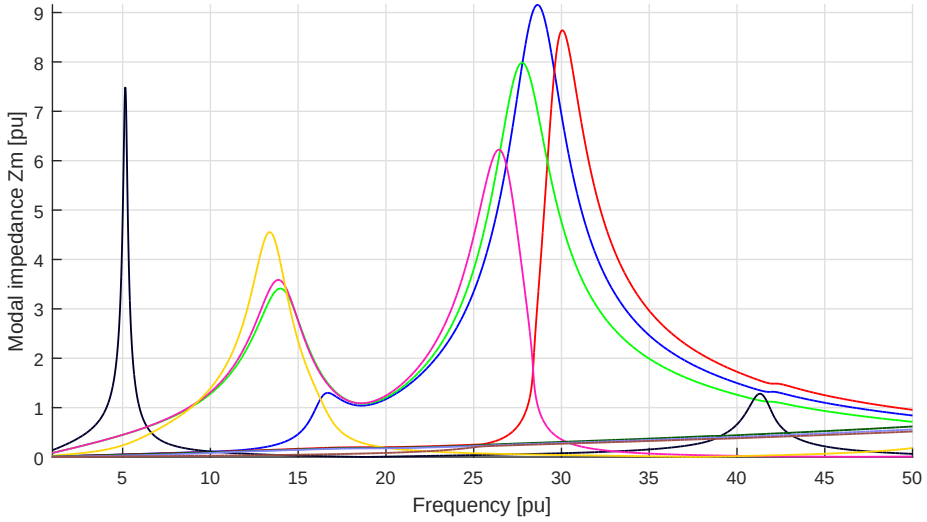

FIGURE 5.20: Modal impedance scan obtained with 9 WPP model, skin effect included and all WTGs connected. There are 10 resoance modes, many of which occur at frequencies close to each other. The resistor in the capacitive high-pass branch introduces significant damping of the resonance modes.

The modal impedance scan for the 9 bus WPP model with skin effect included and all converters connected is shown in Figure 5.20. Ten resonance modes can be identified in the investigated frequency range. Some of the resonance modes are located close to each other, and several resonance modes do not appear in the modal impedance envelope. Considering only the modal envelope hence become insufficient in this case. Participation factors for each resonance mode are listed in Table 5.5, indicating the observability of each resonance mode in driving point impedances.

TABLE 5.5: Participation factors of resonance modes obtained with 9 bus WPP model and all wind turbines connected. The largest PF of each mode is marked with solid underline.

f_{res} [pu]	5.155	13.375	13.870	13.980	26.435	27.760	28.640	30.050	41.310
Z_m [pu]	7.484	4.554	3.586	3.411	6.222	7.982	9.154	8.639	1.281
Bus 1	0.0740	0.0133	0.0002	0.0001	0.0103	0.0029	0.0019	0.0091	<u>0.3209</u>
Bus 2	<u>0.2200</u>	0.0005	0.0000	0.0000	0.0032	0.0003	0.0001	0.0001	0.2706
Bus 3	0.2129	0.0155	0.0002	0.0001	0.0114	0.0037	0.0024	0.0089	0.3388
Bus 4	0.0963	0.1374	0.1729	0.1266	0.0879	<u>0.2626</u>	0.2276	0.0747	0.0085
Bus 5	0.0950	0.1084	0.0311	0.2966	0.0443	0.0446	<u>0.3090</u>	<u>0.4362</u>	0.0101
Bus 6	0.0980	0.2003	0.2271	0.0117	<u>0.4360</u>	0.2530	0.0179	0.0212	0.0065
Bus 7	0.0680	0.1602	0.2236	0.1675	0.0613	0.1988	0.1845	0.0654	0.0150
Bus 8	0.0683	0.1239	0.0391	<u>0.3811</u>	0.0302	0.0327	0.2412	0.3643	0.0156
Bus 9	0.0676	<u>0.2405</u>	<u>0.3056</u>	0.0162	0.3154	0.2014	0.0154	0.0201	0.0141

The algorithms for calculation of sensitivity indices in this thesis are based on modal envelope analysis. Because resonance modes are so close to each other, with several of them not appearing in the modal envelope, the algorithms unfortunately do not work well in this case. It would be possible to overcome this issue by identifying modes for sensitivity index calculation in each modal variable rather than in the envelope. However, this is considered outside the scope of the thesis.

Including the WTG main circuits in the WPP model clearly has a large impact on the modal impedance frequency responses. There are more resonance modes, and the modes are also much more damped. It can be verified that the reduced magnitude of resonance modes is due to resistors in the WTG shunt harmonic filters. In Figure 5.20 there a cluster of four resonance modes between 26 pu and 30 pu frequency. Though the sensitivity indices can not be presented, it has been qualitatively observed that these resonance modes are primarily due to array cables and offshore substation transformers resonance. Hence they are similar to the resonance modes which were located between 13 pu and 19 pu before inclusion of the WTG harmonic main circuit, as shown in Figure 5.14. The resonance modes in the 13-14 pu frequency range appear as a result of including the WTG main circuits.

Previously, when the entire wind turbine circuit was modelled as a current source, it did not make a difference whether or not a turbine was considered in operation. Now it is

assumed the grid-side converter and shunt harmonic filter of an out-of-operation WTG is disconnected, leaving the low voltage side of the step-up transformer open-circuited. Hence there is no damping provided by the shunt harmonic filter of an out-of-operation turbine. The modal impedance envelope as a function of turbines in operation obtained

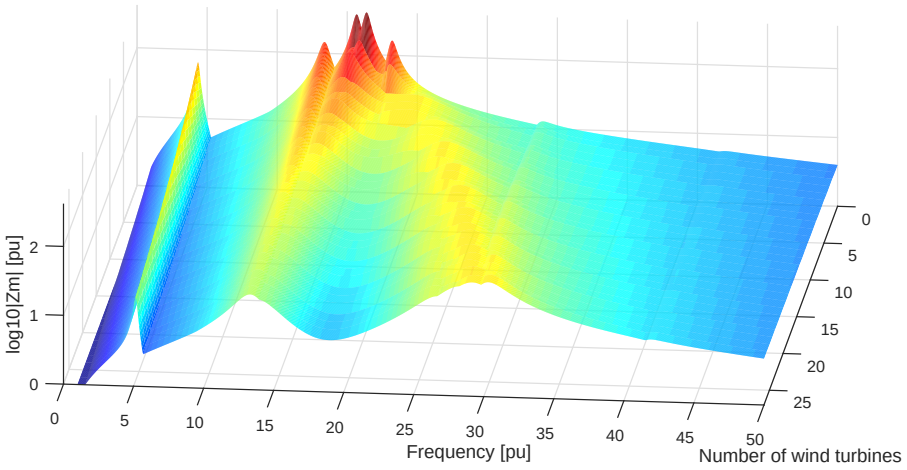

FIGURE 5.21: Three dimensional plot of modal impedance envelope as fuction of number of turbines in operation.

from the 33 bus WPP model is shown in Figure 5.21. The 27 WTG equivalents in this model are disconnected in order of bus number, i.e. the turbine closest to PCCs are disconnected first. The figure illustrates how the modal impedance characteristics of a WPP changes under varying operating conditions. The magnitude of modal impedances are increasingly damped with more turbines in operation, due to the damping effect of the shunt harmonic filters.

The modal impedance scan obtained with the 33 bus WPP model is shown in Figure 5.22. There are some minor differences, but overall the resonance modes are largely similar to those seen in the 9 bus WPP model.

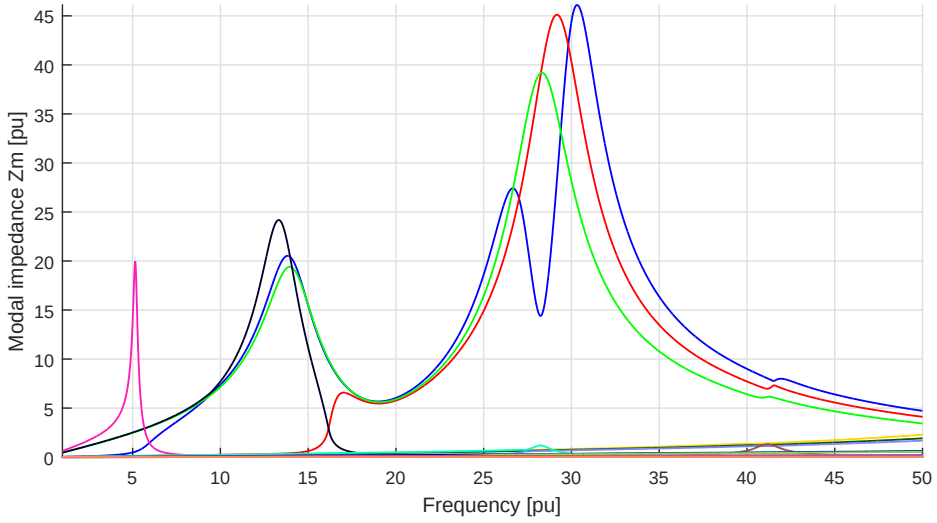

FIGURE 5.22: Modal impedance scan obtained with 33 bus WPP model, skin effect included and all WTGs connected. The resonance modes are largely similar to the ones obtained from the 9 bus model.

Impact of converter control

With the current controllers tuned as indicated in Section 3.5, the following PI-current control parameters are obtained:

$$K_p = \frac{L_{mr}}{2T_{a,pu}} = \frac{0.064}{100\pi \cdot \left(\frac{1.5}{2500}\right)} = 0.169\,\text{pu}$$

$$T_i = \tau_{mr} = \frac{L_{mr}}{(100\pi) \cdot R_{mr}} = \frac{0.064}{100\pi \cdot 0.0064} = 31.8\,\text{ms rad}^{-1} = 10\,\text{pu}$$

The equivalent impedance representing the main reactor and PI current controller is given by

$$\begin{aligned} Z_{eq}(\omega) &= R_{mr} + j\omega L_{mr} + K_p - j\frac{K_p}{\omega T_i} \\ &= (R_{mr} + K_p) + j\left(\omega L_{mr} - \frac{1}{\omega\left(\frac{T_i}{K_p}\right)}\right) \end{aligned} \qquad \text{(3.15 revisited)}$$

The modal impedance frequency response with skin effect and all turbines connected is shown in Figure 5.23. Compared to the case in Figure 5.20, where the equivalent impedance of the current controller is neglected, there are some minor changes of modal frequency responses in the range of 5 pu to 20 pu frequency.

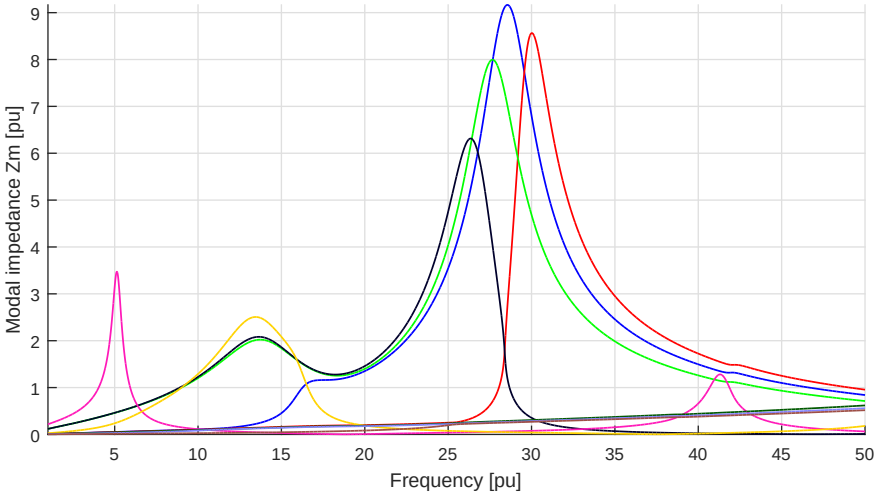

FIGURE 5.23: Modal impedance scan obtained with 9 WPP model, skin effect included, all WTGs connected, and the converter control represented with equivalent impedances. Some small changes can be seen for the modes in the range of 10-15 pu frequency.

6 Discussion

6.1 General Remarks

Frequency responses of the eigenvalues of an admittance matrix allows for locating frequencies associated to parallel resonances. Modal switching should be corrected when obtaining the frequency responses. Unlike a traditional impedance or admittance frequency scan, a modal impedance scan is not linked to a particular location in the circuit. Rather, the modal resonances are linked to the impedance at defined buses via participation factors.

The weighted participation factor, a term coined by Xu et al. [5], has received little attention in published papers. The driving point impedance at some bus for any frequency is the sum of weighted participation factors for the bus in all modal variables. It has been shown in this thesis that when a single WPF approaches the driving point impedance at a resonance frequency, it indicates excitation of a single mode. However, a driving point impedance resonance can also be linked to the excitation of more than one mode. In the WPP analysis, it was shown that it is possible to excite more than one resonance mode simultaneously, i.e. there can be several WPFs of considerable magnitude in a driving point impedance resonance.

In addition to participation factors, a modal impedance sensitivity index and modal frequency sensitivity index have been proposed in literature for quantifying the involvement of different network branches in modal resonances. These sensitivity indices indicate the horizontal and vertical movement of the modal impedance peaks, or modes, in the frequency-impedance plane following a small change in some network parameter of interest. If the harmonic analysis is carried out with the simplifying assumption of circuit element linearity (i.e. constant values of R, L and C), and all branches of interest are modelled as variation of a series RLC branch, the sensitivity indices can be calculated in a simplified way using eigenvectors obtained during the modal impedance scan. This concept was confirmed for the test cases investigated in Chapter 3. It detracts somewhat from the HRMA method that the simplified calculation of the modal sensitivity indices

breaks down when non-RLC branches and non-linear circuit elements are included in the admittance matrix. The sensitivity indices can still be calculated numerically, but with considerable increase of computational time and effort required.

Some papers have suggested buses with high participation factors are good candidates for placing filters if a particular resonance needs to be mitigated [24, 25]. This is arguably true in the sense that a location with large participation in a resonance mode is where the mode is most observable in the driving point impedance. Beyond this simple fact, the results of this thesis do not imply there is anything extraordinary about buses with high participation in a resonance mode. As has been shown, the resonating branches are not necessarily connected at the bus with highest participation factor, Hence it is in the authors opinion not obvious that a resonance mode can best be mitigated at buses with high participation factor in the mode.

If the frequency of a resonance mode is away from frequencies of harmonic emissions, it may not be of concern. If the resonance mode is close to frequencies of existing harmonic emissions, the frequency sensitivity index can be used to reveal which parameters might be adjusted to move the resonance mode to either higher or lower frequencies. A parameter may however affect several resonance modes. Changing a parameter which has favourable impact on one mode thus might have a negative impact on other modes. Hu et al. [8] combined the frequency sensitivity index with an iterative Newton-Raphson based scheme to adjust the size of selected capacitor banks in small industrial power system, thus placing resonance modes at target frequencies.

There is usually some error tolerance with respect to electrical parameters in production and delivery of power system components such as capacitor banks and filters. Hence it may not be possible to predict the exact location of a resonance mode ahead of time. The frequency sensitivity index might be useful in order to decide what margin there needs to be between the frequency of a predicted resonance mode and frequencies of known harmonic emissions. Alternatively the frequency sensitivity index can be used to determine the error tolerance of electrical components based on the frequency of resonance modes and harmonic emissions.

There is arguably a certain elegance to the modal sensitivity indices. They work well with HRMA because the modes are inherent to the system under study, i.e. not linked to a particular bus. On the contrary, the frequency and magnitude of resonances detected via nodal impedance or admittance frequency responses depend on the location at which the scan is obtained. Hence a sensitivity index which is applicable on a system level can not be defined based on traditional methods. However, on a qualitative level

it is possible to reveal the involvement of different electrical network elements in resonances via sensitivity analysis based on traditional impedance and admittance frequency responses [42].

The HRMA described in this thesis is conducted on the positive sequence admittance matrix. Hence it is implicitly assumed the phases are symmetrical, yielding balanced voltages. In reality there is however always some degree of phase unbalance. In a system with considerable unbalance, the resonance frequencies can be different in each phase. Unbalance can occur for a number of reasons. For example, line transpositions can be ineffective for harmonic frequencies. Another cause of phase unbalance might be cables laid in flat formation, i.e. without transpositions. In industry the symmetrical analysis is of limited value due to unbalance being the norm [12]. State of the art software for harmonic analysis such as DigSilent PowerFactory allows for specifying unbalances, hence it can be reflected in frequency scans and in harmonic power flow analysis [15]. If the HRMA method is to find application in industry, it would likely have to be expanded to cover unbalanced systems. Whether the principles of HRMA can be extended to non-symmetrical representation remains an open question.

6.2 Wind Power Plant Analysis

In Chapter 5 HRMA was used to analyse a large offshore WPP. The results have not been validated with any real measurements, and so the accuracy of the WPP model is uncertain.

The modes in the studied WPP showed a tendency to group together. In other words several resonance modes are close to each other in terms of resonance frequency and modal impedance magnitude. Resonances in driving point impedance are therefore sometimes linked to excitation of more than one mode, i.e. the driving point impedance can not be estimated by a single WPF. Moreover, in the particular case where there is perfect radial symmetry in the studied system, it was shown that two modal variables can have identical frequency response. Clearly taking only the modal impedance envelope into account is insufficient when studying such large WPPs.

The most critical modes were shown to be associated to resonance between the inductances of offshore substation transformers and array collector cable capacitances. The inclusion of frequency dependent resistance (i.e. skin effect) did not cause considerable changes in the frequency of resonance modes, participation factors or sensitivity indices. On the contrary, inclusion of long line corrected cable models had a quite significant impact on frequencies of resonance modes, participation factors and sensitivity indices.

The frequency and magnitude of resonance modes were shown be highly dependent on the number of turbines in operation. All potential operating conditions must therefore be considered in resonance analysis of such large offshore WPPs.

The analysis showed that the HRMA results are quite sensitive to modelling of the WTG circuit components, i.e. step-up transformers, shunt harmonic filters and main reactors. Hence these components should be included in the resonance analysis. In Section 3.5 it was shown from a theoretical perspective how the current controller of a VSC can influence the impedance as seen from the grid. In the HRMA analysis only a minor effect was observed in the resonance modes when including the current controller.

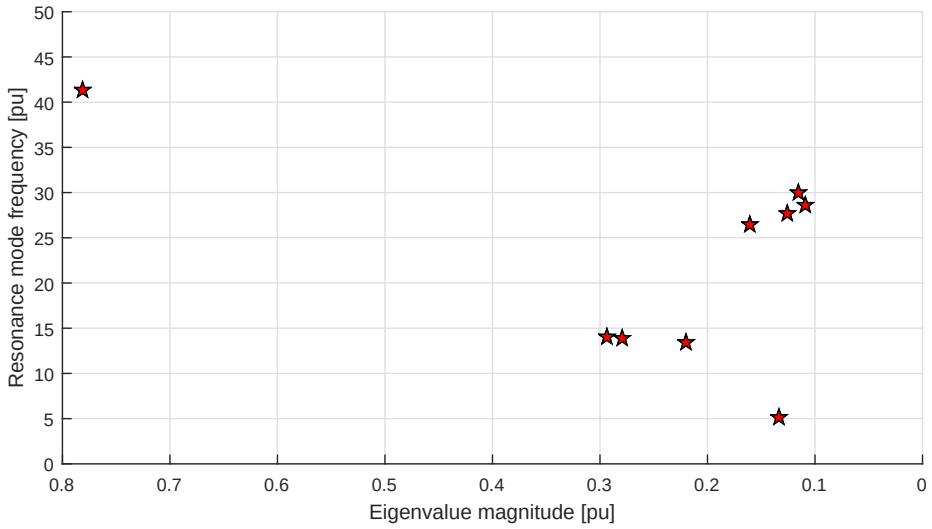

FIGURE 6.1: Root locus style presentation of resonance modes observed in 9 bus WPP model with all WTG connected. A small eigenvalue, associated with a large modal impedance, places the mode far to the right in the diagram, indicating poor damping of the resonance.

An alternative presentation of the resonance modes is shown in Figure 6.1. The figure emulates the left half plane of a root-locus diagram, and thus will be familiar to anyone with knowledge of small signal stability analysis. The eigenvalue magnitude and frequency of resonance modes are plotted against each other. Resonance modes with little damping have small eigenvalue magnitudes, and are located far to the right in the diagram. The frequencies of the resonance modes are indicated on the y-axis. Eigenvalues can not take on negative values, hence modes in the right half plane, which indicate instability in small signal analysis, can not occur here. From the root locus style diagram one can clearly see the grouping of the resonance modes. It can also be used to illustrate the movement of the resonance modes following some parameter change in the system.

7 Conclusions

The findings in analysis of test cases were consistent with those presented in published papers. Certain issues in implementation, particularly the issue of modal switching, has not received sufficient attention in past papers, but are critical for meaningful presentation and interpretation HRMA results. The combination of resonance modes, participation factors and sensitivity indices can provide a good overview of parallel resonances in a power system.

The finding of this thesis indicate HRMA method can potentially give some guidance for solving problems related to harmonic resonance in offshore WPPs. There is ample potential for resonances to cause problems in offshore WPPs, particularly because the resonance points change with number of turbines in operation. The obtained results were sensitive to modelling of elements within each WTG circuit.

7.1 Further Work

The matrix formulation and methodology suitable for analysis of series resonances has received little attention in literature, and could be investigated further. Also, there is a need to define and verify suitable mitigation strategies based on HRMA. Assumptions and modelling for HRMA could be verified by comparing results with state of the art simulation software such as DigSilient PowerFactory and/or real measurements. Additionally it would be worth investigating if the HRMA method can be applied to non-symmetrical systems by using a three-phase rather than positive sequence representation in the admittance matrix.

A HRMA Test Case Input Data and Results

A.1 Input Data IEEE 14 Bus Test System

TABLE A.1: IEEE 14 bus test case stedy state load flow [38]

Bus #	Nominal voltage (kV)	P Load (pu)	Q Load (pu)	LF Voltage (pu)	LF angle (deg)	THD (%)
1	230	0	0	1,0600	0,00	1,767
2	230	0	0	1,0450	5,68	2,177
3	230	0	0	1,0427	15,30	1,516
301	35,4	0,50905	0,03363	1,0417	-16,18	9,169
302	35,4	0,50905	0,03363	1,0417	-16,18	9,169
4	230	0,47790	-0,03900	1,0282	-11,41	0,755
5	230	0,07599	0,01599	1,0337	-9,82	1,462
6	230	0	0	1,0700	-15,87	0,468
7	230	0	0	1,0193	-14,47	0,423
8	13,8	0	0,12900	1,0209	-14,49	0,522
9	115	0,29499	16,59900	1,0147	-16,09	0,482
10	115	0,09000	0,05799	1,0168	-16,33	0,421
11	115	0,03501	0,01800	1,0394	-16,21	0,394
12	115	0,06099	0,01599	1,0528	-16,72	0,391
13	115	0,13500	0,05799	1,0458	-16,73	0,376
14	115	0,14901	0,05001	1,0154	-17,39	0,343

TABLE A.2: IEEE 14 bus test case generator input data [38]

Bus #	Bus Type	Voltage setting (pu)	P gen. (pu)	Q gen. (pu)	Sub-transient X (pu)
1	Slack	1.0600	2.618681	-0.02863	0.25
2	PV	1.0450	0.18300	5.857	0.25
6	PV	1.0700	-0.11200	44.200	0.25

TABLE A.3: IEEE 14 bus test case branch parameters [38]

Branch Type	From Bus #	To Bus #	R1 (pu)	X1 (pu)	B1 (pu)
Transformer (Y-Y)	4	7	0.00000	0.20900	
Transformer (Y-Y)	4	9	0.00000	0.55618	
Transformer (Y-Y)	5	6	0.00000	0.25020	
Transformer (Y-Δ)	7	8	0.00000	0.17615	
Transformer (Y-Y)	7	9	0.00000	0.11000	
OH Line	6	11	0.09495	0.19887	
OH Line	6	12	0.12285	0.25575	
OH Line	6	13	0.06613	0.13024	
OH Line	9	10	0.03181	0.08448	
OH Line	9	14	0.01270	0.27033	
OH Line	10	11	0.08203	0.19202	
OH Line	12	13	0.22087	0.19985	
OH Line	13	14	0.17089	0.34795	
OH Line	1	2	0.01937	0.05916	0.05279
OH Line	1	5	0.05402	0.22300	0.04920
OH Line	2	3	0.04697	0.19794	0.04380
OH Line	2	4	0.05810	0.17628	0.03740
OH Line	2	5	0.05693	0.17384	0.03386
OH Line	3	4	0.06700	0.17099	0.03460
OH Line	4	5	0.01335	0.04209	0.01280
Capacitor (pf correction)	9	0	0.00000	0.00000	0.06330
Filter order: 2nd	8	0	0.52510	8.31233	0.03015
Filter order: 5th	8	0	0.52510	1.32635	0.03015
Filter order: 7th	8	0	0.52510	0.67307	0.03015
Filter order: 11th	8	0	0.52510	0.27515	0.03015
Filter order: 11th	3	0	0.00136	0.02772	0.24916
Filter order: 11th	3	0	0.00136	0.02772	0.24916
Transformer (Y-Y)	3	301	0.00000	0.02800	0.00000
Transformer (Y-Δ)	3	302	0.00000	0.02800	0.00000

A.2 Test Case Results

TABLE A.4: Participation factors for all buses and modal resonances in modal scan envelope. The largest participation factor for each frequency is underlined.

Freq [pu]	1.917	2.869	4.212	5.874	8.627	10.738	14.458	25.261	25.943
Zm [pu]	4.4553	9.3417	7.9056	4.5109	6.8356	12.4556	13.1867	22.5070	18.0491
Bus 1	0.0277	0.0556	0.0005	0.0044	0.0427	0.2027	0.0279	0.0027	0.3742
Bus 2	0.0347	0.0742	0.0012	0.0036	0.0364	0.1699	0.0192	0.4026	0.0029
Bus 3	0.0763	0.2632	0.0469	0.0060	0.0013	0.0003	0.0000	0.0078	0.0097
Bus 4	0.0585	0.0972	0.0006	0.0139	0.0455	0.1096	0.0003	0.0976	0.3682
Bus 5	0.0483	0.0802	0.0003	0.0123	0.0542	0.1592	0.0021	0.4138	0.1926
Bus 6	0.0299	0.0257	0.0055	0.0228	0.0464	0.0336	0.0144	0.0306	0.0111
Bus 7	0.1207	0.0769	0.1258	0.1395	0.1074	0.0460	0.0985	0.0025	0.0128
Bus 8	0.2705	0.1000	0.6543	0.4359	0.1149	0.0040	0.0117	0.0005	0.0026
Bus 9	0.0806	0.0555	0.0575	0.0985	0.1376	0.0800	0.3618	0.0051	0.0112
Bus 10	0.0705	0.0467	0.0426	0.0834	0.1202	0.0598	0.2284	0.0008	0.0040
Bus 11	0.0508	0.0351	0.0202	0.0531	0.0870	0.0420	0.0843	0.0048	0.0004
Bus 12	0.0358	0.0258	0.0073	0.0312	0.0577	0.0270	0.0167	0.0174	0.0056
Bus 13	0.0363	0.0264	0.0087	0.0315	0.0561	0.0277	0.0222	0.0137	0.0041
Bus 14	0.0594	0.0377	0.0285	0.0640	0.0927	0.0382	0.1125	0.0001	0.0007

B Details of HRMA

B.1 2-norm of Eigenvectors

Given an n-dimensional vector

$$\mathbf{x} = \begin{bmatrix} x_1 \\ x_2 \\ \vdots \\ x_n \end{bmatrix}$$

The p-norm of a vector is defined as

$$|x|_p = \left(\sum_i |x_i|^p \right)^{(1/p)} \tag{B.1}$$

The 2-norm is equal to one for all eigenvectors returned by the built-in eig()-function in MATLAB. An eigenvector $\mathbf{x}$ hence fulfils

$$|x| = x_1^2 + x_2^2 + \cdots + x_n^2 = 1 \tag{B.2}$$

B.2 Modal Sensitivity Indices Differential Expressions

In order to calculate modal frequency sensitivities of a branch in the power network, it is necessary to evaluate derivatives $\partial G_{br}/\partial\alpha$, $\partial^2 G_{br}/\partial\alpha\partial f$, $\partial B_{br}/\partial\alpha$ and $\partial^2 B_{br}/\partial\alpha\partial f$. Many branches, such as first order filters, shunt capacitors, and shunt reactors, can be fully represented by a series RLC branch.

Defining

$$|Z| = \sqrt{R_1^2 + h^2 \left(X_1 - \frac{1}{h^2 B_1} \right)^2}$$

and expressing conductance and susceptance of the RLC branch in terms of harmonic order h, resistance R_1, inductive reactance X_1, and capacitive susceptance B_1:

$$G_{br} = \frac{R_1}{R_1^2 + h^2\left(X_1 - \frac{1}{h^2 B_1}\right)^2} = \frac{R_1}{|Z|^2} \tag{B.3}$$

$$B_{br} = \frac{h\left(\frac{1}{h^2 B_1} - X_1\right)}{R_1^2 + h^2\left(X_1 - \frac{1}{h^2 B_1}\right)^2} = \frac{h\left(\frac{1}{h^2 B_1} - X_1\right)}{|Z|^2} \tag{B.4}$$

Expressions for the first order derivatives of G_{br} and B_{br} with respect to X_1 and B_1 are given by

$$\frac{\partial G_{br}}{\partial X_1} = \frac{2h^2 R_1\left(\frac{1}{h^2 B_1} - X_1\right)}{|Z|^4}$$

$$\frac{\partial B_{br}}{\partial X_1} = \frac{2h^3\left(X_1 - \frac{1}{h^2 B_1}\right)^2}{|Z|^4} - \frac{h}{|Z|^2}$$

$$\frac{\partial G_{br}}{\partial B_1} = \frac{2R_1\left(\frac{1}{h^2 B_1} - X_1\right)}{B_1^2|Z|^4}$$

$$\frac{\partial B_{br}}{\partial B_1} = \frac{2h\left(X_1 - \frac{1}{h^2 B_1}\right)^2}{B_1^2|Z|^4} - \frac{1}{hB_1^2|Z|^2}$$

The expressions for second order partial derivatives of G_{br} and B_{br} with respect to harmonic order and either X_1 or B_1 become highly complex. Expressions for these terms have been obtained using Maple software from Maplesoft, and the expressions are evaluated in MATLAB. Maple-generated expressions are included for sake of completeness.

$$\frac{\partial^2 G_{br}}{\partial X_1 \partial h} = \frac{-4Rh^3B^3(-B^3X^3h^6 + B^3R^2Xh^4 + 3BXh^2 - 2)}{(B^2X^2h^4 + B^2R^2h^2 - 2BXh^2 + 1)^3}$$

$$\frac{\partial G_{br}}{\partial B_1 \partial h} = \frac{4R_1hB_1(2B_1^3X_1^3h^6 - 3B_1^2X_1^2h^4 - B_1^2R_1^2h^2 + 1)}{(B_1^2X_1^2h^4 + B_1^2R_1^2h^2 - 2B_1X_1h^2 + 1)^3}$$

$$\frac{\partial^2 B_{br}}{\partial X_1 \partial h} = \frac{-h^2B^2(B^4X^4h^8 - 6B^4R^2X^2h^6 + B^4R^4h^4 - 6B^2X^2h^4 + 6B^2R^2h^2 + 8BXh^2 - 3)}{(B^2X^2h^4 + B^2R^2h^2 - 2BXh^2 + 1)^3}$$

$$\frac{\partial^2 B_{br}}{\partial B_1 \partial h} = \frac{(-3B^4X^4h^8 + 6B^4R^2X^2h^6 + B^4R^4h^4 + 8B^3X^3h^6 - 6B^2X^2h^4 - 6B^2R^2h^2 + 1)}{(B^2X^2h^4 + B^2R^2h^2 - 2BXh^2 + 1)^3}$$

C Offshore WPP Analysis

C.1 Anholt WPP Collector Array Layout

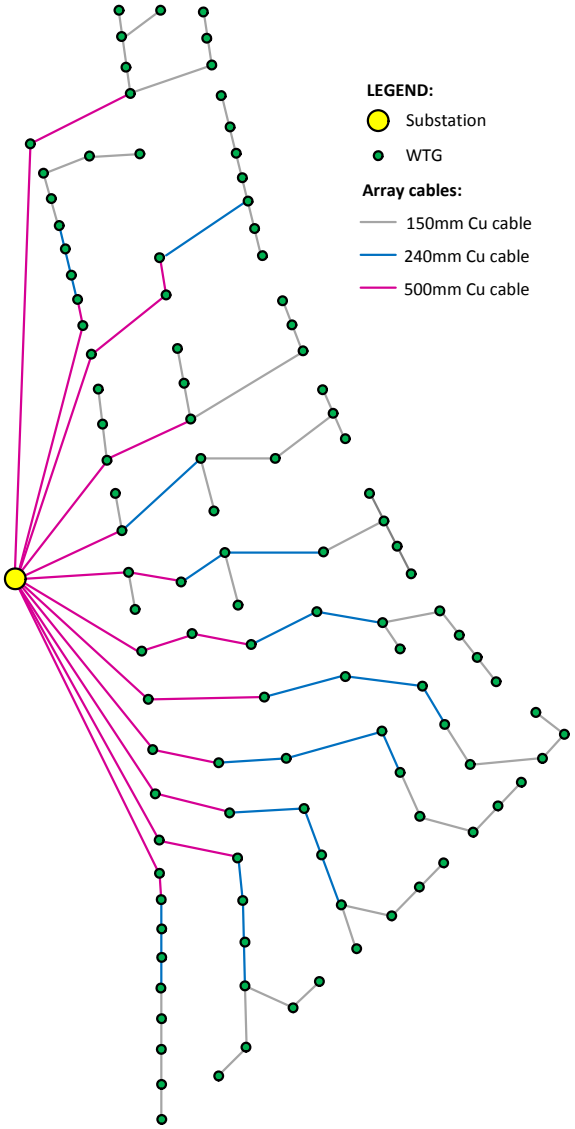

Figure C.1

C.2 Input Data

TABLE C.1: Data for three-core Cu-conductor submarine array cables of nominal voltage 33 kV (U_m=36 kV) Values taken from ABB user's guide [40].

Cross section [mm^2]	150	240	500
Inductance [mH/km]	0.41	0.38	0.34
Capacitance [µF/km]	0.21	0.24	0.32
Current rating [A]	375	480	655

C.3 Results 9 Bus Model with Nominal Cable Models

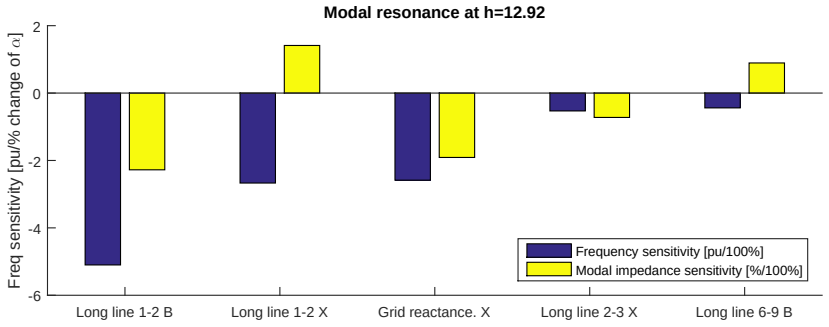

FIGURE C.2: Sensitivty indices of the five parameters with highest frequency sensitivty index with respect to the modal resoance at 12.92 pu frequency. The underground export cable resonates with the grid reactance.

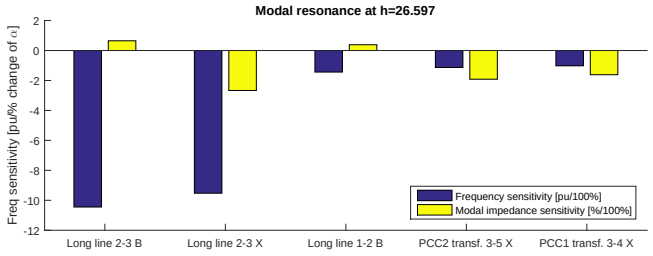

FIGURE C.3: Sensitivty indices of the five parameters with highest frequency sensitivty index with respect to the modal resoance at 26.60 pu frequency. The submarine export cable reactance and shunt capcitance is most involved in this resonace mode.

D LCL Filter Design Grid-tied VSC

The design criteria and methodology used for determining filter parameters in this thesis is in accordance with the author's specialisation project [9] and related paper [10], which again were predominantly based on pre-existing literature [30, 43–45].

Base values given by WTG rated active power and rated AC side voltage are given in table D.1.

TABLE D.1: Per unit base values wind turbine emission filter design

Parameter	Symbol	Equation	Value	Unit
Power	$S_{base} = P_n$	-	3.6	MVA/MW
Voltage	V_{base}	-	0.69	kV
Frequency	f_1	-	50	Hz
Current	I_{base}	$\frac{S_{base}}{\sqrt{3}V_{base}}$	3012	A
Impedance	Z_{base}	$\frac{V_{base}^2}{S_{base}}$	0.13225	Ω
Inductance	L_{base}	$\frac{Z_{base}}{2\pi f_1}$	0.4210	mH
Capacitance	C_{base}	$\frac{1}{2\pi f_1 Z_{base}}$	24.07	mF
DC voltage	$V_{dc,base}$	$\frac{2\sqrt{2}V_{base}}{\sqrt{3}}$	1.127	kV

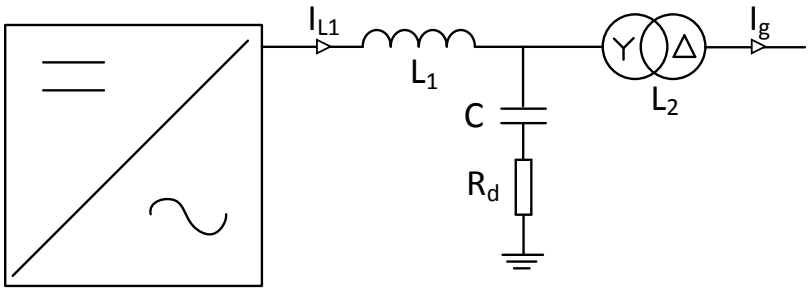

FIGURE D.1: LCL filter for grid-tied VSC with nomenclature

With reference to Figure D.1, constraints typically imposed on the LCL filter design include:

1. The converter side inductor L_1 should by itself be large enough to limit the ripple current to 10 % of the rated converter current amplitude.

2. The total inductance of L_1+L_2 should be no larger than 10 % to limit the maximum voltage drop across the filter and subsequent need for high DC side voltage.

3. The reactive power provided by the capacitor should be limited to approximately 5 % of rated power in order to limit reactive power variation seen from the grid.

4. The filter resonance frequency, given by

$$f_{res} = \frac{1}{2\pi}\sqrt{\frac{L_1 + L_2}{L_1 L_2 C}} \quad [\text{Hz}] \tag{D.1}$$

should be placed in the band of $10f_1 \leq f_{res} \leq 0.5f_{sw}$ where f_{sw} is the carrier switching frequency. The is aimed at ensuring the resonance frequency is much lower than that of the lowest carrier band harmonics, and is high enough to not cause controller stability issues.

5. The filter resonance frequency must be damped either passively or actively. Passive damping is the most straightforward solution, but typically results in higher losses and reduced filtering performance compared to active damping. A resistor of magnitude

$$R_d = \frac{1}{3}\frac{1}{\omega_{res} C}$$

where ω_{res} is the filter resonance frequency, will ensure damping of the filter resonance.

6. It is generally considered that the LCL filter should attenuate the current ripple to 2 % of the rated current amplitude of the converter, i.e. $0.02\sqrt{2}I_{base}$, in order to comply with relevant grid code.

Some assumptions regarding certain elements of the Anholt offshore wind power plant must be made in order to continue the LCL filter design:

- It is assumed a switching frequency f_{sw} is as high as 2.5 kHz is feasible for the WTG converters.
- It is assumed the converter is able to deliver rated active power of 3.6 MW at a power factor of ±0.9 for maximum active power. This implies a converter rating of 4 MVA.
- An MVA rating of 4.5 MVA with a SC reactance 8 % is assumed for the step up transformer. On the 3.6 MW base of Table D.1 this corresponds to an inductance of 6.4 %.

- It is assumed the semiconductor capacity does not present the binding constraint on the DC side voltage.

The maximum ripple current as function of the converter side inductance L_1 can be derived from the converter topology using voltage-second balance. For a two-level converter the ripple current as a function of inductor value can be expressed as

$$\Delta I_{L1,max} = \frac{V_{dc}}{8 f_{sw} L_1} \tag{D.2}$$

and for a three-level neutral point clamped topology the voltage-second balance across inductor L_1 yields

$$\Delta I_{L1,max} = \frac{V_{dc}}{16 f_{sw} L_1} \tag{D.3}$$

It may be verified that the current ripple at the grid-side of the LCL filter is approximately,

$$\Delta I_{g,max} = \Delta I_{L1,max} \cdot \frac{1}{|1 + \frac{L_1}{L_2}\left(1 - L_1 C (2\pi f_{sw})^2\right)|} \tag{D.4}$$

Assuming now that the inductance L_2 of the step-up transformer is fixed at 6.4 %, the overall attenuation achieved for different values of inductance L_1 and the capacitor C can be plotted as in figure D.2 an figure D.3 for two- and three-level converters respectively. The figures show it is not possible to find a solution adhering to all constraints for either two-level or three-level converter topology. It may also be verified that increasing L_2 only makes the situation even worse.

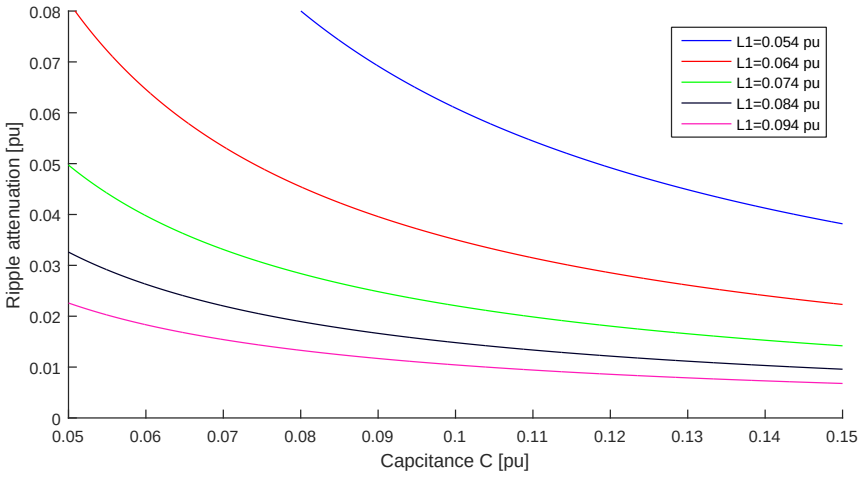

FIGURE D.2: Ripple attenuation as function of capacitance C for different sizes of inductor L_1, two-level VSC.

The topology of the converter used in Anholt's turbines is not known, hence an assumption must be made. It is therefore assumed that the converter has a 3-point neutral point

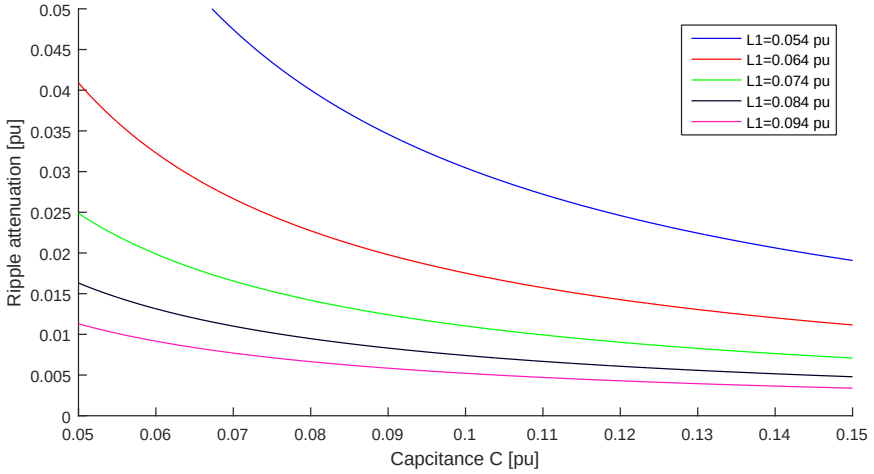

FIGURE D.3: Ripple attenuation as function of capacitance C for different sizes of inductor L_1, three-level VSC.

clamped topology. Moreover, a trade off must be made to find a filtering solution outside of the suggested constrained area. Hence it is assumed the grid-side converter can operate with a total inductance somewhat higher than 10 %. Due to the flexible power factor operation of the converter, there is arguably some flexibility on the constraint number three, which limits the size of the capacitor. The desired ripple attenuation of the ripple to 2 % of the peak rated current can thus be achieved with the following sizing of the LCL-filter components,

$$L_1 = L_2 = 0.064\,\text{pu}, \quad C = 11.21\,\text{pu}, \quad \text{or} \quad x = 0.0892 \quad \text{where} \quad C = xC_{base}$$

The resonance frequency with these parameters is located at the 18.72 pu frequency.

A resistor of magnitude

$$R_d = 0.220\,\text{pu}$$

can be installed in series with the shunt capacitor to provide damping of the filter resonance. A resistor in series with the shunt capacitor is a rather crude way to provide damping of the LCL filter resonance, in part due to high losses with such a solution. Better performance can be achieved using active damping or by more sophisticated passive filter design.

The chosen capacitor produces 0.0892 pu or 0.321 MVA reactive power. For high converter power output the reactive power contribution from the capacitor is largely offset by filter inductors. The power factor at the grid-side filter terminals can hence be controlled by adjusting the power factor operation of the converter.

More sophisticated filter design methods might reveal that better utilisation of the capacitance can be achieved by specifically targeting the carrier band harmonics which are characteristic for a grid-tied voltage source converter. For example, an inductor might be inserter in series with the capacitor to form an LC branch tuned to the first group of carrier band harmonics, or several LC shunt branches might each be tuned to one group of carrier band harmonics. Such solutions might allow for reducing the size of L_1 and C, hence finding a solution within the boundary of the constraints. Such considerations are outside of the scope of this thesis.

Bibliography

[1] IEA. Technology roadmap: Wind energy - 2013 edition, 2013.

[2] EY. Offshore wind in europe: Walking the tightrope to success, 2015.

[3] Math H Bollen and Irene Gu. *Signal processing of power quality disturbances*, volume 30. John Wiley & Sons, 2006.

[4] Łukasz Hubert Kocewiak, Jesper Hjerrild, and Claus Leth Bak. Wind turbine converter control interaction with complex wind farm systems. *IET Renewable Power Generation*, 7(4):380–389, 2013.

[5] Wilsun Xu, Zhenyu Huang, Yu Cui, and Haizhen Wang. Harmonic resonance mode analysis. *Power Delivery, IEEE Transactions on*, 20(2):1182–1190, April 2005. ISSN 0885-8977. doi: 10.1109/TPWRD.2004.834856.

[6] Zhenyu Huang, Yu Cui, and Wilsun Xu. Application of modal sensitivity for power system harmonic resonance analysis. *Power Systems, IEEE Transactions on*, 22 (1):222–231, Feb 2007. ISSN 0885-8950. doi: 10.1109/TPWRS.2006.883678.

[7] Yu Cui and Xiaoyu Wang. Modal frequency sensitivity for power system harmonic resonance analysis. *Power Delivery, IEEE Transactions on*, 27(2):1010–1017, April 2012. ISSN 0885-8977. doi: 10.1109/TPWRD.2012.2185520.

[8] Haitao Hu, Zhengyou He, Yangfan Zhang, and Shibin Gao. Modal frequency sensitivity analysis and application using complex nodal matrix. *Power Delivery, IEEE Transactions on*, 29(2):969–971, April 2014. ISSN 0885-8977. doi: 10.1109/TPWRD.2013.2288012.

[9] Henrik Andreas Broch Brantsæter. *Specialisation project: Wind Turbine and Offshore Wind Power Plant Modelling for System Level Harmonic Studies*. Norwegian University of Science and Technology (NTNU), 2014.

[10] Henrik Brantsæter, Łukasz Kocewiak, Atle Rygg Årdal, and Elisabetta Tedeschi. Passive filter design and offshore wind turbine modelling for system level harmonic studies. *Energy Procedia*, 80:401 – 410, 2015. ISSN 1876-6102. doi:

http://dx.doi.org/10.1016/j.egypro.2015.11.444. 12th Deep Sea Offshore Wind R&D Conference, {EERA} DeepWind'2015.

[11] C. Larose, R. Gagnon, P. Prud'Homme, M. Fecteau, and M. Asmine. Type-iii wind power plant harmonic emissions: Field measurements and aggregation guidelines for adequate representation of harmonics. *Sustainable Energy, IEEE Transactions on*, 4(3):797–804, July 2013. ISSN 1949-3029. doi: 10.1109/TSTE.2013.2252209.

[12] N.R. Watson J. Arrillaga. *Power System Harmonics*. John Wiley & Sons, 2 edition, 2003.

[13] Kai Yang. *Wind-Turbine Harmonic Emmission and Propagation through A Wind Farm*. Master Thesis, Lulea University of Technology, 2012.

[14] Task Force on Harmonics Modeling and Simulation. Modeling and simulation of the propagation of harmonics in electric power networks. Part I: Concepts, models, and simulation techniques. *Power Delivery, IEEE Transactions on*, 11(1):452–465, Jan 1996. ISSN 0885-8977. doi: 10.1109/61.484130.

[15] *DigSILENT PowerFactory 15 User Manual*.

[16] K.N.M. Hasan, K. Rauma, P. Rodriguez, J.I. Candela, R.S. Munoz-Aguilar, and A. Luna. An overview of harmonic analysis and resonances of large wind power plant. In *IECON 2011 - 37th Annual Conference on IEEE Industrial Electronics Society*, pages 2467–2474, Nov 2011. doi: 10.1109/IECON.2011.6119697.

[17] Task Force on Harmonics Modeling and Simulation. Modeling and simulation of the propagation of harmonics in electric power networks. Part II: Sample systems and examples. *Power Delivery, IEEE Transactions on*, 11(1):466–474, Jan 1996. ISSN 0885-8977. doi: 10.1109/61.484131.

[18] SJ Ranade and W Xu. An overview of harmonics modeling and simulation. *IEEE Task Force on Harmonics Modeling and Simulation*, page 1, 2007.

[19] Jan Machowski, Janusz W. Bialek, and James R. Bumby. *Power System Dynamics Stability and Control*. John Wiley & Sons Ltd., 2 edition, 2008.

[20] Yu Cui and Wilsun Xu. Harmonic resonance mode analysis using real symmetrical nodal matrices. *Power Delivery, IEEE Transactions on*, 22(3):1989–1990, July 2007. ISSN 0885-8977. doi: 10.1109/TPWRD.2007.899481.

[21] Masoud Esmaili, Heidar Ali Shayanfar, and Alireza Jalilian. Modal analysis of power systems to mitigate harmonic resonance considering load models. *Energy*, 33 (9):1361–1368, 2008.

[22] K. Rauma, K.N. Md Hasan, C. Gavriluta, and C. Citro. Resonance analysis of a wind power plant with modal approach. In *Industrial Electronics (ISIE), 2012 IEEE International Symposium on*, pages 2042–2047, May 2012. doi: 10.1109/ISIE.2012.6237408.

[23] K.N.M. Hasan, K. Rauma, A. Luna, J.I. Candela, and P. Rodriguez. Study on harmonic resonances and damping in wind power plant. In *Intelligent and Advanced Systems (ICIAS), 2012 4th International Conference on*, volume 1, pages 418–423, June 2012. doi: 10.1109/ICIAS.2012.6306230.

[24] K.N. Binti Md Hasan, K. Rauma, A. Luna, J.I. Candela, and P. Rodriguez. Harmonic compensation analysis in offshore wind power plants using hybrid filters. *Industry Applications, IEEE Transactions on*, 50(3):2050–2060, May 2014. ISSN 0093-9994. doi: 10.1109/TIA.2013.2286216.

[25] K.N. Md Hasan, A.M. Cantarellas, A. Luna, J.I. Candela, and P. Rodriguez. Grid harmonic detection and system resonances indentification in wave power plant applications. In *Industrial Electronics Society, IECON 2013 - 39th Annual Conference of the IEEE*, pages 1644–1649, Nov 2013. doi: 10.1109/IECON.2013.6699379.

[26] J. Beerten, S. D'Arco, and J.A. Suul. Cable model order reduction for hvdc systems interoperability analysis. In *AC and DC Power Transmission, 11th IET International Conference on*, pages 1–10, Feb 2015. doi: 10.1049/cp.2015.0039.

[27] *Electromagnetic Transient Program Reference Manual (EMTP Theory Book).*

[28] J. Wasilewski, W. Wiechowski, and C.L. Bak. Harmonic domain modeling of a distribution system using the digsilent powerfactory software. In *Future Power Systems, 2005 International Conference on*, pages 7 pp.–7, Nov 2005. doi: 10.1109/FPS.2005.204272.

[29] Wilsun Xu. Component modeling issues for power quality assessment. *Power Engineering Review, IEEE*, 21(11):12–17, Nov 2001. ISSN 0272-1724. doi: 10.1109/MPER.2001.961998.

[30] A.A. Rockhill, M. Liserre, R. Teodorescu, and P. Rodriguez. Grid-filter design for a multimegawatt medium-voltage voltage-source inverter. *Industrial Electronics, IEEE Transactions on*, 58(4):1205–1217, April 2011. ISSN 0278-0046. doi: 10.1109/TIE.2010.2087293.

[31] Fritz Santjer, Bernd Weise, Tina Pausch, and Johannes Brombach. Aspects for improvement of measurement and assessment procedures of harmonic emission of wind power plants. In *DEWEK 2015*, May 2015.

[32] Ł. H. Kocewiak, B. L. Øhlenschlæger Kramer, O. Holmstrøm, K. H. Jensen, and L. Shuai. Active filtering application in large offshore wind farms. In *Integration of Wind Power into Power Systems as well as Transmission Networks for Offshore Wind Farms, Energynautics GmbH, 11-13 November 2014, Berlin, Germany*, pages 1–6, November 2014.

[33] Łukasz Hubert Kocewiak. *Harmonics in large offshore wind farms, PhD Thesis*. Videnbasen for Aalborg UniversitetVBN, Aalborg UniversitetAalborg University, Det Teknisk-Naturvidenskabelige FakultetThe Faculty of Engineering and Science, 2012.

[34] D.G. Holmes, T.A. Lipo, B.P. McGrath, and W.Y. Kong. Optimized design of stationary frame three phase ac current regulators. *Power Electronics, IEEE Transactions on*, 24(11):2417–2426, Nov 2009. ISSN 0885-8993. doi: 10.1109/TPEL.2009.2029548.

[35] L. Harnefors, A.G. Yepes, A. Vidal, and J. Doval-Gandoy. Passivity-based controller design of grid-connected vscs for prevention of electrical resonance instability. *Industrial Electronics, IEEE Transactions on*, 62(2):702–710, Feb 2015. ISSN 0278-0046. doi: 10.1109/TIE.2014.2336632.

[36] F.D. Freijedo, S.K. Chaudhary, R. Teodorescu, J.M. Guerrero, C.L. Bak, Ł.H. Kocewiak, and C.F. Jensen. Harmonic resonances in wind power plants: Modeling, analysis and active mitigation methods. In *PowerTech, 2015 IEEE Eindhoven*, pages 1–6, June 2015. doi: 10.1109/PTC.2015.7232382.

[37] Caixia Yang, Kaipei Liu, and Dongxu Wang. Harmonic resonance circuit's modeling and simulation. In *Power and Energy Engineering Conference, 2009. APPEEC 2009. Asia-Pacific*, pages 1–5, March 2009. doi: 10.1109/APPEEC.2009.4918398.

[38] R. Burch, G. Chang, M. Grady, E. Gunther, M. Halpin, Y. Liu, M. Marz, T. Ortmeyer, V. Rajagopalan, S. Ranade, P. Ribeiro, T. Sim, and W. Xu. Test systems for harmonics modeling and simulation. *Power Delivery, IEEE Transactions on*, 14(2):579–587, Apr 1999. ISSN 0885-8977. doi: 10.1109/61.754106.

[39] I Zlatunić, S Vodopija, and R Goić. Mode switching in modal domain models of overhead lines and underground cables. In *International Conference on Power Systems Transients (IPST2015) in Cavtat, Croatia June 15-18*, 2015.

[40] ABB. *XLPE Submarine Cable Systems, Attachment to XLPE Land Cable Systems - User's Guide*, volume Rev 5. .

[41] ABB. *XLPE Land Cable Systems, User's Guide*, volume Rev 5. .

[42] Vytautas Kersiulis, Andrzej Holdyk, Joachim Holboell, and Ivan Arana. Sensitivity of nodal admittances in an offshore wind power plant to parametric variations in the collection grid. In *Proceedings of the 11th International Workshop on Large-Scale Integration of Wind Power into Power Systems*, 2012.

[43] A.E. Leon and J.A. Solsona. Performance improvement of full-converter wind turbines under distorted conditions. *Sustainable Energy, IEEE Transactions on*, 4(3): 652–660, July 2013. ISSN 1949-3029. doi: 10.1109/TSTE.2013.2239317.

[44] S.V. Araujo, A. Engler, B. Sahan, and F. Antunes. Lcl filter design for grid-connected npc inverters in offshore wind turbines. In *Power Electronics, 2007. ICPE '07. 7th Internatonal Conference on*, pages 1133–1138, Oct 2007. doi: 10.1109/ICPE.2007.4692556.

[45] A. Reznik, M.G. Simoes, A. Al-Durra, and S.M. Muyeen. Lcl filter design and performance analysis for grid-interconnected systems. *Industry Applications, IEEE Transactions on*, 50(2):1225–1232, March 2014. ISSN 0093-9994. doi: 10.1109/TIA.2013.2274612.